

AD-A166 795

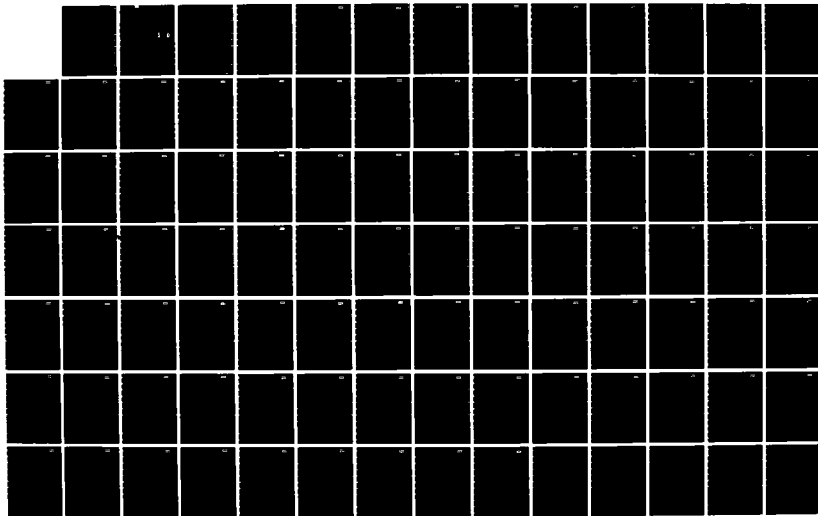
HGCDTE SURFACE AND DEFECT STUDY PROGRAM(U) SANTA
BARBARA RESEARCH CENTER GOLETA CALIF J A WILSON ET AL.
MAR 86 SBRC-60411 MDA903-83-C-0100

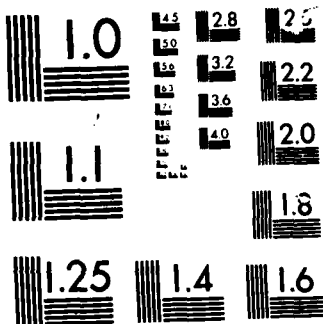
1/2

UNCLASSIFIED

F/G 20/12

NL





MICROCOPY

CHART

2

HgCdTe SURFACE AND DEFECT STUDY PROGRAM

J. A. Wilson and V. A. Cotton
Santa Barbara Research Center
Goleta, CA 93117

J. A. Silberman, G. P. Carey, A. K. Wahl
D. J. Friedman, C. K. Sikh, K. A. Bertness, I. Lindau, and W. E. Spicer
Stanford Electronics Laboratories
Stanford, CA 94305

A. Sher and A.-B. Chen
SRI International
Menlo Park, CA

R. G. Wilson
Hughes Research Laboratories
Malibu, CA

March 1986

FINAL TECHNICAL REPORT

Contract No. MDA-903-83-C-0108

The views, opinions, and findings contained in this report are those of the authors and should not be construed as an official Department of Defense position, policy, or decision, unless so designated by other official documentation.

Prepared for:
DARPA
1400 Wilson Blvd.
Arlington, Virginia 22209
Attention: Dr. James Murphy
Defense Science Office

DTIC
ELECTE
APR 22 1986
S D

DTIC FILE COPY

CLEARED
FOR OPEN PUBLICATION

APR 17 1986

3

DIRECTORATE FOR FREEDOM OF INFORMATION
AND SECURITY REVIEW (OASD-PA)
DEPARTMENT OF DEFENSE

86 4 22 184 86

1369

HgCdTe SURFACE AND DEFECT STUDY PROGRAM

**J. A. Wilson and V. A. Cotton
Santa Barbara Research Center
Goleta, CA 93117**

**J. A. Silberman, G. P. Carey, A. K. Wahi
D. J. Friedman, C. K. Sikh, K. A. Bertness, I. Lindau, and W. E. Spicer
Stanford Electronics Laboratories
Stanford, CA 94305**

**A. Sher and A-B. Chen
SRI International
Menlo Park, CA**

**R. G. Wilson
Hughes Research Laboratories
Malibu, CA**

March 1986

FINAL TECHNICAL REPORT

Contract No. MDA-903-83-C-0108

**The views, opinions, and findings contained in
this report are those of the authors and should
not be construed as an official Department of
Defense position, policy, or decision, unless so
designated by other official documentation.**

**Prepared for:
DARPA
1400 Wilson Blvd.
Arlington, Virginia 22209
Attention: Dr. James Murphy
Defense Science Office**

1369

86 3 7 1-18

UNCLASSIFIED

SECURITY CLASSIFICATION OF THIS PAGE

REPORT DOCUMENTATION PAGE

1a. REPORT SECURITY CLASSIFICATION UNCLASSIFIED			1b. RESTRICTIVE MARKINGS		
2a. SECURITY CLASSIFICATION AUTHORITY			3. DISTRIBUTION/AVAILABILITY OF REPORT		
2b. DECLASSIFICATION/DOWNGRADING SCHEDULE					
4. PERFORMING ORGANIZATION REPORT NUMBER(S) RPT60411			5. MONITORING ORGANIZATION REPORT NUMBER(S)		
6a. NAME OF PERFORMING ORGANIZATION SANTA BARBARA RESEARCH CENTER		6b. OFFICE SYMBOL (If applicable)	7a. NAME OF MONITORING ORGANIZATION DARPA/DSO		
6c. ADDRESS (City, State and ZIP Code) 75 Coromar Drive Goleta, CA 93117			7b. ADDRESS (City, State and ZIP Code) 1400 Wilson Blvd. Arlington, VA 22209		
8a. NAME OF FUNDING/SPONSORING ORGANIZATION DARPA/DSO		8b. OFFICE SYMBOL (If applicable)	9. PROCUREMENT INSTRUMENT IDENTIFICATION NUMBER		
8c. ADDRESS (City, State and ZIP Code) 1400 Wilson Blvd. Arlington, VA 22209			10. SOURCE OF FUNDING NOS.		
			PROGRAM ELEMENT NO.	PROJECT NO.	TASK NO.
11. TITLE (Include Security Classification) HgCdTe Surface and Defect Study Program (U)					
12. PERSONAL AUTHOR(S) Wilson, J.A.; Cotton, V.A.					
13a. TYPE OF REPORT FINAL TECHNICAL		13b. TIME COVERED FROM 7/1/85 TO 3/2/86		14. DATE OF REPORT (Yr., Mo., Day) MARCH 1986	
15. PAGE COUNT ?					
16. SUPPLEMENTARY NOTATION Authors of papers included in this report: Silberman, J.A.; Carey, G.P.; Wahi, A.K.; Friedman, D.J.; Shih, C.K.; Bertness, K.A.; Lindau, I.; Spicer, W.E.; Sher, A.; Chen, A.-B.; and Wilson, R.G.					
17. COSATI CODES			18. SUBJECT TERMS (Continue on reverse if necessary and identify by block number)		
FIELD	GROUP	SUB. GR.	HgCdTe, CdZnTe, HgZnTe, tetrahedral crystal structure surfaces, defects, electronic structure, interface, damage doping, channeled implants, surface damage.		
19. ABSTRACT (Continue on reverse if necessary and identify by block number) Enhanced doping density within 250Å of the passivated interface of $\text{Hg}_{0.7}\text{Cd}_{0.3}\text{Te}$ (PHOTOX-SiO ₂ and anodic oxide) were measured using capacitance voltage techniques. Detailed doping profiles in channeled implants in $\text{Hg}_{0.7}\text{Cd}_{0.3}\text{Te}$ show that nuclear damage is the dominant mechanism causing damage induced donor levels with profiles similar to those expected for unoriented implants. Implant atomic profiles are presented for a variety of ions. The role of the weak Hg bond is discussed in forming interfaces with Ag, Cu and Al. CdTe band structure is calculated using a nonlocal pseudo-potential and the results are used to interpret angle-resolved photoemission spectroscopy results on HgCdTe. Dislocation energies and hardnesses are calculated by an extension of Harrison's model as are bond length and bond energy changes. Bond-length relaxation in pseudo-binary alloys is applied to the case of tetrahedral structures and compared to $\text{Ga}_{1-x}\text{In}_x\text{As}$. Anomalous behavior of Si 2p core-exciton binding energy and line width is explained in $\text{Si}_x\text{Ge}_{1-x}$ alloys. Finally, correlations between Cd and Zn in $\text{Cd}_{1-x}\text{Zn}_x\text{Te}$ and Hg and Zn in $\text{Hg}_{1-x}\text{Zn}_x\text{Te}$ are calculated.					
20. DISTRIBUTION/AVAILABILITY OF ABSTRACT UNCLASSIFIED/UNLIMITED <input checked="" type="checkbox"/> SAME AS RPT. <input type="checkbox"/> DTIC USERS <input type="checkbox"/>			21. ABSTRACT SECURITY CLASSIFICATION UNCLASSIFIED		
22a. NAME OF RESPONSIBLE INDIVIDUAL			22b. TELEPHONE NUMBER (Include Area Code)		22c. OFFICE SYMBOL

SUMMARY

This report presents results obtained in the final six month period, July 1985 to March 2, 1986 and summarizes the principal accomplishments of the entire period of performance starting in November 1982.

Changes in doping density near the passivated interface of $\text{Hg}_{0.7}\text{Cd}_{0.3}\text{Te}$ have been measured using a newly developed algorithm (reference 3 of Section 1) which allows accurate determination right up to the interface itself. Doping density is significantly higher within 250 to 500Å of the interface than in the bulk, at distances beyond 1000Å from the interface. This increase is interpreted as inhomogeneously distributed surface damage to the Te lattice. As such, this is another manifestation of the same effects seen as: Cd loss from the processed surface, by photoelectron spectroscopy; and low X value regions at the PHOTOX[™]-SiO₂ interface measured by low temperature electroreflectance, and reported in the fifth interim technical report.

A significantly more detailed measurement than any previously reported of the doping profiles resulting from attempted channeled implants of various ions into the (110) surface of $\text{Hg}_{0.7}\text{Cd}_{0.3}\text{Te}$ are presented. The implanted wafer was etched at a low angle, with many MIS devices then made on the new surface. Measurements of average doping density across the depletion region of these devices produced a high resolution depth profile. Despite the use of surface processing designed to minimize mechanical damage to the surface (and hence maximize channeling), the profiles are still dominated by damage mechanisms and show an essentially gaussian doping profile as expected for random implantation. Actual channeling is achieved only for a small fraction of the incident ions in each sample.

We discuss the role of the weak bonding of Hg in the $\text{Hg}_{1-x}\text{Cd}_x\text{Te}$ lattice on interface morphology when metal is deposited on the surface. The Ag/HgCdTe, Cu/HgCdTe, Al/HgCdTe and Cu/CdTe interfaces are studied in ultra-high vacuum with X-ray and ultraviolet photoemission and with low energy electron diffraction. The three metals are found to yield distinctly different interface morphologies. For Ag/HgCdTe, the Hg instability results in vacancy diffusion of Ag $10^2 - 10^3\text{Å}$ into the semiconductor. For Cu overlayers, the instability greatly enhances Te and Cd intermixing into the Cu for HgCdTe compared to CdTe. The more reactive Al overlayers deplete the weakly bound Hg

from the HgCdTe surface. We compare the metal/HgCdTe interfaces with the corresponding metal/CdTe and metal/GaAs interfaces. For the three overlayer metals on HgCdTe the instability of the Hg bond results in interfaces with a much greater degree of intermixing than for the corresponding metal/binary semiconductor interfaces.

As an aid in completing the analysis of the angle-resolved data, calculation of the band structure of CdTe using the nonlocal pseudopotential of Chelikowsky and Cohen (reference 1 of Section 3.2) was performed. The spectrum of computed energies and wave functions spanned the valence bands and the high lying conduction bands up to 30 eV above the valence band maximum. The results of this calculation shed insight into the role of the actual final states involved in the normal emission from CdTe (and by analogy, from $\text{Hg}_{1-x}\text{Cd}_x\text{Te}$) in shaping the features observed in the spectra. While a simple model of approximating the final states by free electron parabolas, successfully accounts for much of the observed structure, certain peaks in the data reflect instead the mixing of the parabolic bands that takes place in the crystal potential.

Angle-resolved photoemission spectroscopy (ARPES) study of the band structure of $\text{Hg}_{1-x}\text{Cd}_x\text{Te}$ along the {110} direction using normal emission method has been published by Silberman et al (reference 1 of Section 3.3). This work is an extension of the band mapping along other major symmetry directions ({111} and {100}) using off-normal emission method. By assuming a direct transition model (DTM) and the free electron final state, the band mapping along {100} direction shows very good agreement with the band calculations by Chelikowsky et al, for CdTe using nonlocal pseudopotential method, and Hass et al, (References 2 and 3 of Section 3.3) for HgTe and $\text{Hg}_{1-x}\text{Cd}_x\text{Te}$ using empirical tight binding method.

The dislocation energies and hardness of semiconductors are calculated by an extension of Harrison's method. It is demonstrated in agreement with experiment that dislocation energies per unit length are proportional to $d^{-3} - d^{-9}$, where d is the bond length and hardness is proportional to $d^{-5} - d^{-11}$. The hardness is related to the interaction energies among dislocations. It is argued that dislocation densities of semiconductors will be reduced if they are alloyed with a second constituent that has a shorter bond length. Experimental evidence supporting this strategy is noted.

The bond length and energy changes of the constituents of alloys relative to their pure crystal values are calculated from an extension of Harrison's method. It is demonstrated that the already weak HgTe bonds are destabilized by adjacent CdTe, HgS, or HgSe, but are stabilized by ZnTe. It is also argued that dislocation energies and the hardness of semiconductors vary as a high inverse power of the bond length of the constituents. Hence, the shorter ZnTe bond as an additive should improve the structural properties of HgTe and CdTe. Experiments that support these predictions are noted. The electronic transport properties of 0.1 eV band gap HgZnTe are about the same as those of HgCdTe, and the structural properties of the Zn compound are superior; thus, we conclude that HgZnTe is likely to be the better material for IR devices.

The bond-length relaxation in pseudobinary alloys can be predicted by a simple radial force model. In tetrahedral structure alloys the bond-length deviation of the solute in the dilute solution is a quarter of the bond-length difference between the two components. This result agrees with the experimental work done on the $\text{Ga}_{1-x}\text{In}_x\text{As}$ system performed by Mikkelsen and Boyce (Reference 1, Section 4.3).

A calculation is presented to explain the anomalous experimental behavior of the Si 2p core-exciton binding energy and linewidth in $\text{Si}_x\text{Ge}_{1-x}$ alloys. The observed minimum in the linewidth near $x \approx 0.15$ can be explained as the result of a competition between intrinsic broadening due to screening and extrinsic alloy broadening. For pure Si, the binding energy is estimated to be 0.15 ± 0.05 eV and the width is shown to be smaller than that observed at $x \approx 0.15$.

Correlations between atoms of Cd and Zn in $\text{Cd}_{1-x}\text{Zn}_x\text{Te}$ and Hg and Zn in $\text{Hg}_{1-x}\text{Zn}_x\text{Te}$ are calculated within an extended quasichemical approximation. A tetrahedron of alloy atoms is used for the microcluster unit. The statistical mechanics of the correlations is outlined for the present problem and an approximate method of solution is indicated. Microcluster energies are obtained from an approximation of a Keating model due to Martin, plus a correction due to Harrison to account for the coupling between the tetrahedral bonds. It is found that the correlations are significant at typical growth temperatures (300 to 600K). $\text{Hg}_{1-x}\text{Zn}_x\text{Te}$ is predicted to undergo spinoidal decomposition between 300K and 600K.

1
2
3
4
5
6
7
8
9
10
11
12
13
14
15
16
17
18
19
20
21
22
23
24
25
26
27
28
29
30
31
32
33
34
35
36
37
38
39
40
41
42
43
44
45
46
47
48
49
50
51
52
53
54
55
56
57
58
59
60
61
62
63
64
65
66
67
68
69
70
71
72
73
74
75
76
77
78
79
80
81
82
83
84
85
86
87
88
89
90
91
92
93
94
95
96
97
98
99
100



Availability Codes	
Dist	Avail and/or Special
A-1	

PRINCIPAL ACCOMPLISHMENTS OF THE HgCdTe SURFACE AND DEFECT STUDY PROGRAM

The purpose of the study was to examine the fundamental physics and chemistry of interface formation on HgCdTe to the eventual goal of improving interface technology, particularly surface passivation.

- Passivated interfaces of HgCdTe are dominated by surface processing induced damage to the HgCdTe lattice. The damage extends over an effective depth of between 200 and 500Å from the interface. This includes both grown (e.g., anodic oxide) and deposited (e.g., PHOTOX™-SiO₂) passivation technologies.
 - Storage time and hence minority carrier lifetime are shortened (measured by capacitance transient analysis)
 - Local doping at the interface is increased by at least an order of magnitude (measured by capacitance-voltage (C-V) depth profiling using a new data reduction algorithm)
 - Band structure, including energy bandgap is altered (measured by admittance spectroscopy, electoreflectance and C-V)
 - Lattice alteration is associated with loss of Cd during processing; interface composition is distorted from stoichiometry (measured by photoelectron spectroscopy and electoreflectance)
- These technology effects are a direct result of the underlying susceptibility of the HgCdTe to be easily damaged due to the weak HgTe bond which is further destabilized by the presence of Cd.
- The underlying causes of the bandgap variation of Hg_{1-x}Cd_xTe alloys and their fragile structural properties have been identified with the unique nature of the Hg 6s-valence state energy.
- Understanding of this effect has allowed us
 - To explain the breakdown of the virtual crystal approximation observed in the valence band by PES.
 - To identify the reason for Hg and Cd core d-state energy shifts as being caused by charge transfer from CdTe to HgTe bonds.
 - To predict that the already weak HgTe bond would be destabilized by an adjacent CdTe bond, while ZnTe would cause a less deleterious effect.
- Our study of the strain coefficients led us to appreciate Harrison's prediction that strain coefficients vary roughly as d^{-9} , where d is the bond length, means that substitution of a

short bond length constituent, e.g. ZnTe in a longer bond length host will strengthen the host.

- Based on these concepts, we have suggested that $\text{Hg}_{1-x}\text{Zn}_x\text{Te}$ was a good candidate material to replace $\text{Hg}_{1-x}\text{Cd}_x\text{Te}$ for long wave length infrared detectors. Preliminary experimental results strongly support these contentions.
- Also based on this theory suggested that JnAs substituted into GaAs is a preferred way to minimize dislocations in GaAs. An explanation of the mechanism through which the longer bonded InAs functions to decrease dislocations densities was also proposed.
- Derived an entirely new hardness of semiconductors that agrees with experimental results for many systems.
- Properly predicted the observations by Mikkelsen and Boyce of the bond length variations of GaAs and InAs in the $\text{Ga}_{1-x}\text{In}_x\text{As}$ alloy, and predicted equivalent results for all group IV, and II-V and II-VI compound alloys.
- With no adjustable parameters in the theory, mixing enthalpies, which are in general agreement with experiment, are calculated for all semiconductor alloys.
- Devised a new correlated statistical theory of order-disorder transitions which demonstrates that as a rule, all alloys are partially ordered (not random), and the degree of ordering depends on growth conditions.
- Appreciated the reasons that calculated deep defects states are sensitive to the quality of the host band structure. In particular, it was demonstrated that no tight binding few-neighbor calculation currently used is capable of producing accurate results, and most will not even yield proper trends.

While we have made considerable progress toward understanding, the bulk and interface properties of HgCdTe our most recent work has raised several questions that remain unanswered. A collection of the more important ones are:

- What is the influence of strains that are present during growth, either because of effects at the melt-solid interface in solid state recrystalline growth or because of lattice mismatches between the substrate and the alloy in epitaxial growth, on the cluster populations?
- Do dipolar energies due to Madelung terms and electron-electron interactions play a significant roll in cluster populations? (Our preliminary answer is yes.)

- What is the relation between cluster populations and vacancy formation energies and diffusion?
- What influence do the clusters have on electrical transport properties?
- What drives interface and metal-contact structural behavior?
- What effects can one expect in superlattices as a consequence of these cluster ideas?
- Make the relation between alloy composition, growth method, strain coefficients, dislocation energies, and hardness explicit.

There are many other questions that could be added to this list, but these are a set of pressing ones that should be pursued.

Finally, even though our investigation of the feasibility of avoiding the damage due to ion implantation by channeling into the {110} face was not entirely successful, there are several important technological conclusions that can be reached:

- Channeling in HgCdTe does occur, though it does not dominate. The lattice damage, mentioned above, which affects passivated interfaces also clogs the channels at the surface so that most of the incident ions are scattered into a random implant range profile.
- Damage induced donor level follows the 'random' portion of the implant profile but increased in concentration by a factor of 10 (except in H and Cl).
- Hydrogen shows a damage level below the peak atomic concentration inferring that the H takes most of the recoil resulting in little lattice distortion.
- Chlorine is the only ion evaluated so far which shows a damage to ion concentration ratio of 100. Chlorine also shows a shoulder in the damage profile which roughly follows the channeled portion of the ion profile.

CONTENTS

<u>Section</u>	<u>Page</u>
Summary and Principal Accomplishments of the HgCdTe Surface and Defect Study Program.....	111
Introduction.....	1
1 INTERFACE STUDY TASK.....	5
Introduction.....	6
Sample Preparation and Measurement.....	7
Results.....	8
Conclusion.....	17
Acknowledgments.....	18
References.....	18
2 CHanneled IMPLANT TASK.....	21
2.1 Channeled Ion Implantation Range Studies in HgCdTe.....	22
Introduction.....	22
Experimental Techniques and Accuracies.....	23
Experiments.....	24
SIMS Measurement Technology.....	33
Discussion.....	35
Conclusions.....	35
References.....	35
2.2 Doping Profiles of Channeled Ion Implantation in HgCdTe....	37
Implant Profiles.....	37
Introduction.....	37
Sample Prop. and Experiment.....	37
Results.....	37
Conclusion.....	42
3 SURFACE STUDY AND OXIDATION CHEMISTRY.....	43
Introduction.....	44
Summary.....	45
References.....	47
3.1 ROLE OF Hg BONDING IN METAL/Hg _{1-x} Cd _x Te INTERFACE FORMATION	56
References.....	68

CONTENTS (Cont)

<u>Section</u>		<u>Page</u>
3.2	CALCULATION OF CdTe BAND STRUCTURE.....	70
	References.....	71
3.3	ANGLE-RESOLVED PHOTOEMISSION STUDY OF THE CdTe, HgTe, AND $Hg_{1-x}Cd_xTe$ BAND DISPERSIONS ALONG MAJOR SYMMETRY DIRECTIONS, AND THE ALLOYING EFFECT IN $Hg_{1-x}Cd_xTe$	72
	References.....	74
4	ALLOY BONDING.....	77
4.1	Dislocation Energies and Hardness of Semiconductors.....	78
4.2	Effects Influencing the Structural Integrity of Semiconductors and Their Alloys.....	81
4.3	Bond Length Relaxation in Pseudobinary Alloys.....	88
4.4	Binding Energy and Spectral Width of Si $2p$ Core Electrons in Si_xGe_{1-x} Alloys.....	90
4.5	Correlations in Pseudobinary Alloys.....	94
5	LIST OF PAPERS, PRESENTATIONS AND THESES SUPPORTED IN PART OR IN WHOLE BY THIS CONTRACT.....	116

ILLUSTRATIONS

<u>Figure</u>		<u>Page</u>
1-1	Measured Doping Density versus Depth for Distances Up to 1000Å From the Insulator/Hg _{0.7} Cd _{0.3} Te Interface.....	10
1-2	Equivalent Circuit of Measured MIS Capacitor Showing Contributions Due to Insulator (C _{ins}), Depletion Layer (C _d), Interface Traps (i _T , R _{iT}) and Inversion Layer (C _{inv} , R _{inv}).....	12
1-3	1/C _d ² versus Surface Potential Excursion for MIS Devices Made With PHOTOX™-SiO ₂ on n-Type Hg _{0.7} Cd _{0.3} Te.....	13
1-4	1/C _d ² versus Surface Potential Excursion for MIS Devices Made with PHOTOX™-SiO ₂ on p-Type Hg _{0.7} Cd _{0.3} Te.....	14
1-5	1/C _d ² versus Surface Potential Excursion for MIS Devices Made with Anodic Oxide Grown on n-Type Hg _{0.7} Cd _{0.3} Te.....	15
1-6	1 MHz Capacitance Voltage Curves for the Samples Used in This Study.....	17
2-1	Partial Periodic Table of the Elements, Showing the First Four Rows (Through Kr) Plus In and Sb and the Three Substrate Components, Hg, Cd, and Te. The potential dopants in columns 1, 3, 5 and 7, which were also the ions implanted and profiled in this work, are outlined in boxes.....	25
2-2	Channeled Depth Distributions for Selected Ions Implanted in the {110} direction of HgCdTe at 150 keV.....	25
2-3	Random Depth Distributions for Selected Ions Implanted in {110} HgCdTe at 150 keV.....	26
2-4	{111} Random and {110} Channeled Depth Distributions for ² H Ions Implanted in HgCdTe at 200 keV.....	26
2-5	Channeled Depth Distributions for Selected Ions Implanted in the {110} Direction of HgCdTe at 200 keV (to 5 μm).....	27
2-6	{111} Random and {110} Channeled Depth Distributions for Li Implanted in HgCdTe at 200 keV.....	27
2-7	{111} Random and {110} Channeled Depth Distributions for F Implanted in HgCdTe at 200 keV.....	28
2-8	{111} Random and {110} Channeled Depth Distributions for Na Implanted in HgCdTe at 200 keV.....	28
2-9	{111} Random and {110} Channeled Depth Distributions for Al Implanted in HgCdTe at 200 keV.....	29
2-10	{111} Random and {110} Channeled Depth Distributions for Cl Implanted in HgCdTe at 200 keV.....	29
2-11	{111} Random and {110} Channeled Depth Distributions for K Implanted in HgCdTe at 200 keV.....	30
2-12	{111} Random and {110} Channeled Depth Distributions for Br Implanted in HgCdTe at 200 keV.....	30

ILLUSTRATIONS (Cont)

<u>Figure</u>		<u>Page</u>
2-13	{111} Random and {110} Channeled Depth Distributions for In Implanted in HgCdTe at 200 keV.....	31
2-14	Channeled Depth Distributions for 200 keV B Implanted into Different HgCdTe Substrates.....	33
2-15	38
2-16	38
2-17	39
2-18	39
2-19	40
2-20	40
2-21	41
3-1	Valence Band Spectra at $h\nu = 21.2$ eV of the Clean $Hg_{1-x}Cd_xTe$ Surface as Well as for the Surface Covered by 5 ml of Each Overlayer Metal. The Cu/ $Hg_{1-x}Cd_xTe$ spectrum is for the composition $x = 0.25$; the other three spectra are for $x = 0.23$. A spectrum of clean $x = 0.25$ $Hg_{1-x}Cd_xTe$ is not shown as it is very similar to the clean $x = 0.23$ spectrum.....	60
3-2a	Attenuation of the XPS Peak Areas I of the $Hg_{1-x}Cd_xTe$ Core Levels With Increasing Cu Coverage. The peak areas are normalized to their zero-coverage values I_0	62
3-2b	Attenuation of the Semiconductor Core Level Peak Areas as in (a), but for Cu/CdTe.....	62
3-3	Attenuation of the XPS Peak Areas I of the $Hg_{1-x}Cd_xTe$ Core Levels With Increasing Al Coverage. The peak areas are normalized to their zero-coverage values I_0	64
3-4	Calculated CdTe Conduction Bands of Σ_3 Symmetry and Identification of States With Greater Than 30% () or Between % and 30% (Δ) [220] Plane Wave Character. Also shown are portions of the experimental final states for peaks No. 1, No. 3, and No. 7 (0).....	71
3-5	The Band Mappings of CdTe (●) and HgTe (o) Along [100] Direction using Off-normal Emission ARPES. The theoretical calculations for CdTe from Ref. 2 (solid line) and HgTe from Ref. 3 (dash line) are also shown for comparison. Only the lower bands are presented.....	75
3-6a	Comparison of the Theoretical Calculation of Σ_s' (E) for $Hg_{0.7}Cd_{0.3}Te$ and the Experimental Result of the ARPES Peak Shift From the VCA Value of <100> Lower Band.....	75
3-6b	Comparison of $2\Sigma_s''$ (E) for $Hg_{0.7}Cd_{0.3}Te$ and the Experimental Result of ARPES Peak Broadening. The broadening data was obtained by comparing ARPES data of HgTe and $Hg_{0.7}Cd_{0.3}Te$ of the same photon energy $h\nu$, and the analyzer angle θ_A	75

ILLUSTRATIONS (Cont)

<u>Figure</u>		<u>Page</u>
3-7	Density of States Projected on Cation s Orbitals for HgTe (solid curve) and CdTe (dashed curve) [cf. Eq. (17)].....	76

TABLES

<u>Table</u>		<u>Page</u>
1-1	9
3-1	Heats of Te Formation ΔH_f , and Heats of Solution $\Delta H_{sol}(C;M)$ of Cation C in Metal M in the Solid Phase, for Various Metals on $Hg_{1-x}Cd_xTe$	57

INTRODUCTION

The bandgap tunability of HgCdTe between the absorption energies of 0.0 eV (HgTe) to 1.5 eV (CdTe) makes the HgCdTe alloy system the premier candidate for use in infrared detection. The potential electronic properties of this semiconductor system had been realized with very limited success in the time period leading up to the inception of this program. Large single element photo-detector devices had been manufactured with some success, but as more and more sophisticated device demands were made on this system, for example, the manufacture of large scale photovoltaic focal plane arrays, inherent problems in the passivation of HgCdTe emerged which greatly reduced the success of these devices. The extreme desirability of obtaining working infrared imaging systems caused many research and development efforts to search for quick solutions to the problems plaguing HgCdTe technology. It was often felt that merely extending Si and III-V semiconductor process technology to the processing of II-VI semiconductor systems with a few alterations would produce successful yields for these II-VI devices. These empirical approaches have shown limited success at reducing some of the key problems hindering successful device fabrication. It was felt that an investigation aimed at examining the nature of the bonding in the alloy and the electrical and mechanical properties of this alloy system and their ultimate effect on the device physics was a necessary first step in solving the fundamental problems plaguing HgCdTe technology.

Our most important results have been:

- establishing the breakdown of the Virtual Crystal Approximation (VCA),
- recognizing the close relationship of this with the relative instability of Hg in the lattice as well as tunability of the bandgap, and
- establishing that $\text{Hg}_{1-x}\text{Zn}_x\text{Te}$ would have important advantages over HgCdTe because of the increased Hg stability in the lattice (based strongly on the theoretical work of Arden Sher in the SRI portion of this contract).

Further work on oxidation and metallization showed that the weak bonding on Hg is a key consideration in HgCdTe interfaces and makes the interfaces of this material very different from those of other zincblend materials such as Si, GaAs, or even CdTe.

In the time period leading up to this joint contract between SBRC, Stanford and SRI, there were some key observations and questions concerning HgCdTe that were not well-understood. One of the most critical parameters involving the optimization of device fabrication, operation, and reliability is the interface found between the HgCdTe and any passivating or metal overlayer. For HgCdTe the sticking coefficient of oxygen had been observed to be very small by Benninghoven,¹ and Ebina² found the sticking coefficient of oxygen on a clean cleaved CdTe {110} surface to be less than 10^{-14} . The native oxide of HgCdTe and the simpler CdTe were not well-understood, and the critical chemistry between the HgCdTe and the native oxide layer was unknown. Another unusual observation by Benninghoven was the Hg out-diffusion from the bulk even at room temperature. The difficulty of maintaining structural integrity and stoichiometry during the rigors of device processing were unknown. These observations provided a possible link to the behavior observed in practical devices. Surface leakage being a persistent problem in device structures could be explained by a build-up of out-diffused Hg in the interface region between the passivant and the HgCdTe. The difficulty in binding oxygen to stoichiometric HgCdTe could affect any passivation process on the HgCdTe surface. Another important observation by Benninghoven was that HgCdTe was particularly sensitive to electron beam-induced desorption. Therefore the ability to characterize HgCdTe using electron spectroscopies without introducing artifacts or anomalous stoichiometry values was unknown. Given the high thermodynamic activity of Hg in the alloy, resulting in a very high equilibrium vapor pressure, it was not even known if HgCdTe would be stable in the ultra-high vacuum (UHV) environment employed during photoemission spectroscopy experiments (PES). There were certainly many more unusual observations of the HgCdTe alloy system in addition to those mentioned above, but these exemplify the unusual behavior of an alloy that appeared to have an electronic structure that was strongly influenced by the mechanical defect structure, possibly related to the peculiar nature of the bonding of HgCdTe as compared to GaAs and other III-V semiconductors.

Because of our success in employing PES to gain great insights into the physics and chemistry of surfaces and interfaces of Si and III-V semiconductors, we felt that we could draw upon our scientific experience with these systems and provide for a more fundamental framework of understanding into the HgCdTe alloy system. Since many of the critical device parameters are diffi-

cult to control in this material, the complexity of these parameters demanded a more scientific approach to be employed in solving and understanding in a more fundamental way the characteristics of this material that directly lead to reduced reliability and lower yields. The success of this approach is manifested by the many contributions to the present HgCdTe technology from SBRC, Stanford, and SRI while funded by this contract. It would be impossible to do proper justice to all of the work that we have conducted under this contract in this report, therefore the following paragraphs are intended only as a summary of the key work. The complete list of publications made over the duration of this contract that is presented in Section 4 gives testimony to the successes and achievements of our HgCdTe research.

Discussions of specific accomplishments over the entire program period and results obtained in the period July 1985 to March 1986 are included in the following four sections. Each section deals primarily with one of the performing organizations.

HUGHES

SANTA BARBARA RESEARCH CENTER
a subsidiary

(THIS PAGE INTENTIONALLY LEFT BLANK)

HUGHES

SANTA BARBARA RESEARCH CENTER
a subsidiary

Section 1
INTERFACE STUDY TASK

DAMAGE ENHANCED DOPING AT THE HgCdTe SURFACE

J.A. Wilson and V.A. Cotton

INTRODUCTION

The passivation of HgCdTe surfaces involves the use of certain chemical treatments which have recently been shown to cause distortions in the surface composition from that of a stoichiometric alloy.¹ This is a form of surface damage which is expected to have a direct effect on the electronic structure of any interface which is later formed. Some compositional changes have also been recently identified at the PHOTONTM-SiO₂ interface, by electroreflectance (ER), which may be due to the actual deposition of the passivation layer itself.² Both of these effects are very local to the surface, a few tens to hundreds of angstroms. Measurement of the doping profile through the depletion region of an MIS device formed on HgCdTe is probably one of the most sensitive probes of the electrical consequences of these forms of near surface damage. Composition distortions of up to a few atomic percent are seen within 20 to 30Å of the surface with Photoelectron Spectroscopy (PES) while changes in doping concentration on the order of 10^{14} cm⁻³ can be detected. This is nine orders of magnitude lower than the conventional levels detected by PES and ER and will allow detection of the deeper tail of this surface damage.

We have measured the doping profile through the depletion region of MIS devices made on $x = 0.3$ Hg_{1-x}Cd_xTe using PHOTONTM-SiO₂ or anodic oxide as the insulator. These profiles are calculated from high frequency and quasistatic capacitance voltage curves using an algorithm which avoids the divergence of the computed profile within an extrinsic Debye length of the interface, common to previous measurements. A sharply higher doping concentration is seen at the interface in all the HgCdTe samples measured. The concentration drops to the bulk value generally on a scale of 200 to 500Å, though some increased doping can sometimes be seen at 1000Å. Comparison of the behavior of n and p-type samples indicate the resulting surface structure is more complex than expected for the case of one type of uniformly introduced defect. The results suggest a heterogeneous distribution of composition and defects across the surface under the gate with neighboring regions contributing n or p-type behavior.

SAMPLE PREPARATION AND MEASUREMENT

The MIS structures were made on n and p-type HgCdTe with a bulk composition (mole fraction, x) of about 0.30. Ingots were grown by the horizontal zone melt technique, cut into wafers, polished to remove saw damage and then isothermally annealed in Hg vapor to reduce the cation vacancies left from the high temperature (600°C) growth. The anneal lowers the native defect acceptor concentration below that of the residual donor impurities to produce n-type, or not quite to that concentration to produce p-type. n or p-type is selected by setting the anneal temperature. Only the wafers outermost 100 to 125 μm are affected in this way during the four week anneal.

The wafers were chemomechanically polished in a solution of Br_2 in DMF (dimethylformamide) and then dip etched in Br_2 in ethylene glycol to prepare the surface for passivation. Passivation was performed by deposition of between 1500 and 4000Å of PHOTOX[™]- SiO_2 or growth of 600Å of anodic oxide. The anodic oxide was grown using a voltage source stepped in two volt increments to a final voltage of 15V during the growth. In this process the current density is not held constant. Gates consisting of 400Å of Ti followed by 4000Å of Au were applied by thermal evaporation through a shadow mask. No photoresist techniques were employed. In addition a C-V standard made with SiO_2 grown on Si was used as a control to verify the data reduction technique.

Capacitance measurements were made at 1 MHz using a PAR 410 capacitance meter and at quasistatic using an electrometer³ (ramp rate is between 10 and 50 mV/sec). Typical current levels are 10^{-11}A . Measurements were made in a dewar cooled with LN_2 and with zero field of view.

The C-V data was reduced to give surface potential versus applied gate bias, $1/C_d^2$ versus surface potential (ϕ_s) and doping versus depth, using an algorithm based on the analysis presented in reference 3.

Integration of the quasistatic capacitance curve gives the dependence of surface potential (ϕ_s) versus applied bias, to within an additive constant.⁵ The doping density, N, as a function of depth, W, is given by

$$N(W) = \mp \frac{2}{\epsilon_s q} \left[\frac{1}{d\phi_s} \left(\frac{1}{C_d^2} \right) \right]^{-1} \frac{1}{1-g} \left(1 - \frac{2W^2}{\lambda^2} \frac{g}{(1-g)^2} \right)$$

where g is defined by

$$\frac{W}{\lambda} = (g - \ln g - 1)^{1/2}.$$

The value of g used in determining the doping is obtained from the slope of $1/C_d^2$ versus ϕ_s by a search routine fitting the expression

$$\frac{kT}{q} C_d^2 \frac{d}{d\phi_s} \left(\frac{1}{C_d^2} \right) = -2 \frac{g}{1-g} + \frac{1-g}{\frac{W^2}{\lambda^2}}$$

where the extrinsic Debye length is given by

$$\lambda = \left\{ \frac{2kT\epsilon_s}{q^2 |N(W)|} \right\}^{1/2}.$$

The value of $1/C_d^2$ is determined from the high frequency capacitance voltage data by the expression

$$1/C_d^2 = \left(\frac{C_{ins}}{C_{HF}} - 1 \right)^2$$

where C_{ins} is the insulator capacitance, C_{HF} is the measured high frequency capacitance, k is Boltzmann's constant, q is the electron charge, ϵ_s is the dielectric constant for HgCdTe and T is the temperature. The negative sign is for n-type and the positive sign for p-type HgCdTe. The additive constant in ϕ_s resulting from the Berglund integration can be determined from the intercept of the tangent to the portion of the $1/C_d^2$ versus ϕ_s curve, for ϕ_s in depletion, with the horizontal axis ($1/C_d^2 = 0$)⁶. It will become apparent from the data, that in many cases, the region of the $1/C_d^2$ curve through depletion is not closely approximated by a single slope. This indicates that there is a no single appropriate offset constant and therefore no single flatband condition for the bands near interfaces.

RESULTS

Doping profiles for samples made on both n and p-type HgCdTe using PHO-TOX™-SiO₂ as the insulator, and on n-type using anodic oxide show measured doping levels using this technique, which agree with those expected for the bulk material at depths far from the interface; 0.1 μm or deeper and agree with Hall data with a factor of 2. Near the interface, however, the measured

doping is seen to depart significantly from the bulk values for all the HgCdTe samples as shown in Table 1-1. Table 1-1 compares peak surface region doping to that in the bulk, at depths between half and one μm . The measured bulk doping is uniform at these depths. The increased apparent surface dopings are at least an order of magnitude. Figure 1-1 shows the portion of the doping profiles within 1000Å of the interface. Also shown is a doping profile of a Si MIS device, derived using the same algorithm, which shows no significant change in its bulk doping near the interface. The interface value of the doping, for the Si device, is within the range of fluctuation seen over the entire depletion region, about $2 \times 10^{14} \text{ cm}^{-3}$. This high degree of fluctuation is due to the hand digitizing required of this particular data set. The HgCdTe data was recorded directly by computer and consequently shows much less fluctuation over the entire depletion region for each sample.

Table 1-1.

Sample	MIS	Type	Doping		Surface Potential Range eV
			Surface cm^{-3}	Bulk cm^{-3}	
7161	PHOTOX™	n	2×10^{16}	2.2×10^{14}	0.25
2026	PHOTOX™	n	1×10^{15}	5×10^{13}	0.21
2069	PHOTOX™	n	3×10^{16}	6×10^{13}	0.16
3001	PHOTOX™	p	4×10^{16}	2.5×10^{15}	0.33
3002	PHOTOX™	p	1×10^{17}	1.8×10^{15}	0.40
0054	Anodic	n	1×10^{19}	2×10^{14}	0.51
0058	Anodic	n	1×10^{19}	2×10^{14}	0.54
Si	SiO ₂	n	2×10^{14}	2×10^{14}	0.91

Figure 1-1 shows doping profiles for: three n-type devices, numbers 7161, 2026 and 2069; two p-type devices, 3001 and 3002, all made using PHOTOX™-SiO₂; and two n-type devices made with Anodic oxide, 0054 and 0058.

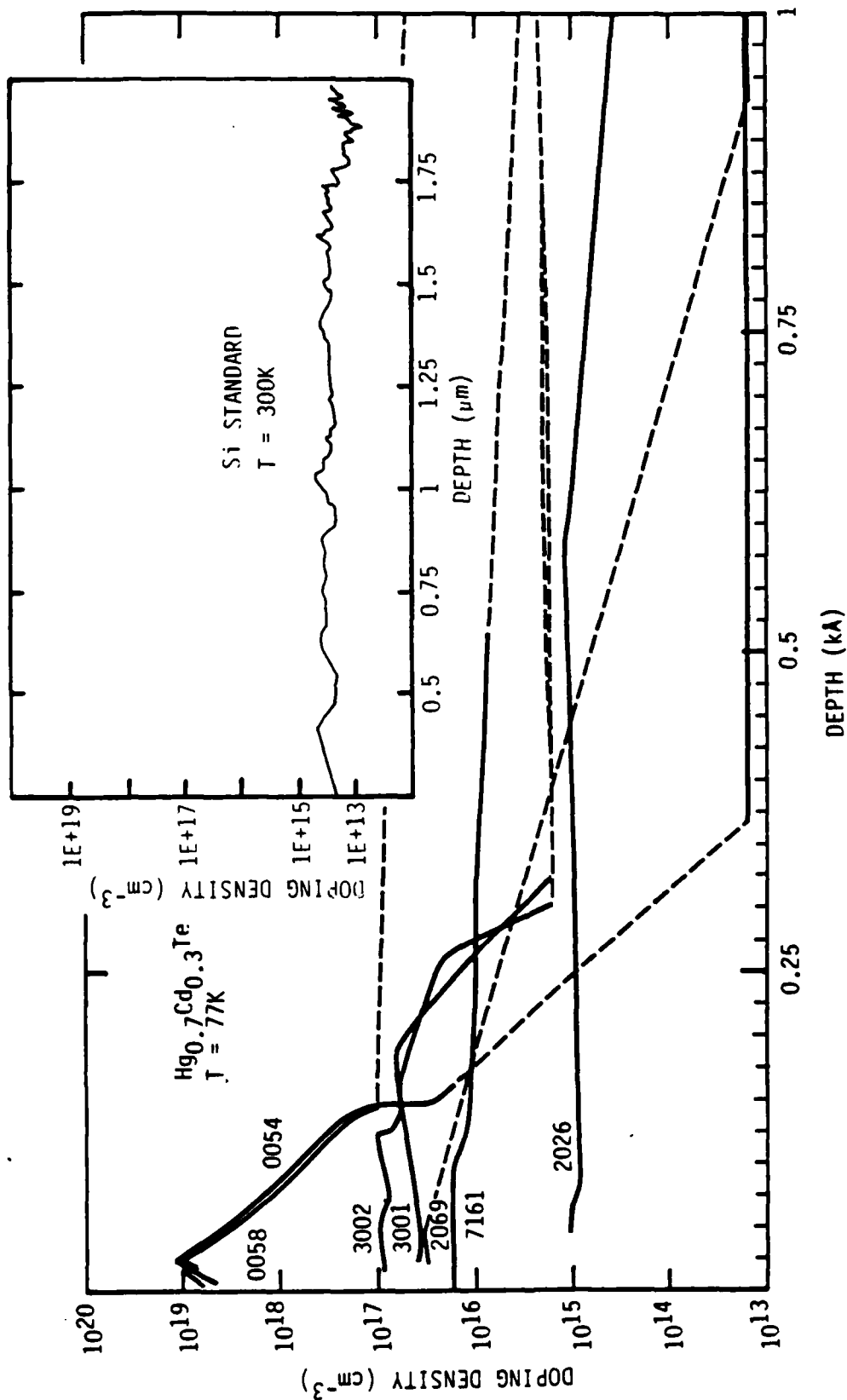


Figure 1-1. Measured Doping Density versus Depth for Distances Up to 1000 Å
 From the Insulator/ $\text{Hg}_{0.7}\text{Cd}_{0.3}\text{Te}$ Interface. Note different
 horizontal axis scales of inset.

In all cases the surface doping is higher than the bulk by over an order of magnitude while in the case of the anodic oxide the increase is nearly five orders of magnitude. It can also be seen in Figure 1-1, that this region of higher doping is almost entirely confined to the 250Å nearest the insulator interface. We also note that some of the curves are incomplete (broken lines) in that some data is not plotted between the surface and the bulk in the region where the doping is expected to be changing the most rapidly. These points are rejected during a step in the calculation of the doping density due to lack of convergence of the search routine. Physically these are regions where the variation of doping is too rapid and the algorithm used breaks down (the value of $1/C_d^2$ varies very rapidly with ϕ_s). Each point is calculated independently of neighboring points so that omission of any point has no effect on the accuracy of the others. The calculated doping profiles are reduced from the slope of the dependence of $1/C_d^2$ on ϕ_s . The calculation of $1/C_d^2$ from the data is straight forward and does not involve the same search routine so that the points missing from the doping profiles are contained in these curves.

Depletion layer capacitance was determined from the high frequency capacitance voltage data based on an MIS equivalent circuit of the form shown in Figure 1-2.⁷

High frequency measurements were made at 1 MHz which is high enough that no known HgCdTe interface state can contribute significantly.⁷ The curves of $1/C_d^2$ shown in Figures 1-3 through 1-5 are accurate for surface potentials from accumulation (C_d is infinite) through depletion to the onset of inversion. Since the doping information displayed in Figure 1-1 is contained as the slope of these curves, it is significant that the slope is not constant over the surface potential range representing depletion, to the same degree as the Si device. This indicates that the flatband condition is in general, depth dependent in HgCdTe. A single flatband bias is a useful concept in the case of Si MIS devices and is a useful approximation for most MIS devices including HgCdTe, but it is not strictly correct at these interfaces.

The value of $1/C_d^2$ versus ϕ_s for Si, shown for comparison as the inset in Figure 1-3, is essentially a straight line (the small fluctuations are again an artifact of the hand digitization used on this data) while those of the HgCdTe samples are of nonuniform slope. From the plots of $1/C_d^2$ versus ϕ_s it

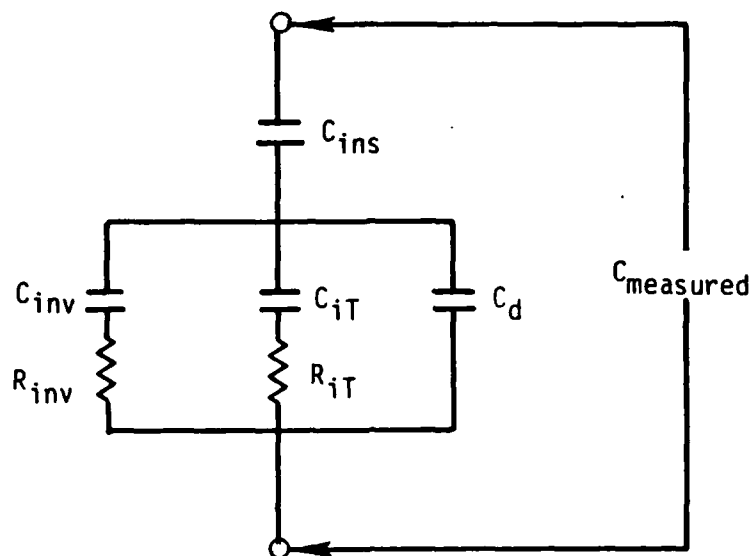


Figure 1-2. Equivalent Circuit of Measured MIS Device Showing Contributions Due to Insulator (C_{ins}), Depletion Layer (C_d), Interface Traps (C_{iT}, R_{iT}) and Inversion Layer (C_{inv}, R_{inv}).

is clear that, with the exception of 0054, there are no clear indications of general type reversal and therefore of any p-n junctions in series with the depletion layer capacitance. Type reversal would be indicated by a region where the slope changes sign. In sample 0054, Figure 1-4, there is a change of sign of the slope between $\phi_s = -0.2$ and -0.25 eV. The substrate of this anodic oxide MIS is n-type so that in this region it appears there is local type conversion. The equivalent depth of this feature in Figure 1-1 is the region beginning around 250\AA and extending another several hundred angstroms into the bulk. In general, however, the increased surface doping is of the same type as the bulk material and there is no clear evidence of a junction layer at the interface so that the damaged region is probably inhomogeneously distributed across the surface with neighboring regions being either n or p-type. This allows iro-type paths to short and heterotype barriers in general.

Since the increased effective surface doping is of the same type as the bulk, it is unlikely that it is caused directly by a damage mechanism such as that which always results in donor activity following ion implant into HgCdTe. The increased doping most likely results indirectly from damage to

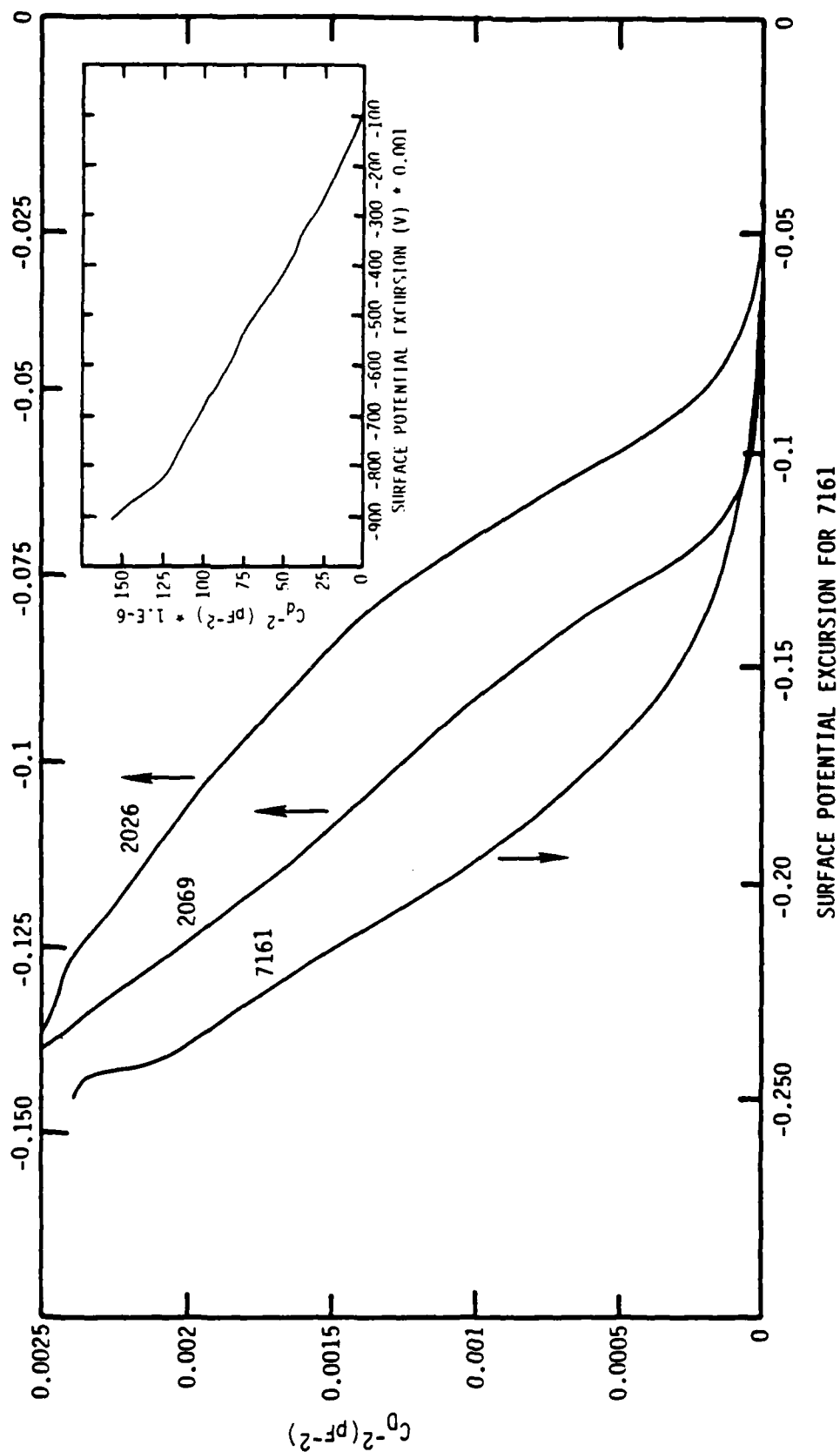


Figure 1-3. $1/C_d^2$ versus Surface Potential Excursion for MIS Devices Made With PHOTOXTM-SiO₂ on n-Type Hg_{0.7}Cd_{0.3}Te. Inset Shows Similar Data for n-Type Si MOS Device.

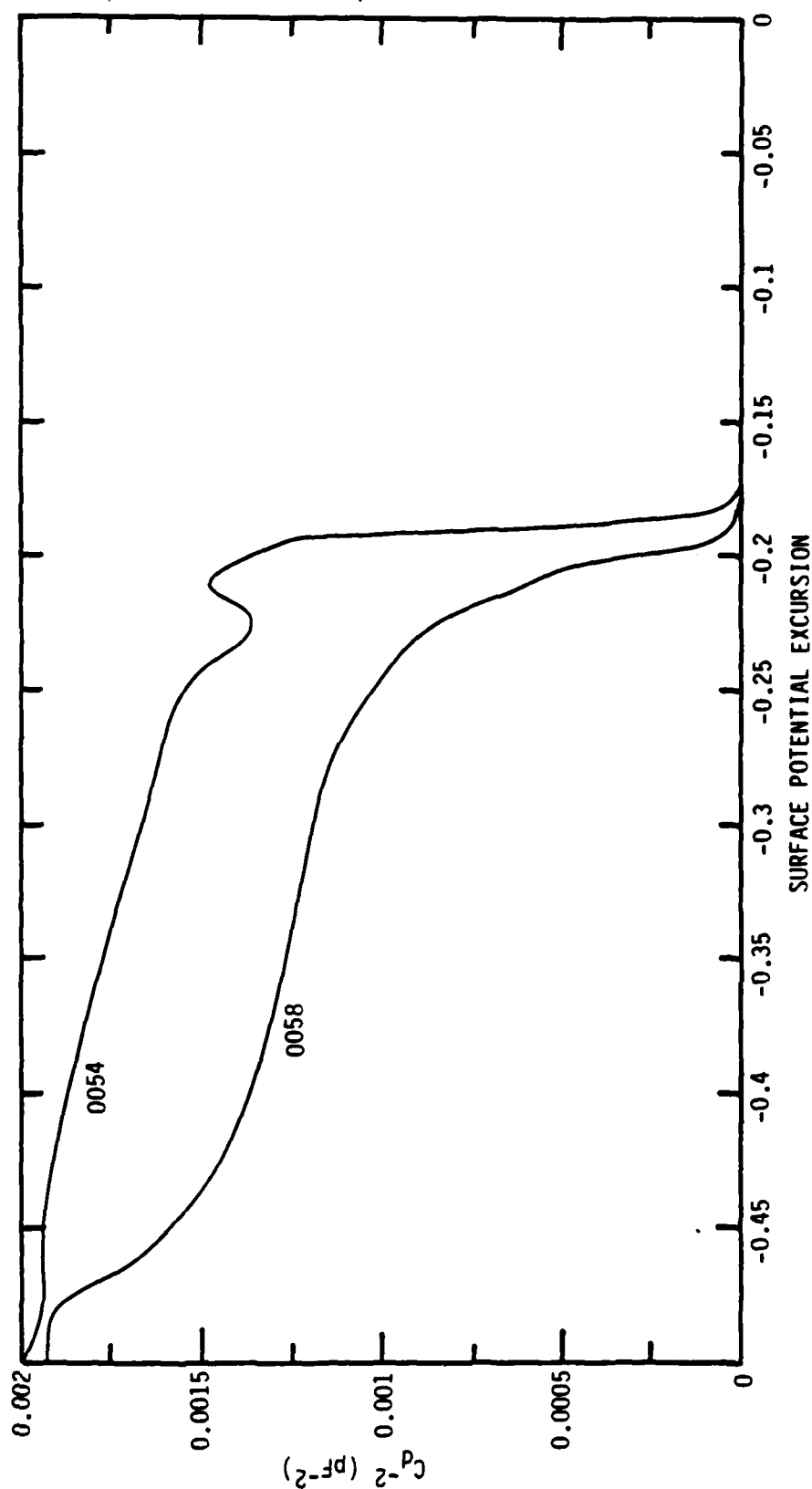


Figure 1-4. $1/C_d^2$ versus Surface Potential Excursion for MIS Devices
Made With PHOTOX™-SiO₂ on p-Type Hg_{0.7}Cd_{0.3}Te

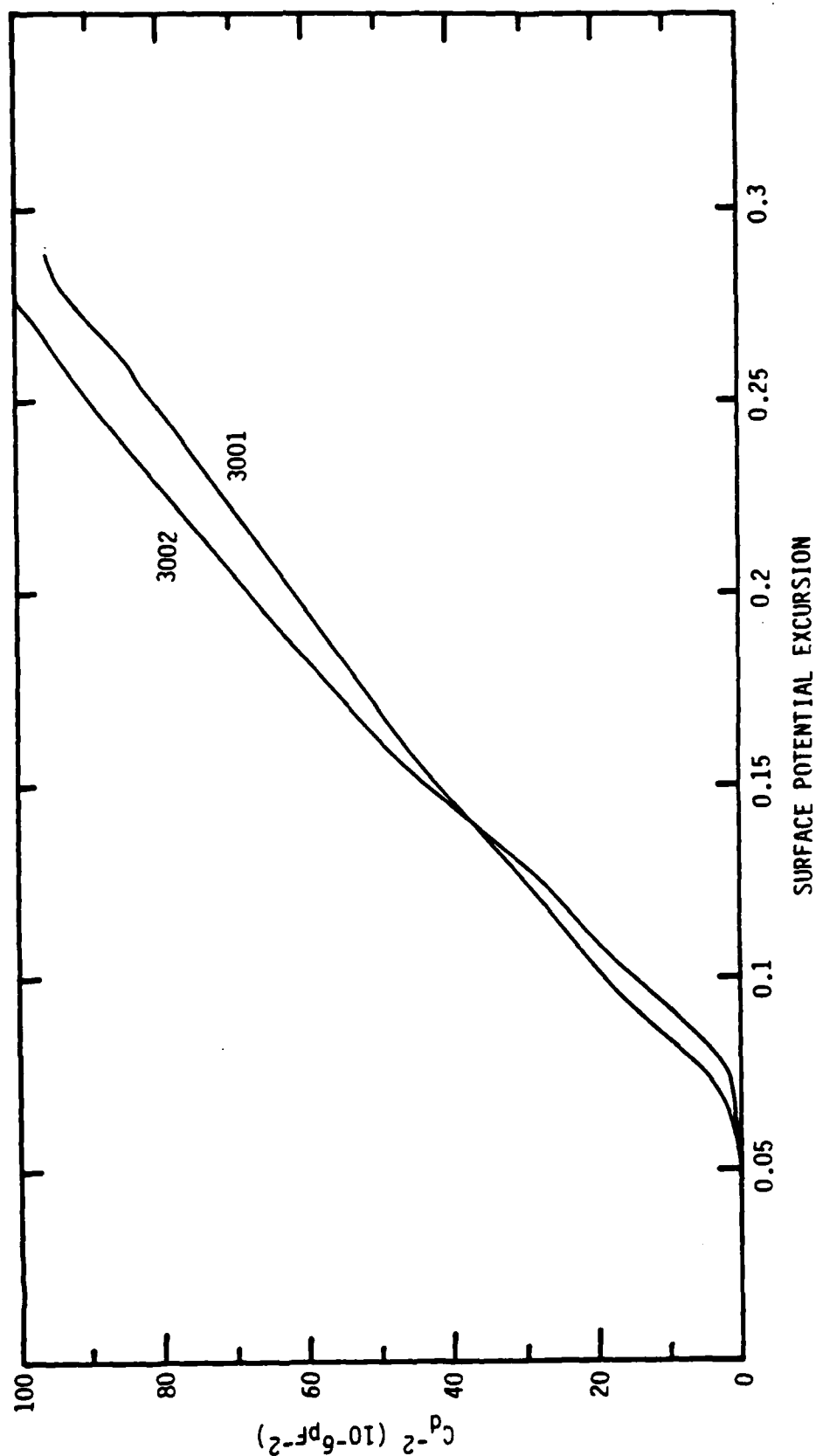


Figure 1-5. $1/C_d^2$ versus Surface Potential Excursion for MIS Devices
Made With Anodic Oxide Grown on n-Type $Hg_{0.7}Cd_{0.3}Te$

the Te lattice resulting in net alteration of the band structure in such a way that the fermi energy is relocated closer to the nearest band edge than in the undamaged bulk. We note that the effect is slightly more pronounced in p than n-type HgCdTe. However this increased effect cannot be taken by itself to indicate that the valence band edge is more strongly affected since the p-type sample were about an order of magnitude higher to start with. The effect is significantly more pronounced at the anodic oxide interface indicating that the applied PHOTOX™ SiO₂ passivation is inherently a more benign process.

As indicated in Table 1-1 the total excursion of the surface potential for these interfaces does not correspond closely to , nor vary simply from that expected from the bulk bandgap at 77 for $x = 0.3$ HgCdTe, of 0.26 eV. The PHOTOX™ interfaces on n-type wafers all show a more restricted excursion while the other cases, particularly the anodic interfaces, show a wider excursion. The surface potential excursion is the value obtained directly from Berglund integration of the quasi-static capacitance voltage curves. For MIS devices which exhibit a measurably long storage time, greater than about 2 ms, there is the possibility that the MIS device does not closely approximate equilibrium while the gate bias is ramped from accumulation to inversion. In this case the low frequency curve does not accurately represent the true quasi-static condition the derived surface potential excursion appears wider than the bulk bandgap and any surface state densities derived from this data would appear artificially low. The parts used in this study were selected to avoid bulk storage times long enough to cause this effect. Also the results obtained for bias sweeps from accumulation to inversion were compared to those for sweeps from inversion to accumulation, to avoid any nonequilibrium conditions. The nonequivalence of the surface potential excursion and the bulk energy gap is taken as a real effect of these interfaces indicating a major alteration of the interface crystal structure.

The part of the C-V curve which gives rise to these apparent increases in surface doping are seen as a very slight flattening of the curve at the transition between accumulation and depletion. This region is indicated by the arrows in Figure 6. One of the samples (2026) was chosen because the flattening is especially pronounced. Similar types of distortions of the C-V curves can occur due to the presence of discrete or very high densities of interface traps. The densities of interface traps for the devices of this study are

typical of HgCdTe with midgap minima of about 1 to $5 \times 10^{11} \text{ eV}^{-1} \text{ cm}^{-2}$ and are free of unusual densities of discrete traps. Also the degree of flattening is similar in both high frequency and quasi-static curves so that any interface state associated with this feature would have a response frequency well above 1 MHz . To a detection limit of about $5 \times 10^9 \text{ eV}^{-1} \text{ cm}^{-2}$ there are no high frequency states present at these interfaces.⁷ This type of distortion of the C-V curve cannot be due to any fundamental property of the HgCdTe lattice, such as nonparabolicity of the conduction band, since the effect varies widely in degree from device to device for material with the same composition. It is also not a peculiarity of the algorithm because the increased doping corresponds in degree to a real feature of the capacitance voltage data.

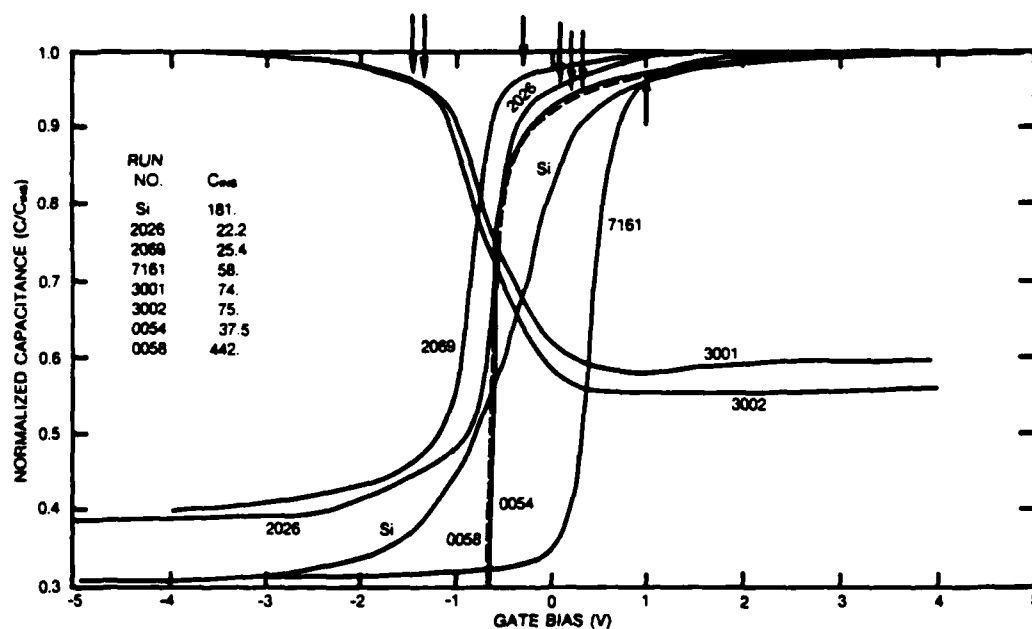


Figure 1-6. 1 MHz Capacitance Voltage Curves for the Samples Used in This Study. Arrow indicates the bias region where nonideal structure interpreted as increased near interface doping.

CONCLUSION

We have examined the dependence of doping on depth at the passivated interface of HgCdTe formed with anodic oxidation or deposited PHOTOX™ SiO₂. In all cases the doping density within 250 to 500 Å from the interface is increased sharply over that of the bulk material. Because the increased

doping is generally of the same type as the bulk, this increase is taken to be the indirect result of a fundamental inhomogeneous alteration of the Te lattice and hence its electronic band structure by the processes used to form the MIS device. As the result of this lattice distortion the bands are curved near the interface, to some extent, at any applied bias and the energy gap is changed from the bulk value. The increase in effective doping and band distortion are, hence, consequences of the weakened HgTe bond in the presence of Cd which is the fundamental cause of the ease with which this alloy is damaged.⁸ In general, passivated interfaces on HgCdTe are broader and more rich in structure than the corresponding situation on other semiconductors.

ACKNOWLEDGMENTS

We gratefully acknowledge many helpful discussions with T.N. Casselman at SBRC, F.H. Pollak at Brooklyn College, W.E. Spicer at Stanford University and A. Sher of SRI International. We also acknowledge the expert technical assistance of J.I. Mosely for assistance in programming the data reduction algorithm and finally to J.F. Santarosa and M.E. Boyd for assistance in recording the capacitance data. This work was supported under DARPA contract number MDA-903-83-C-0108. The program sponsor is R.A. Reynolds and the technical monitor is J. Murphy both of DARPA/DSO.

REFERENCES

1. G.P. Carey, A. Wahi, J.A. Silberman, C.M. Stahle, W.E. Spicer and J.A. Wilson, "Photoemission Study of Etched HgCdTe Surfaces Revealing Cd Loss," submitted to Appl. Phys. Lett.
2. A. Ksendzov, F.H. Pollak, J.A. Wilson and V.A. Cotton, "Electroreflectance Study of HgCdTe in the Metal-Insulator-Semiconductor Configuration at 77K," submitted to Appl. Phys. Lett.
3. K. Ziegler, E. Klausmann and S. Kar, Solid State Electronics, 18, 189 (1975).
4. J.A. Wilson and V.A. Cotton, J. Appl. Phys., 57, 2030 (1985).
5. C.N. Berglund, IEEE Trans. Electron. Devices, ED-13, 701 (1966).
6. A. Sher, H.J. Hoffman, Pin Su and Y.H. Tsuo, J. Appl. Phys., 54, 5183 (1983).
7. G.H. Tsau, A. Sher, M. Madou, J.A. Wilson, V.A. Cotton and C.E. Jones, J. Appl. Phys., 59, 1238 (1986).

HUGHES

SANTA BARBARA RESEARCH CENTER
a subsidiary

8. A. Sher, A.B. Chen, W.E. Spicer and C-K Shih, J. Vac. Sci. Technol., A3, 105 (1985).

HUGHES

SANTA BARBARA RESEARCH CENTER
a subsidiary

(THIS PAGE INTENTIONALLY LEFT BLANK)

HUGHES

A HUGHES COMPANY

SANTA BARBARA RESEARCH CENTER
a subsidiary

Section 2
CHANNELED IMPLANT TASK

2.1 CHANNELED ION IMPLANTATION RANGE STUDIES IN HgCdTe

INTRODUCTION

We have measured the depth distributions for elements of interest as potential dopants implanted in the {111} random and the {110} channeling orientations of HgCdTe using secondary ion mass spectrometry (SIMS). The HgCdTe material used was preannealed solid state regrown (SSR). The elements studied were all of odd Z, taken from columns 1, 3, 5, and 7 of the periodic table, namely H, Li, Na, K, Cu, B, Al, Ga, In, N, P, V, As, Sb, F, Cl, Mn, and Br, plus Be. The implantation energies were 150 or 200 keV. The implant fluences were mostly $3 \times 10^{13} \text{ cm}^{-2}$, with extrapolation to $1 \times 10^{15} \text{ cm}^{-2}$ because of SIMS measurement technology. Alignment for the channeled implants was performed by using Rutherford backscattering of protons. We have determined the range parameters, R_p , ΔR_p , maximum channeling range R_c , and the shape factors or third and fourth moments, γ_1 and β_2 , by performing pearson IV fitting routines to the experimental depth distributions. Sufficient detection sensitivity using SIMS was achieved to determine many {110} channeling ranges, which vary substantially and reflect the Z_1 -dependent electronic stopping S_e . Some channeling ranges in the large {110} channel of HgCdTe are from 6 to 50 μm for 200 keV ion energies.

When ions are channeled in a crystal, they lose energy by electron interactions, not by nuclear collisions. Therefore they do not cause displacement damage or vacancy-interstitial pairs, until near the end of their range when they have lost all but the last few keV of energy. Therefore, channeled ion implantation does less damage in the deeper channeled region of the implanted depth distribution. Damage is still done in the surface region by ions that do not enter channels that contribute to the random component of a channeled depth distribution.

The motivation for this work was to determine implantation range parameters and depth distributions for selected elements implanted in both the random and the open {110} channeled orientations of HgCdTe crystals that would be used to fabricate devices. In particular, we desired to learn how deep these selected ions channel and what atom densities can be achieved in the deep channeled regions, with the idea that the damaged surface region could be etched away to leave a less damaged region that might be chemically doped rather than defect doped. The random range parameters and profiles are

important for understanding standard implantation technology. Establishing a valid SIMS technology for profiling in HgCdTe was another goal and result of this work.

Implantation of the lighter elements into HgCdTe was emphasized because implant depths are deeper and less implant damage is caused in the HgCdTe compared with higher atomic number (Z_1) elements. Therefore, elements were selected for implantation from the first four rows of the periodic table, through Br ($Z_1 = 35$), except for In and Sb, and only odd Z_1 elements were studied (columns 1, 3, 5 and 7). All odd Z_1 elements through Br were attempted, that is, were implanted in the {111} random and {110} channeling orientations. In addition, In ($Z_1 = 49$) was implanted in the random and channeling orientations, and Sb ($Z_1 = 51$) was implanted in the random orientation, because they are used as implantation and melt-grown dopants in HgCdTe in the industry.

EXPERIMENTAL TECHNIQUES AND ACCURACIES

The samples of HgCdTe used in this work were polished solid state regrown {111} and {110} oriented material annealed for three or four weeks at 350°C and etched to remove surface damage. All ions were implanted at room temperature with current densities below 2 nAcm^{-2} , so beam heating was insignificant. Ion energies are accurate to within 2%, and ion fluences, to within about 10%.

The channeled implants were performed by first aligning the HgCdTe crystal direction with the incident ion beam direction to within 0.1 degree using Rutherford backscattering of protons, and then implanting the selected ions to the desired fluences. The angular divergence of the ion beam during scanning was ± 0.1 degree. For the random implants, {111} wafers were tilted 7 or 8 degrees about an axis from which a flat was rotated 18 degrees when a directional flat was apparent, which was not always. In those cases, the azimuthal rotation was random.

Secondary ion mass spectrometry (SIMS) measurements were made using either an oxygen primary ion beam and positive ion spectrometry, or a cesium ion beam and negative ion spectrometry. Sputtering rates were between 3 and 10 nm/s. The depth scales of SIMS profiles were determined from surface profilometry (Dektak) measurements of the crater depths; the error in the

depth scales is about $\pm 7\%$. The atom densities were determined by setting the integrals of these unannealed depth profiles equal to the ion fluences.

EXPERIMENTS

Several implantation studies were carried out under this program. The first was an exploratory study that comprised implanting several selected ions in the $\{111\}$ random and $\{110\}$ channeling orientations of HgCdTe at 150 keV and $3 \times 10^{13} \text{ cm}^{-2}$. The ions in this group were Be, B, F, Na, Al, Cl, and K. The $\{110\}$ channeling depth distributions measured using SIMS are shown in Figure 2-2. Channeling ranges are seen to vary from near 2 μm for B to about 6 μm for F, and an undetermined depth greater than 7 μm for Na. The corresponding $\{110\}$ random profiles are shown in Figure 2-3. These $\{110\}$ random profiles exhibit significant channeling tails.

Next, H was studied because little damage is done to the HgCdTe by this light ion and greater random ranges can be achieved than for heavier ions. Implanted H had been shown to produce p-j junctions in HgCdTe. H is a difficult element to profile using SIMS so a significant SIMS technology study was required. We were successful and the results were published in an Applied Physics Letter.¹ Subsequently, H, as ^1H and ^2H , was channeled in the $\{110\}$ direction of HgCdTe and one profile is included in Figure 2-2 for comparison with the other depth distributions shown there. The channeled ^2H profile is compared with a $\{111\}$ random profile in Figure 2-4. H is seen to have a channeling range greater only than B, and shallower than the other six in this group of elements.

The third set of implants studied comprised the 18 elements from columns 1, 3, 5, and 7 of the partial periodic table shown in Figure 2-1, and that are potential dopants in HgCdTe. These 18 elements were implanted at 200 keV in the $\{111\}$ random and the $\{110\}$ channeling orientations of preannealed SSR HgCdTe. $\{110\}$ channeling profiles are shown for some of these elements in Figure 2-5, to a depth of 5 μm . The $\{110\}$ channeling profiles that are deeper than 5 μm are shown separately for individual elements in Figure 2-6 for Li, Figure 2-7 for F, Figure 2-8 for Na and Figure 2-9 for Al. Other channeled depth distributions are shown in Figure 2-10 for Cl, in Figure 2-11 for K, in Figure 2-12 for Br, and in Figure 2-13 for In. In is of interest because of its recent use as a dopant in HgCdTe. The good detection limits for these

H							He
Li	(Be)	B	C	N	O	F	Ne
Na	Mg	Al	Si	P	S	Cl	Ar
K	Ca	Sc	Ti	V	Cr	Mn	Fe Co Ni
Cu	Zn	Ga	Ge	As	Se	Br	Kr
	\triangle Cd	In		Sb	\triangle Te		
	\triangle Hg						

Figure 2-1. Partial Periodic Table of the Elements, Showing the First Four Rows (Through Kr) Plus In and Sb and the Three Substrate Components, Hg, Cd, and Te. The potential dopants in columns 1, 3, 5 and 7, which were also the ions implanted and profiled in this work, are outlined in boxes.

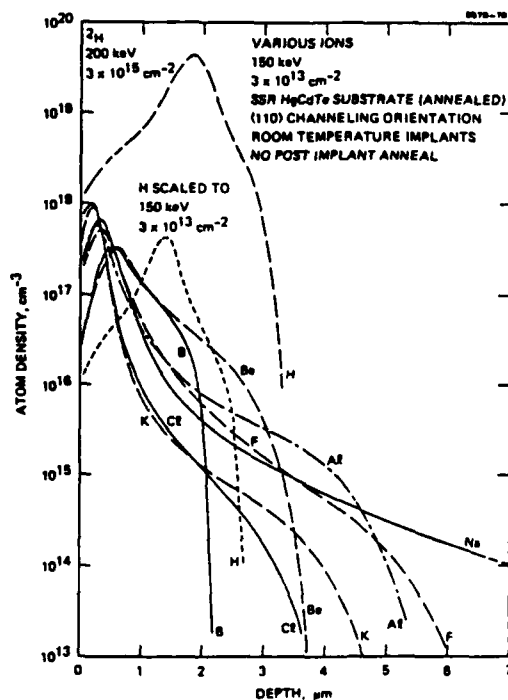


Figure 2-2. Channeled Depth Distributions for Selected Ions Implanted in the {110} direction of HgCdTe at 150 keV

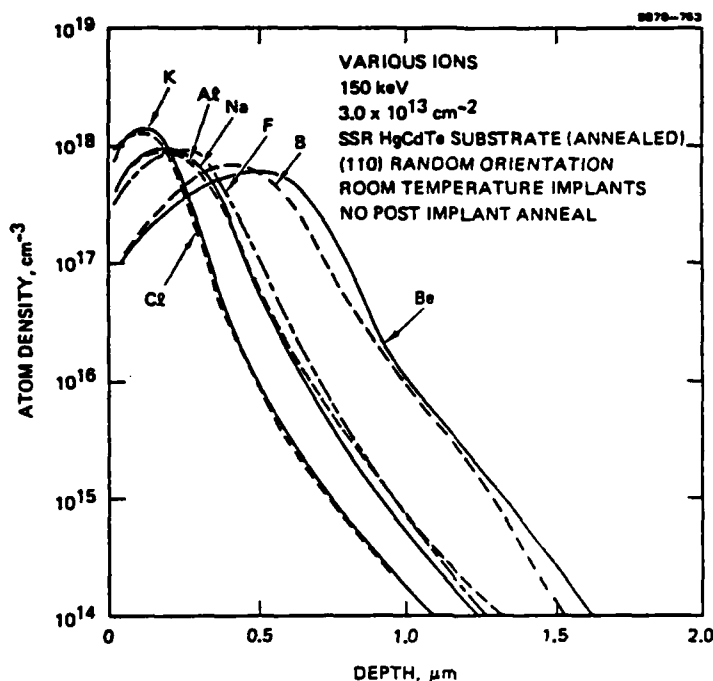


Figure 2-3. Random Depth Distributions for Selected Ions Implanted in {110} HgCdTe at 150 keV

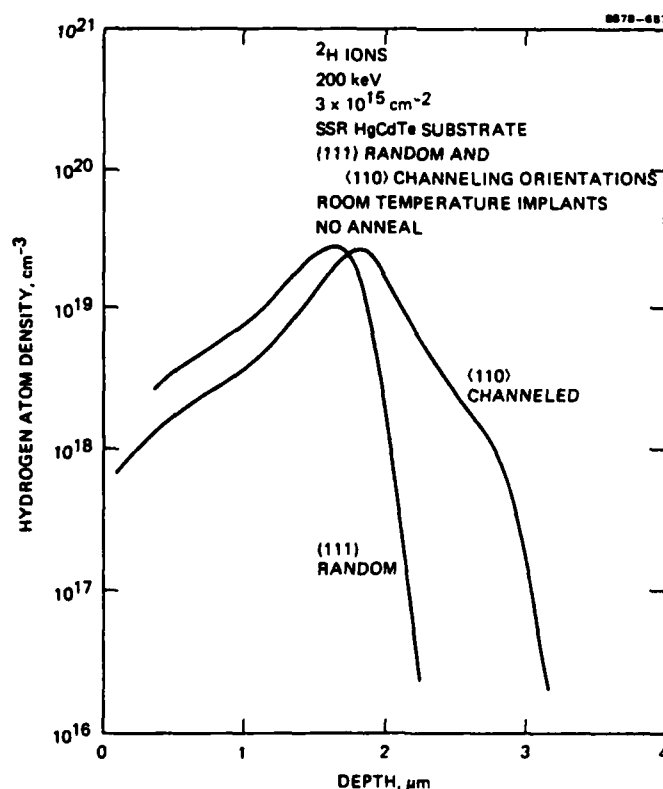


Figure 2-4. {111} Random and {110} Channeled Depth Distributions for ^2H Ions Implanted in HgCdTe at 200 keV

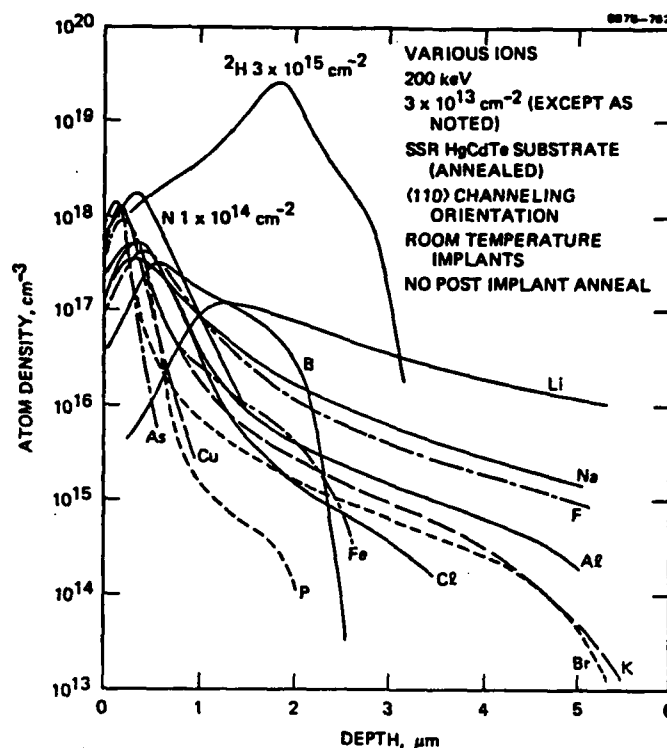


Figure 2-5. Channelled Depth Distributions for Selected Ions Implanted in the {110} Direction of HgCdTe at 200 keV (to 5 μm)

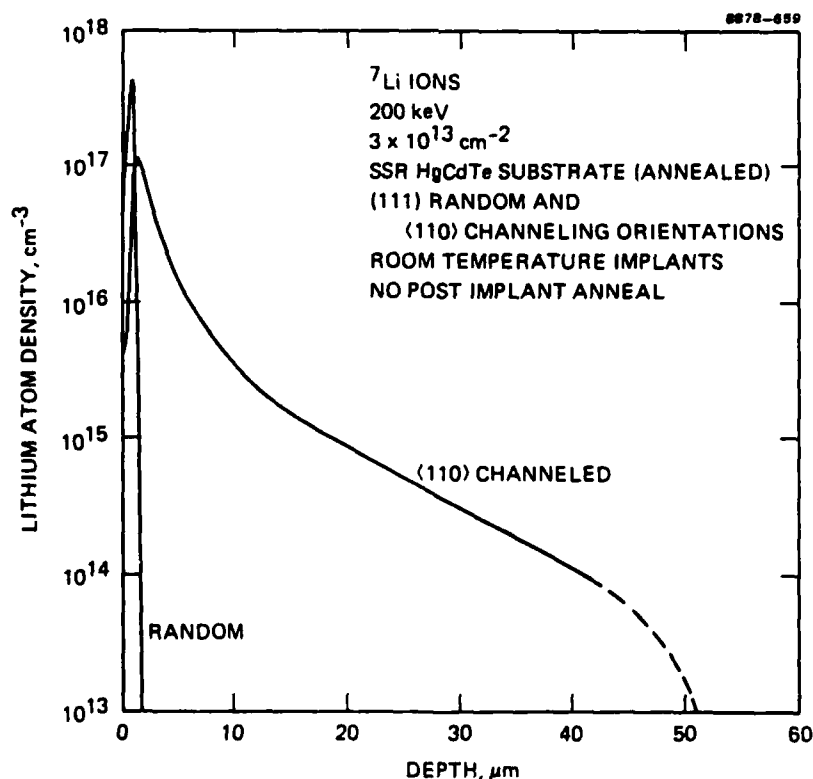


Figure 2-6. {111} Random and {110} Channelled Depth Distributions for Li Implanted in HgCdTe at 200 keV

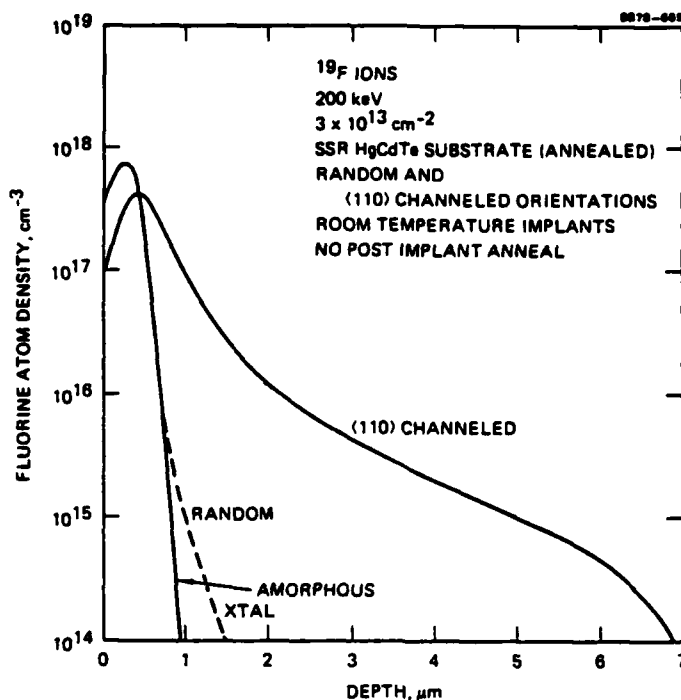


Figure 2-7. {111} Random and {110} Channelled Depth Distributions for F Implanted in HgCdTe at 200 keV

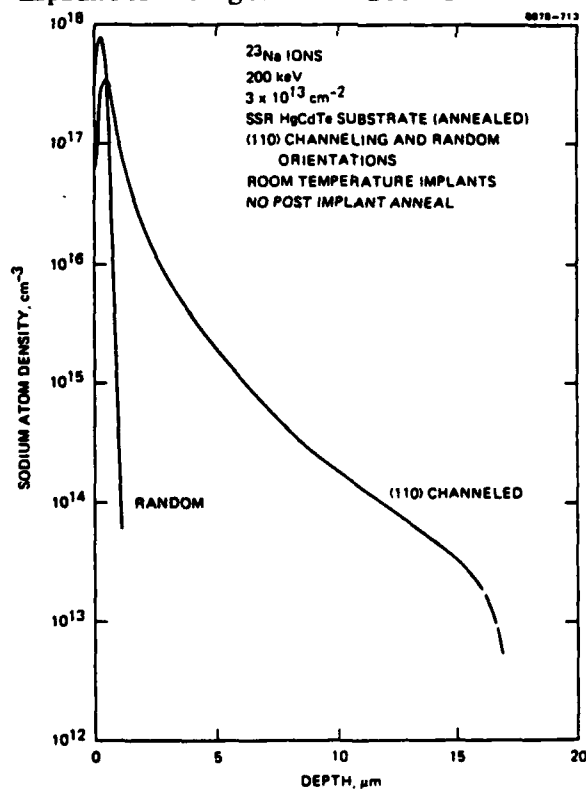


Figure 2-8. {111} Random and {110} Channelled Depth Distributions for Na Implanted in HgCdTe at 200 keV

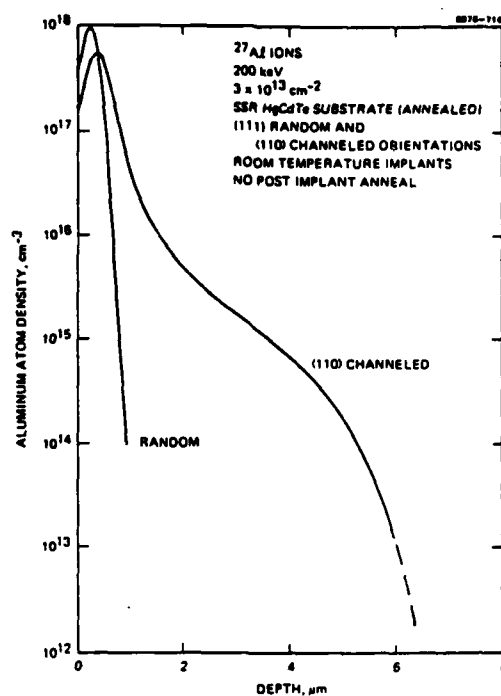


Figure 2-9. {111} Random and {110} Channeled Depth Distributions for Al Implanted in HgCdTe at 200 keV

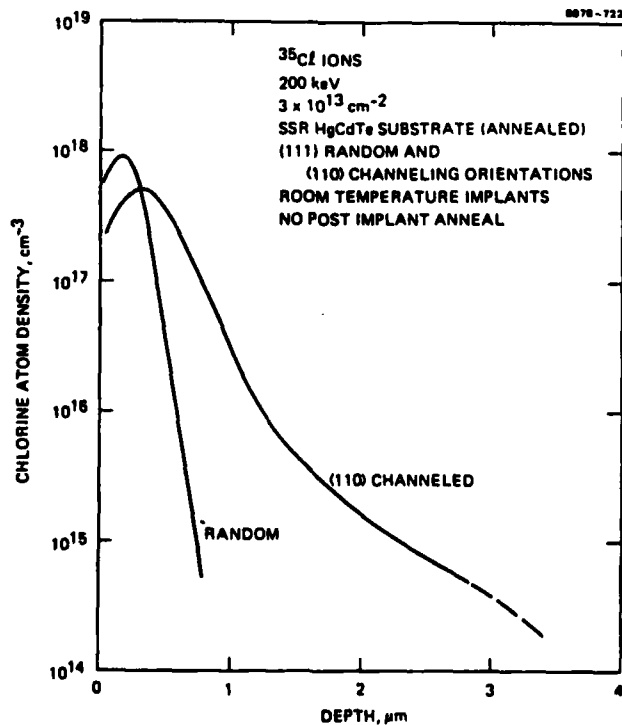


Figure 2-10. {111} Random and {110} Channeled Depth Distributions for Cl Implanted in HgCdTe at 200 keV

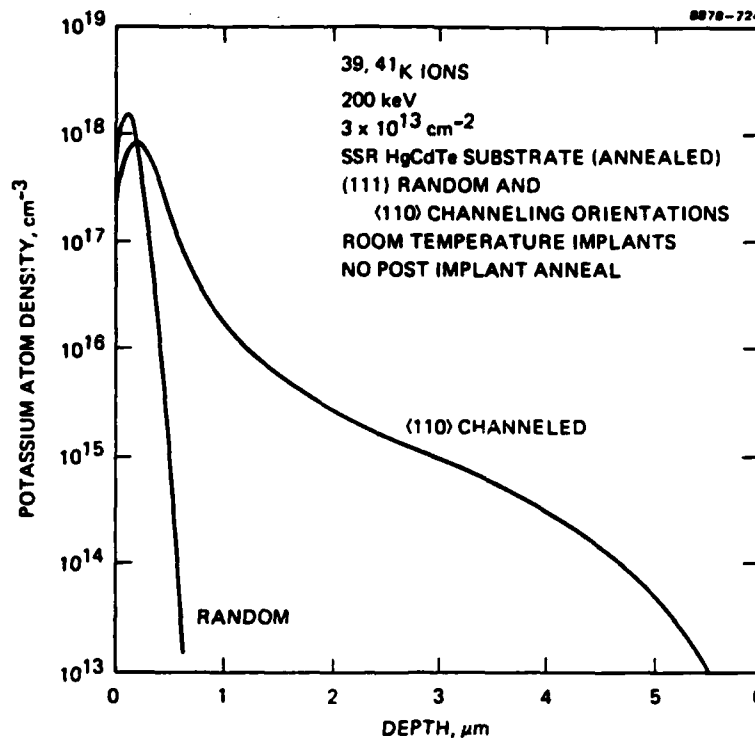


Figure 2-11. {111} Random and {110} Channeled Depth Distributions for K Implanted in HgCdTe at 200 keV

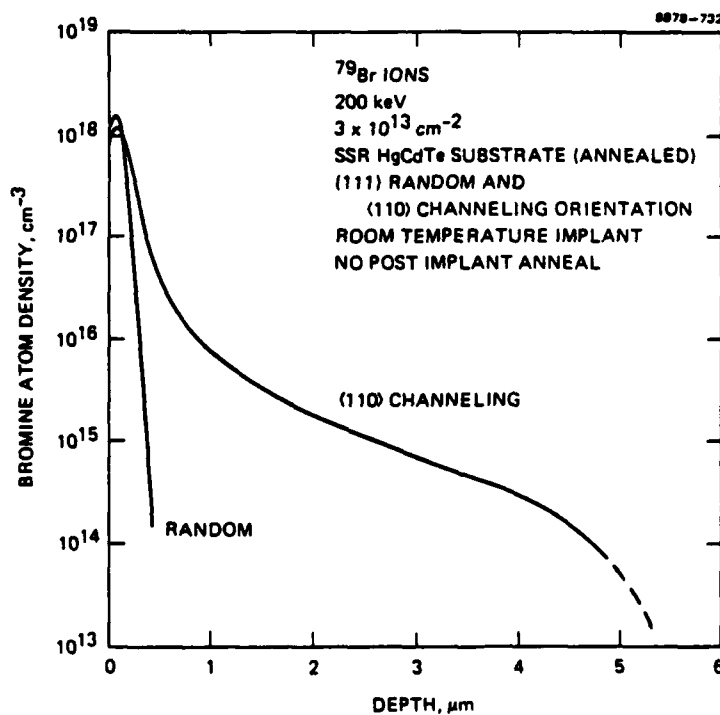


Figure 2-12. {111} Random and {110} Channeled Depth Distributions for Br Implanted in HgCdTe at 200 keV

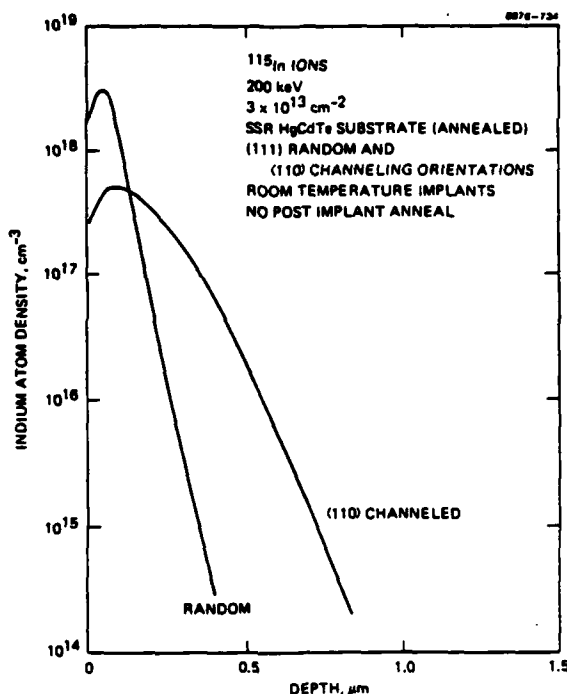


Figure 2-13. {111} Random and {110} Channeled Depth Distributions for In Implanted in HgCdTe at 200 keV

ions using SIMS allow these profiles to be measured even though the maximum channeling ranges are observed only for atom densities less than 10^{14} cm^{-3} , or a few parts per billion.

The final group of implants performed under this program was a set of selected ions implanted at 200 keV but at $1 \times 10^{13} \text{ cm}^{-2}$ to be used at SBRC for capacitance-voltage profiling. These ions and the electrical results are reported elsewhere in this final report. Two full {110} HgCdTe wafers were implanted in the channeling orientation with each ion.

The maximum channeling ranges for Be and Cl are seen in Figure 2-2 to be approximately the same ($\sim 3.7 \mu\text{m}$) at 150 keV, but a much larger fraction of the implanted Be ions exist in the deep channeled portion of the profile. These observations illustrate that the electronic stopping S_e of Be and Cl at 150 keV are nearly identical, accounting for the nearly identical channeling ranges, but the small size of the Be ion compared with the Cl ion accounts for the larger fraction of more deeply channeled Be ions. Fewer ions are dechanneled as they proceed through the HgCdTe lattice. Na is seen to be an example of a small ion with a small electronic stopping, so Na channels deeply. B is

a small ion with a relatively high value of electronic stopping, so it channels well but not deeply. Large ions with high electronic stopping show relatively little channeling profile, as is the case for some of the higher Z ions studied.

We measured a Rutherford backscattering χ_{\min} of 7.2% in the $\{110\}$ direction for the SSR HgCdTe material, which is a figure of merit for the crystal quality of the substrate material. Values of χ_{\min} quoted by Bahir and Kalish^x for the $\{100\}$ of HgCdTe vary from 20 to 30%. Channelled ion depth distributions may be another way to measure the crystal quality, in this case, by examination of $\{110\}$ channelled profiles. The presence of Hg interstitials, for example, would block the channels and prevent channeling ions from reaching their maximum range, or contribute to an increased dechanneled portion of the channelled depth profile. We studied this possibility briefly by measuring channelled B profiles in HgCdTe substrates prepared under various annealing and etching conditions as illustrated in Figure 2-14. The data in this figure indicate that the crystal quality of λ substrates that are annealed and either standard or deep ($\sim 20 \mu\text{m}$) etched are the same within experimental accuracy and are both better than unannealed crystals. The long anneal is performed to convert the n-type as-grown material to p type.

The results of another experiment are shown in Figure 2-14. 200-keV B was implanted into HgCdTe in the $\{110\}$ channeling orientation of HgCdTe at doses of 1×10^{13} , 3×10^{13} , and $1 \times 10^{14} \text{ cm}^{-2}$ to determine at what atom density the channeling profile saturates for B in HgCdTe. This saturation is caused by blocking of the channels by interstitials that result from implantation damage. This saturation is seen to occur at about 10^{17} cm^{-3} (at about $2 \mu\text{m}$), or for a fluence of about $5 \times 10^{13} \text{ cm}^{-2}$. This saturation occurs at lower fluences for heavier ions and the profiles for all ions heavier than B shown in this work illustrate the saturation density for $\{110\}$ channeling because the implant fluences were $3 \times 10^{13} \text{ cm}^{-2}$.

SIMS profiles of implants into LPE HgCdTe were less consistent and had poorer backgrounds than profiles measured in the SSR material used in this work. Occasionally, profiles in LPE HgCdTe were ragged as if there were internal interfaces, inclusions or complexes within the LPE layers.

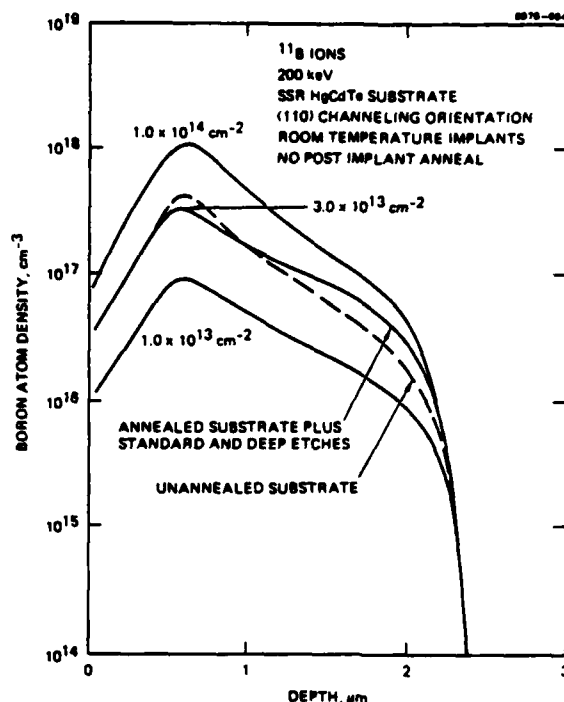


Figure 2-14. Channeled Depth Distributions for 200 keV B Implanted into Different HgCdTe Substrates

SIMS MEASUREMENT TECHNOLOGY

Some problems were encountered with the SIMS measurement technology. High backgrounds of some elements were encountered in various HgCdTe materials, especially in LPE material. Solid state regrown (SSR) material and vertical Bridgman (VB) material exhibited lower background of most elements. The many isotopes of Cd, Te, and Hg, and their molecular combinations, and the combination of all of those with oxygen cause interferences with certain ions that can easily be determined. This problem is much less significant for negative SIMS using Cs because Cd and Hg do not yield negative ions, and there are no doubly ionized negative ions. In positive SIMS, all of these ions exist in substantial quantities and their doubly ionized components interfere with an additional set of elements. To learn all that we could and to optimize detection sensitivity, we profiled all elements with both positive O SIMS and negative Cs SIMS, and with and without offset voltages in many cases where interferences were observed, to suppress molecular interferences.

The systematic measurement of profiles of implanted elements using O and Cs beams in a Cameca SIMS instrument performed under this program and a

parallel IR&D program has led to one serious observation. The substantially higher energy (14 keV) of the more massive Cs ions (133 amu) compared with the O ions (4 keV and 16 amu) causes enough greater forward momentum/energy transfer and impurity substrate mixing to cause the depth distributions to be significantly skewed to the deep side compared with the O SIMS profiles. The widths of the depth distributions obtained using a Cs beam are too large and the deep sides of the profiles extend too deeply into the HgCdTe substrate. While there may be some small effect for 4-keV O, it is believed to be negligible. The profiles for elements beginning at about the transition I metals measured using Cs SIMS yield values of R_p that are slightly too large (assuming O profiles are to be correct), values of ΔR_p that are too large, values of the third moment γ_1 that are too positive, and what appear to be channeling tails when none or much smaller ones are shown using O. The errors in depth approach about 40% as the Z of the impurity approaches 73, Ta, the heaviest element studied.

The profiles reported here were all obtained using positive O SIMS except in cases where a comparison showed Cs profiles not to be very distorted, especially when more dynamic range was achieved using Cs SIMS, which was rarely. This limitation is not severe because all elements can be profiled using O SIMS; only some elements with high ionization potentials yield poor sensitivity using O SIMS and these are primarily the noble gases. Most of the elements in columns 4, 5, 6, and 7 profile quite well using O SIMS, in some cases, better than can be achieved using Cs SIMS. Cs SIMS is not able to measure depth profiles for the elements with zero or very small electron affinity (under the experimental conditions). The sensitivity factors for SIMS do not follow the often assumed rule of proportionality between ionization potential or electron affinity and log sensitivity factor for ionization potentials above 9 eV or for large values of electron affinity, for some substrates (which do not include HgCdTe). As part of this program and a parallel IR&D program, we have measured sensitivity factors for about 45 elements (from H to Ta) implanted in HgCdTe using both O and Cs SIMS and plotted them versus ionization potential and electron affinity. It is from the results of these studies that the observations, conclusions, or statements made above are drawn.

In a few cases, molecular ions comprised of the ion of interest and one from the substrate or the primary ion beam were studied. More work could be done in this area, to optimize the measurement technology, if it were deemed significant enough to expend the funds. We achieved sufficient detection sensitivity to obtain channeling profiles for some but not all of the 18 elements of interest (plus Be). high backgrounds were often encountered for P and Cl.

DISCUSSION

Ion energies studied were 150 and 200 keV, energies compatible with commercial implanters and standard in the industry, and for some of the heavier ions, 250, 300, or 400 keV. Ion fluences for channeled profiles were generally $3 \times 10^{13} \text{ cm}^{-2}$, but $1 \times 10^{13} \text{ cm}^{-2}$ was used in some cases for samples that were subsequently used for electrical measurements, for example, capacitance-voltage. Ion fluences studied for random implants varied from 1×10^{13} to $5 \times 10^{14} \text{ cm}^{-2}$, except for H, for which 3×10^{14} and $3 \times 10^{15} \text{ cm}^{-2}$ gave better profiles using SIMS, because of the high background of H in HgCdTe and interference from the vacuum ambient. H is so light that the implant damage is comparable for this higher fluence. D has such good detection sensitivity that it can be profiled as a substitute for H at lower fluences. These fluences produce densities toward the high end of the range of interest for device fabrication in the random portion of implantation depth distributions, but the densities produced in the deeper channeling portion of the profiles (10^{13} to 10^{17} cm^{-3}) are of interest for device fabrication. The column 5 elements were especially difficult to SIMS in HgCdTe. N exists in the HgCdTe and in the vacuum ambient. P, As, and Sb exhibited high backgrounds in HgCdTe, largely from interferences.

Suitable random profiles were obtained for all 19 elements studied. Channeling profiles were not attempted for Sb. Channeling profiles were difficult to study for Cu and Ga because of interferences from doubly ionized Te and the oxide of Te, respectively.

CONCLUSIONS

We achieved all of our goals for this study, with the exception of being able to obtain adequate SIMS detection sensitivity to measure {110} channeled

profiles for a few of the ions selected for implantation. We were able to profile H in HgCdTe and obtained both random and {110} channeled depth distributions. We were able to implant and to SIMS profile the 18 elements selected as potential dopants in HgCdTe from columns 1, 3, 5, and 7 of the periodic table. The resulting channeled depth distributions and ranges exhibited the significant effects of the Z_1 -dependent electronic stopping seen for a Si substrate. We determined what channeled depths and associated doping densities can be achieved for {110} channeling and the ranges and other range parameters for {111} random implantation. Maximum {110} channeling ranges vary from 2 to 50 μm for 200 keV implantation energy, and saturation atom densities in the deep channeled region vary from 10^{18} cm^{-3} for H and 10^{17} cm^{-3} for B to 10^{14} cm^{-3} for the heavier ions that channel deeply. We determined that preannealed HgCdTe material has a better crystal quality than unannealed material (via the degree of B ion channeling), and that material subjected to standard and deep etching are of equivalent quality, as measured by this criterion. We measured a Rutherford backscattering χ_{min} of 7.2% for our HgCdTe material in the {110} direction. We found that LPE HgCdTe is of poorer quality than SSR HgCdTe; we observed higher impurity backgrounds, poorer consistency, and apparent buried interfaces and inclusion. We implanted a number of full wafers of HgCdTe with selected ions in the {110} channeling orientation for electrical measurements to be made at SBRC. We learned much about measuring depth distributions in HgCdTe using SIMS and established a SIMS technology in HgCdTe. This technology requires the use of O SIMS rather than Cs SIMS for profiling elements heavier than about Fe. We found that SIMS sensitivity factors do not follow the rule of proportionality between log sensitivity factor and ionization potential or electron affinity.

REFERENCES

1. R.G. Wilson, Appl. Phys. Lett. 45, 107 (1984)
2. G. Bahir and R. Kalish, J. Appl. Phys. 54, 3129 (1983)

2.2 DOPING PROFILES OF CHANNELED ION IMPLANTATION INTO $\text{Hg}_{0.7}\text{Cd}_{0.3}\text{Te}$

Introduction

This task pursued obtaining higher resolution doping profiles of HgCdTe wafers implanted in the channeling $\{110\}$ direction. A comparison is made between the damage-induced donor levels and the implanted species level. This provides some insight into the damage mechanism and separation of nuclear versus electronic stopping.

Sample Preparation and Experiment

An ingot of $X = 0.3$ HgCdTe grown by Solid State Recrystallization, was oriented and sliced to expose the $\{110\}$ surface. These wafers were then polished to remove saw damage and implanted with various ions at 200 keV to a dose of $1 \times 10^{13} \text{ cm}^{-2}$. Ions studied were H, Be, O, Cl, P, Si and In. A dip etch was used to obtain a tapered surface. Etching while pulling the wafer out at a constant rate results in the far edge, which sees the etch longest, having the most material removed. The nearest edge transitions smoothly to the original surface. The final amount of material removed from the far edge was $2.75 \pm 0.25 \text{ } \mu\text{m}$ (the wafers are about 1 cm in diameter) for H, Be and Cl, and $5.0 \pm 0.5 \text{ } \mu\text{m}$ for O, P, Si and In. The wafers then received 1500Å of PHOTOX[™] SiO_2 and deposition of 400Å Ti followed by 4000Å Au to form capacitors with an area of $4 \times 10^{-4} \text{ cm}^2$ and a center-to-center capacitor separation of 145 μm . This gives a change in depth probed per capacitor of $4.5 \times 10^{-2} \text{ } \mu\text{m}$ and $9.1 \times 10^{-2} \text{ } \mu\text{m}$ for the two etch depths. Capacitance-voltage data was then taken at 1 MHz to yield $|N_D - N_A|$ versus depth. The background donor level due to residual impurities is $\sim 3 \times 10^{15} \text{ cm}^{-3}$.

Results

Figures 2-15 through 2-21 show depth profiles of $|N_D - N_A|$ from C-V compared to the implant species concentration from SIMS for H, Be, O, P, Cl, Si and In, respectively. The first thing to be noted as the transition is made toward heavier, larger atoms is the decrease in the channeled portion of the SIMS curve. All samples have some random component due to the impossibility of all incoming ions being channeled. For larger ions more collide with the lattice at the surface rather than being channeled. There are significant exceptions to this, however. Both Si and O show minimal channeling while H and Be (which are lighter) and Cl and P (which are heavier) show a fair amount

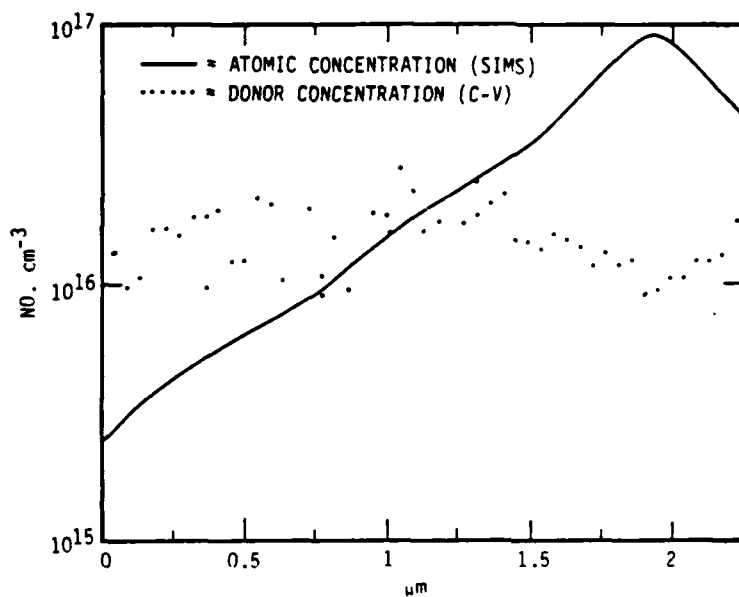


Figure 2-15. Atomic and Donor Concentration Depth Profiles for Hydrogen

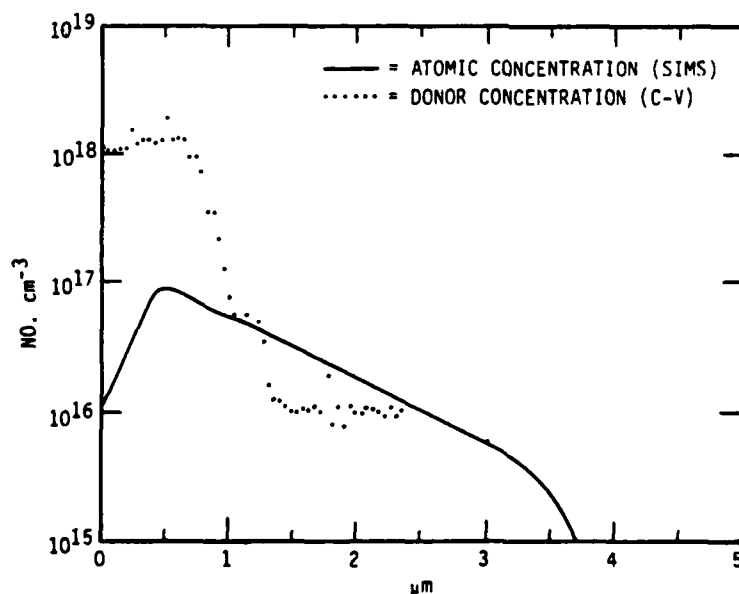


Figure 2-16. Atomic and Donor Concentration Depth Profiles for Beryllium

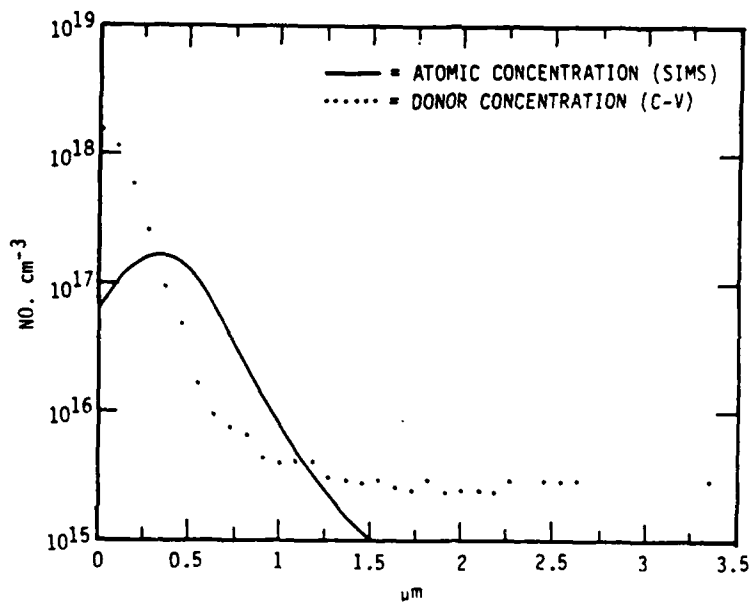


Figure 2-17. Atomic and Donor Concentration Depth Profiles for Oxygen

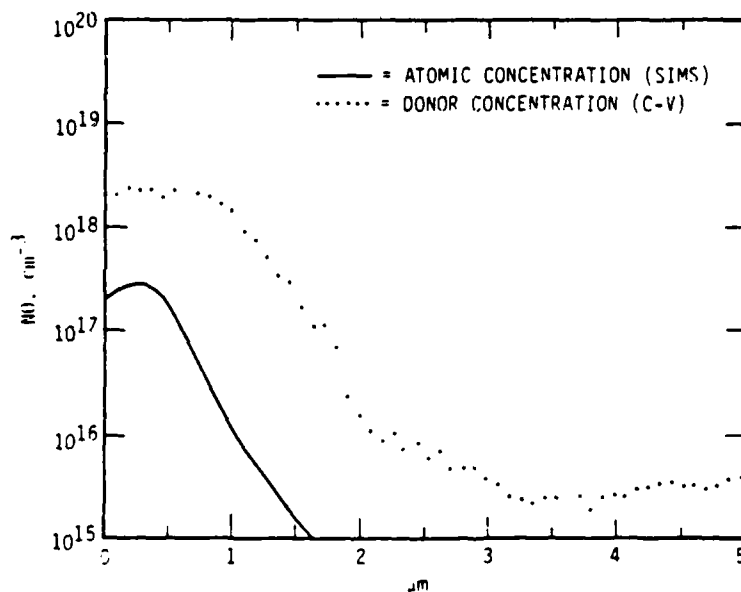


Figure 2-18. Atomic and Donor Concentration Depth Profiles for Silicon

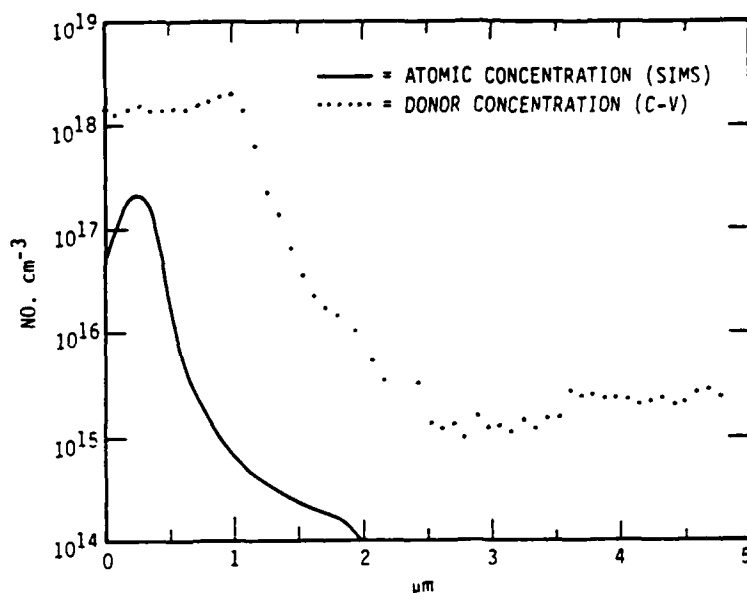


Figure 2-19. Atomic and Donor Concentration Depth Profiles for Phosphorus

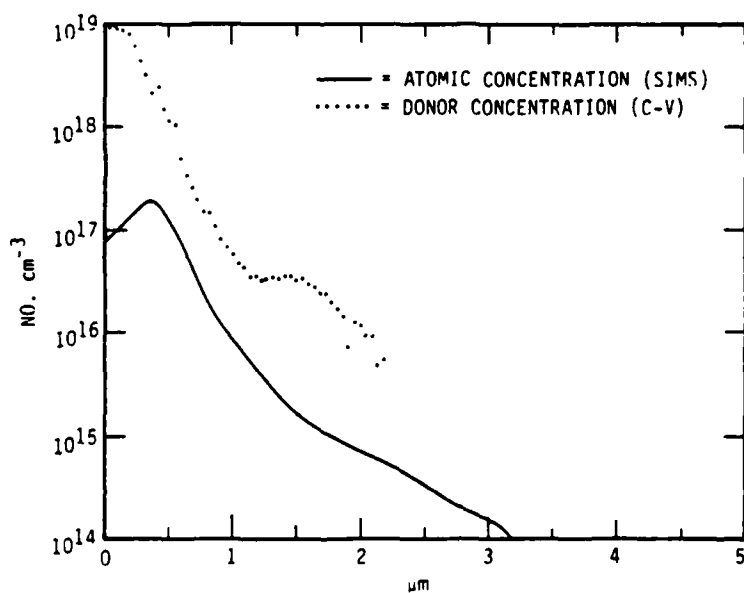


Figure 2-20. Atomic and Donor Concentration Depth Profiles for Chlorine

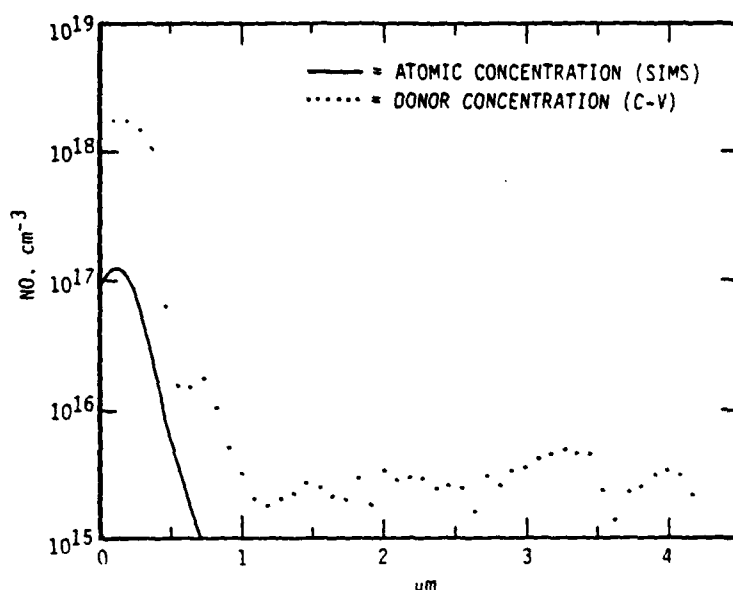


Figure 2-21. Atomic and Donor Concentration Depth Profiles for Indium

of channeling. A similar effect is seen in silicon.¹ The "Z1" channeling probability is dependent on the radial electron density which varies somewhat cyclicly with mass.^{2,3} It appears that the same dependence holds in HgCdTe. The absolute values of Z1 will of course be different due to different channel size, bond strength and atoms present in the lattice.

The next point of interest is a comparison of level and peak position in the "random" portion of the profile. In Si and GaAs the ratio of the damage level to ion concentration goes up with increased mass. This is due to heavier ions carrying less of the recoil. The lattice absorbs more of this energy propagating a higher damage level. This effect is not seen in the HgCdTe samples. The ratio of damage to ions was 10 ± 1 for all ions except H and Cl. It is very likely that the reason for this is a "self-annealing" effect in the crystal. This effect has been seen on a microscopic scale by T. James⁴ in a comparison of implants performed at 300K and 77K. The exception of H, where the peak damage level is a factor of 10 below the ion concentration is to be expected due to its small mass and hence very little energy transferred to the lattice. Cl, on the other hand, shows a ratio of 100. This is substantially higher than the other ions and has been seen on previous samples.

The shape of the damage profile follows that of the random portion of the ion profile. In the case of Be the damage level actually drops below the ion level in the channeled region of the sample. The indication then is that nuclear stopping is responsible for induced damage levels and that the weaker electronic stopping forces do not distort the lattice enough to produce electrically active sites. The exceptions, again, are H and Cl. For H, the damage level is fairly constant and below the peak ion concentration. This can be explained by its small mass as mentioned earlier. In the case of Cl, however, there is a "shoulder" in the damage profile, beyond the random portion of the SIMS curve, which appears to follow the channeled ion distribution.

Conclusion

Several trends are apparent in this data. Damage-induced donor levels are indicated to be caused by nuclear rather than electronic stopping. The level of this damage may initially scale with increased mass, however a self-annealing effect is apparent, which results in all ions resulting in approximately the same damage level. Hydrogen is an exception due to its small mass. The behavior of Cl, which does not follow these trends, will require further investigation. Beyond the region of electrical damage and nuclear stopping the depth to which ions are channeled depends roughly on the radial electron distribution.

REFERENCES

1. J.S. Briggs and A.P. Pathak, J. Phys. C 7 1929 (1974).
2. A.P. Pathak, Nuclear Instrum. Methods 194 31-34 (1982).
3. I.M. Cheshire, G. Dearnaley and J.M. Poate, Proc. R. Soc. London A 311, 47-51 (1969).
4. T.W. James, C.Y. Huang, K.V. Vaidyanathan and H.L. Dunlap, presented at the U.S. Workshop on the Physics and Chemistry of HgCdTe, 1985 (to be published).

HUGHES

A HUGHES COMPANY

SANTA BARBARA RESEARCH CENTER

a subsidiary

Section 3

SURFACE STUDY AND OXIDATION CHEMISTRY

INTRODUCTION

Our investigation into the metal-HgCdTe interface continues with new data presented on the Cu-HgCdTe interface formation and a parallel study of the Cu-CdTe interface. These experiments were performed in UHV on clean cleaved samples and analyzed using PES. The role of the weak HgTe bonding in the lattice is emphasized in explaining the interface morphology for the Cu-HgCdTe and Cu-CdTe systems. The differences and similarities between the resultant morphologies of these metal-semiconductor interfaces and the Ag and Al metal-HgCdTe systems are also discussed, and the role of the Hg bonding in each is elucidated. Section 3.1 of this report contains a full discussion of these results.

The calculation of the band structure of CdTe along the [110] direction is reported in Section 3.2. The calculation was performed using the nonlocal pseudopotential of Chelikowsky and Cohen (see references, Section 2.2) and gives insight into the role of the actual final states involved in the normal emission process in influencing some of the features of the observed spectra. Much of the observed spectra agree with the approximation that the final states are free electron-like and therefore are parabolic, but certain peaks in the data appear to be influenced by a mixing of the parabolic bands that takes place in the crystal potential. The optical transition matrix elements for interband transitions were determined using the calculated wave functions of each band. These matrix elements are a major contribution in determining the intensity of spectral peaks and their polarization dependence agreed with the measured in experiment.

Section 3.3 contains new information extracted from angle-resolved photoemission (ARPES) experiments previously conducted. Attempts at the mapping of the electronic valence bands along the [100] and [111] directions from the data obtained in these experiments have been undertaken. Due to the experimental complexity resulting from off-normal emission in obtaining this data, the mapping of the bands in these cases is very difficult and nontrivial. Preliminary results indicate that the expected theoretical dispersion of these bands is found in these angle-resolved spectra. The application of these ARPES results into the investigation of the alloying effect in HgCdTe is also discussed.

SUMMARY

Cation Bonding and Electronic Structure in HgCdTe

At the beginning of this study, bonding of the cation in the lattice was imperfectly understood and, thus, the consequences of this were not fully appreciated. As we all know, HgCdTe crystallizes in the zincblende crystal structure which can be thought of as two interpenetrating face-centered cubic sublattices, one displaced from the other by $1/4 [111]$. Te occupies the sites of one of the sublattices, and Hg and Cd occupy sites on the other. The resulting bond configuration is one of tetrahedral symmetry where the outer valence electrons on the anion and cation hybridize to form sp^3 -hybrids to take place in covalent bonding. When one does theoretical calculations to determine the electronic valence bands, and hence derive many important parameters such as electronic transport and ease of dislocation formation, one must employ the crystal potential of the lattice. To do this calculation for most ternary alloy semiconductors, for example an alloy system in which there exists two different cations located on the cation sublattice a compositionally weighted average of the cation potentials is employed on the cation sublattice. This virtual crystal approximation (VCA) typically yields theoretical parameters that are in close agreement with experimentally determined values. As one can see, there are no provisions in this theoretical framework to account for any differences in the bonding between the anion and the two different nearest neighbor cations.

In HgCdTe, some of the behavior of the crystal suggests a very periodic lattice, whereas other observed phenomena was reflective of a more random lattice where the bonding between Hg and Te is distinguishable from that of CdTe. The extremely high electron mobilities in the conduction band minimum (CBM) is indicative of highly nonlocalized electronic wave functions characteristic of a periodic rather than random lattice. The ease of breaking the HgTe bond in the alloy resulting in the migration of Hg to the surface and its subsequent evaporation is suggestive of a different bonding for Hg and Cd in the alloy, and this difference should result in a different potential for Hg and Cd and hence be reflected in the electronic structure.

The techniques of PES and ARPES available to our research group were able to probe the valence electronic states that are both highly localized and nonlocalized, and therefore revealed several very interesting features

concerning the bonding in the lattice. When one observes the nonlocalized states at the VBM in the region of Γ in the Brillouin zone, which are comprised mostly of Te-p states, across the composition range from HgTe to CdTe, these states remain fixed in energy and hence are fairly insensitive to compositional changes. The CBM is predominately cation s-derived and since it also occurs at Γ , these very nonlocalized states sample an average potential of the entire lattice. Since the Hg6s² electrons are bound 1.4 eV deeper than the Cd5s², substituting Hg for Cd in CdTe will lower the conduction band and hence this CBM moves linearly with composition as one would expect in the approximation of a virtual crystal. This advantageous movement of the CBM while the VBM remains fixed is what gives HgCdTe its very attractive characteristic of bandgap tunability.

Insight into a very interesting feature of the bonding in the alloy is gained if one looks at the electronic valence band states located between 4 and 6 eV below the VBM. These states are located at the zone boundary and therefore are very localized and hence sensitive to Hg and Cd percentage. Two distinct peaks are seen that are fixed in energy but change in intensity as the composition changes. The deeper bound peak can be attributed to Hg s-states at 5.4 eV and the lesser bound peak at 4.6 eV is attributed to Cd s-states. This represents a deviation from virtual crystal behavior because one would expect these states to change linearly with composition in the framework of the VCA. This selective breakdown of the VCA reveals that the HgTe bonds are different from the CdTe in the lattice, and this unusual behavior indicates that a more sophisticated picture of the bonding in this alloy must be found. One must take into account the difference in the cation potentials in evaluating the alloy electronic structure. The coherent potential approximation (CPA)³ takes this into account, and calculations of density of states using the CPA give much better agreement to experimental data than using the VCA.

The selective breakdown of the VCA also gives insight into many of the observed mechanical deficiencies of HgCdTe, as well as the point defect equilibria which gives rise to acceptor-type behavior. The deeper bond Hg s-valence bonding states are retained nearer to the Hg nucleus than that of the lighter Cd, and hence the Hg does not produce as strong of a covalent bond to Te than does Cd. This results in a HgTe bond that is as much as 30% weaker

than the CdTe in the HgCdTe alloy. There is no other semiconductor with such a large difference in the pseudobinary constituent bonds. Further information is gathered from the UPS spectra of different alloy compositions by looking at the behavior of the Cd4d and Hg5d core levels. A key finding in our work was that upon adding Hg to CdTe, the Cd4d becomes more deeply bound, whereas the addition of Cd to HgTe decreases the Hg5d binding energy. Therefore the HgTe bond weakens further and the CdTe strengthens in the alloy as compared to their energy in the respective binaries. Consequently, adding Cd to HgTe exacerbates the instability of the alloy, and can give rise to greater densities of point defect such as Hg vacancies, and the breaking of the HgTe can result in Hg out-diffusion from the lattice. This has severe ramifications into the structural integrity of the alloy, and the history of the sample during growth and annealing is very critical. In all of our studies of HgCdTe as listed in Section 4.1, this bonding nature of the alloy is manifested in studies of the interfaces, surfaces, and bulk properties of HgCdTe.

Experimental determination of the electronic valence band structure along the major symmetry directions [110], [100], and [111] using ARPES has also been performed under this contract. Accurate knowledge of the band structure of a material enables many materials properties to be estimated. Properties ranging from effective mass in the conduction band to vacancy formation energies may be estimated from a detailed picture of the bands. Accurate knowledge of the electronic bands is also essential when deriving the transport properties of superlattices, which are currently of great interest in HgCdTe technology. The theoretical properties calculated for these materials are not as precise without this kind of knowledge derived from our study.

In the ARPES studies performed on this contract, the acquired spectral data points were mapped along the primary directions in reciprocal space, and the experimental points were compared to theoretical calculations.⁴ The initial state bands are determined by assuming a free electron final state in the conduction band. This first order approximation holds for some of the bands, or rather, yields initial state bands that agree well with the theoretically predicted results, but for others the assumption of a free electron final state and folding back into the first zone of the primary reciprocal lattice vector (e.g. $G = 4\pi/a[110]$ in the case of [110] normal emission) yield inaccurate initial state values. In Section 2.2 of this report, a more

sophisticated method of determining the initial states is presented. Nonlocal pseudopotential calculations of the conduction bands up to 30 eV above VBM indicate a mixing of the parabolic bands in the crystal potential and the incorporation of other reciprocal lattice vectors in the electron scattering provide for a more accurate initial state-band determination. Another utility of our ARPES work is that it allows one to determine more subtle features in the valence band such as alloy broadening. Closely related is the ability to determine the effect of Hg loss by experimentally examining ARPES as a function of Hg loss. The details of this experiment are given in Section 2.3 of this report.

Native Oxidation of HgCdTe

One of the primary problems one must solve to increase the reliability, optimize the processing technology, and improve device yield is to improve the passivation of the HgCdTe surface. The oxidation of this ternary alloy system is very complex and the resultant equilibrium oxides are determined by the intensive thermodynamic state variables that the system is subjected to during growth of the oxide. There are many equilibrium or metastable oxides that may be theoretically produced, but most are subject to decomposition even at relatively low temperatures, or upon the deposition of other passivation layers. This unreliability in the structural and hence dielectric properties cast doubt as to the benefit of producing native oxides at all on HgCdTe surfaces. The very low sticking coefficient for oxygen on HgCdTe also renders this a very difficult process to achieve. We suggested very early on in this contract that it might be beneficial to minimize the native oxides of HgCdTe and deposit a layer of an external oxide, e.g. SiO_2 , as gently as possible to passify the surface.

To understand more fundamentally the kinetics of oxide formation and the initial stages of uptake of oxygen on the surface of HgCdTe, PES was employed as a sensitive surface probe to study this interaction. Because of the difference in the cation bonding in the lattice, a sensitive study of the oxygen chemistry with HgCdTe should also reveal a difference in the kinetics and activity of the system as a function of composition. There were two primary areas of research in this study, the identity and character of the oxygen species responsible (e.g. O, O_2 , etc), and the rate of oxygen uptake on the

surface. Initial experiments indicated that molecular oxygen that was unexcited did not stick appreciably to the HgCdTe surface over a period of many hours. When the ion gauge filament (electron-filament) was turned on in line of sight of the sample oxygen uptake was stimulated. The exact nature of the excited oxygen species is not known, but it most likely appears to be molecular oxygen which may be vibrationally excited.

The complex oxygen chemistry of HgCdTe tends to support the bonding theories discussed in the previous section. It was found that the rate of oxide production of $\text{Hg}_{0.69}\text{Cd}_{0.31}\text{Te}$ was 69% of that for HgTe, therefore the rate of growth scales with the number of HgTe bonds in the alloy. This oxide growth is accompanied by a release of Hg from the lattice and an incorporation of the Cd in the oxide. The free Te to oxidizes once the bond to the Hg has been broken. The oxidation rate of CdTe was faster than that of the alloy, indicating a lowering of the activity of the CdTe sites in the alloy. One of the major conclusions than can be drawn from our oxidation studies is that even the first one or two atomic layers alter the HgCdTe composition at the surface, which could have deleterious consequences for any devices passivated with native oxide.

Mechanical Defects

Observations into the change of electronic behavior of HgCdTe upon mechanical stress and the question of mechanical stability of the lattice prompted our TEM studies into the mechanical defect structure of HgCdTe. Also desirable in our studies was information into the heterojunction widths between the substrate CdTe and HgCdTe LPE layers. Three primary studies were conducted on HgCdTe under this contract. The determination of the defects in the lattice of SSR p-type HgCdTe giving rise to etch pits produced by the Polisar⁵ etch-2 was the first study. The defect structure at a cleaved HgCdTe surface was also investigated. The desire to observe at LPE layers in cross section prompted another study into the difference of ion milling induced defects in HgCdTe and CdTe.

A traditional method of quickly determining the quality of a single crystal of known orientation is to etch the surface with a suitable defect etchant to produce etch pits on the surface. The concentration and distribution of these etch pits yields valuable information into the defect structure

of the lattice. Because of the ambiguity that may exist as to the origin of the defects giving rise to the etch pits, we undertook a study using TEM to identify the defects. In a predominate number of etch pits, Te precipitates were found to most likely have given rise to the etch pit. It is important to emphasize that the material study was SSR p-type HgCdTe, and the [111] A-face (HgCd) give rise to the etch pits upon etching with the Polisar⁵ etch-2. Near the edge of the ingot the etch pits lie in an array strongly reminiscent of the dendritic arms in the original cast ingot. These observations suggest that the SSR ingot is strongly influenced by the casting stage.

Another study of great importance was to understand the defect structure induced on the [110] face upon cleaving because this is the surface studied in PES and hence is of great theoretical importance. The face was found to be rough on an optical scale, and the fracture surface exhibited numerous steps and the fracture appeared to be brittle in some regions. Upon examining the surface with TEM, it was found that at the portion of the surface that a step appeared, a high density of dislocations had been nucleated at the step. The crack appeared to proceed slightly off the ideal cleave face, arrest with a corresponding nucleation of many dislocations, and then proceed. Thus, the cleavage face was found to be much more defective than the bulk. This might explain why the surface often converts to n-type upon cleaving, and future experiments looking into this are planned at Stanford.

Another important mechanical feature of HgCdTe is the abruptness of the transition region between the CdTe substrate and the LPE HgCdTe. These interfaces are difficult to image with the TEM because it is difficult to make a TEM sample without introducing artifacts. We employed ion milling to thin the material, and although we introduced many artifacts, the distribution of the ion milling induced defects in the CdTe/HgCdTe heterojunction was very surprising. Detailed analysis of the defects in the HgCdTe and CdTe revealed the probable reason for a 2 to 3 order of magnitude higher defect density in the CdTe; the stacking fault widths in the CdTe were much wider than in HgCdTe. This lends support to the theoretical predictions⁶ of a weak HgTe bond and an increase in the metallicity of this bond because the stacking fault should be narrower for less directional or rigid bonds and the number of Hg vacancies greater than a weaker HgTe bond. Both of these characteristics should

increase the rate of recovery of the HgCdTe as compared to the CdTe, which was observed experimentally.

Metal Overlayers

A relatively neglected interface up to this point in HgCdTe is that of the metal/HgCdTe system. Most processors of HgCdTe devices tend not to worry about metal contacts because they are for the most part ohmic contacts on n-type material. However, ohmic contacts on n as well as p-type materials are important. Similarly, the ability to produce reliable Schottky barriers is important for optimizing devices. But in light of the chemistry that occurs between HgCdTe and even two monolayers of oxygen, the stoichiometry of the HgCdTe in the vicinity of the surface may be drastically altered upon deposition of a reactive or even unreactive metallic species, which could produce deleterious effects on the electronic bands in the vicinity of the surface. We have studied the chemistry of the HgCdTe surface upon deposition of Al, Ag, and Cu. The Al is predicted thermodynamically to react strongly with the Te, and the Ag should not react, and Cu should fall between them in reactivity according to heats of formation data. In addition to the chemistry of these surfaces, pinning of the fermi level was also monitored as a function of deposition.

There are several interesting observations that we have made into the characteristics of each interface. We have found that the reactive Al case drastically depletes the surface of Hg as the first few monolayers are deposited. This is not the case for Ag or Cu. In the Ag case, the Ag is seen to replace the Hg in the top approximate 1000Å, it therefore diffuses very deeply into the bulk. For the Al/HgCdTe interface, the first 3 to 5 monolayers are incorporated into an AlTe reacted layer, with further Al deposition being incorporated as metallic Al. The deposition of Cu onto HgCdTe and CdTe reveals an enhanced Te and Cd intermixing into the Cu for HgCdTe compared to CdTe. These systems were discussed in Section 2.1 of this report. The fermi level is also pinned for each case. For Ag on HgCdTe the bands bend up 0.05 to 0.10 eV which indicates a lower binding energy for this case. In the Al on HgCdTe case, all core level and VB features shift 0.5 ± 0.05 eV to higher binding energy, i.e. the fermi level moves upward from the VBM energy. The Cu

case is still being investigated. We have shown unique behavior in HgCdTe metal contacts, much more remains to be done to elucidate these findings.

Cd Loss in BrM Etched Surfaces

In extending our studies to HgCdTe surfaces of practical interest, we have observed with PES profound Cd loss upon etching these surfaces with BrM. Losses between 5% and 20% have routinely been observed. These technologically important surfaces (e.g. the [111] face for LPE and MBE) must be cleaned before the initial processing steps can be performed to build up the device structure. That we see Cd loss upon etching HgCdTe with BrM is not too surprising in light of the etching rate experiments performed by Talasek,⁷ but the magnitude of this loss suggests that the material's crystalline structure and electrical properties could be greatly affected. The significance of our studies outlined in the next section in studying cation loss, and its effect on the electronic structure, is underlined by this finding on practical surfaces.

Electron Beam Induced Desorption

Because HgCdTe is seen to lose the cation species when subjected to conditions identical to those seen during processing, it is very important to study the effect of this loss of stoichiometry on the electronic structure of the alloy. Such studies are also of fundamental importance. We have mentioned many experiments in this report that result in a loss of Hg from the lattice. Depositing metals on the surface or reacting the surface with excited oxygen cause the surface region of HgCdTe to be depleted of Hg to varying depths. Etching free HgCdTe surfaces with bromine methanol (BrM) results in profound Cd loss from the surface region. A very powerful study may be conducted if one of the cations can be removed in a well-controlled manner and the resulting surface probed using ARPES to reveal the subtle effects of cation loss on the electronic structure of the altered HgCdTe.

Because we can remove Hg from the lattice by impinging the surface of HgCdTe with an electron beam, and the electron beam parameters can be controlled precisely, we are able to surgically remove Hg and study the resultant electronic structure. We can also monitor the crystallinity of the lattice with low energy electron diffraction (LEED) to give us critical information as

to the structural nature of the lattice after profound cation loss. At the initial stage of Hg loss (approximately 3%), the surface structural crystallinity and electronic structure are intact, and the surface becomes degenerate p-type. These parameters remain intact up to about 9% loss, but at greater Hg loss the surface crystal and electronic structure gradually lose the crystalline character of a covalently bonded lattice. The selection rules dictated by a crystalline solid are lost and the valence band loses its dispersion. These observations reveal that the attractive electronic properties of HgCdTe can be drastically altered upon processing the alloy when making devices.

Implications Into Future Research

HgCdTe is of extreme importance because its bandgap is "tuned" by composition to any value from 0 to 1.5 eV. This has given it great potential as an infrared (IR) detector. However, great difficulties have arisen in achieving the potential of HgCdTe because of its "structural" weakness which make it difficult to process and passivate devices or device arrays. A key contribution from this contract was establishing of a one to one relationship between the bandgap tunability and the structural weakness in HgCdTe. As was established under the contract both properties are due to the peculiar nature states of Hg. In order to fully exploit the results of this contract, it is critical that the key role of Hg be understood. Doing so, several avenues of work are clearly called for. This will be discussed below.

One avenue is to explore materials which have the bandgap "tunability" of HgCdTe but which may have strong lattices. Since the band tunability is uniquely due to Hg, this must be retained in the lattice. An important result from this contract was the finding that $\text{Hg}_{1-x}\text{Zn}_x\text{Te}$ should have more mechanical strength than HgCdTe while retaining the E_g tunability. It is very important that this be followed up by work on $\text{Hg}_{1-x}\text{Zn}_x\text{Te}$. A contract is being planned by NASA and the Army to get such work underway. However, much more support is necessary to fully exploit this opportunity which was revealed by the present contract. One area of importance not covered by the NASA-Army contract is work on surface passivation and metallization.

There have been informal suggestions that alloying HgCdTe with up to about 10% MnTe might give material with the same IR properties but more strength than HgCdTe. For completeness, it would be important to pursue such

possibilities. However, this seems less promising than $\text{Hg}_{1-x}\text{Zn}_x\text{Te}$. It appears increasingly clear that exploration and exploitation of CdTe-HgTe superlattices will be a very important future IR project; however, ZnTe-HgTe superlattices should not be overlooked from the reasons given above. Here questions of the stability of the HgTe:CdTe (HgTe:ZnTe) interfaces are very important. The present contract gives a good background into these. The experimental and theoretical approaches established here should be exploited for future work on these critical interfaces. This contract has established that because of the Hg "instability" in HgCdTe, interfaces on this or other Hg containing materials (such as $\text{Hg}_{1-x}\text{Zn}_x\text{Te}$) provide very unique problems. Three types of interfaces are important.

- semiconductor:insulator
- semiconductor:metal
- semiconductor:semiconductor

The superlattices referred to in the preceding paragraph are one example of the semiconductor:semiconductor interface. Much effort has been spent to date in studying a very limited number of these interfaces. However, this past work has principally been empirical where a very specific problem has been attached in the context of a given application. It would be much more efficient to attack these problems as well in a very generic way. To do this, a number of avenues opened by the present contract should be exploited. Within this context we will now make more specific suggestions.

The Hg instability is a key problem with HgCdTe (or other long wavelengths, Hg containing IR detectors). We have shown in this contract that this is particularly critical at the interfaces listed above. We have also established that Hg loss can be produced at surfaces in a very controlled manner by an electron beam. Studies of the effects of such loss should be done on a wide range of parameters important to device operation.

This contract has studied in some detail the Cd loss produced on standard (bromine-methanol) preparation of HgCdTe surfaces. The Hg loss would be expected to effect properties in a similar way to this loss; however, detailed studies of this loss, its cause and effects, are also of importance.

The disturbances and loss of the Hg in HgCdTe lattice caused by vapor deposition of metals has been established and studies in this report. The IR

detector technology has advanced to the point where such phenomena may effect device operation. Thus, these phenomena should be studied in a systematic fashion.

It has also been established that oxidation disturbs the HgCdTe surface. This has strong implications into passivation; as does the realization that deposition of a foreign oxide can disturb the surface. It is critical that this be studied in a systematic way in order to reduce the ultimate costs in developing IR detector arrays.

These are but a few of the major technological problems presently facing II-VI semiconductor IR technology. The successful exploitation of these exotic II-VI semiconductor alloys is dependent on many of these problems being solved. The fundamental understanding into the bonding of HgCdTe in this present contract has provided an impetus to study these new ternary alloy systems, and the future successful manufacture of devices made from these semiconductors is dependent on the increased understanding into the peculiar nature of the bonding in these lattices.

REFERENCES

1. H. M. Nitz, O. Ganschow, U. Kaiser, L. Wiedmann, and A. Benninghoven, Surf. Sci. 104, 365 (1982).
2. A. Ebina and T. Takahasi, J. Cryst. Growth 59, 51 (1982).
3. A.-B. chen, and A. Sher, J. Vac. Sci. Technol. 21, 138 (1982).
4. J. R. Chelikowsky and M. L. Cohen, Phys. Rev, B 14, 556 (1976).
5. E. L. Polisar, N. M. Boinikh, G. V. Indenbaum, A. V. Vanyukov, and V. P. Schastlivii, Izv. Vyssh. Uchebn Zaved Fiz. 6, 81 (1968).
6. W. A. Harrison, J. Vac. Sci. Technol A 1, 1672 (1983).
7. R. T. Talasek, and A. J. Syllaios, J. Electrochem. Soc. 132(3), 656 (1985).

3.1 ROLE OF Hg BONDING IN METAL/ $\text{Hg}_{1-x}\text{Cd}_x\text{Te}$ INTERFACE FORMATION

Abstract

We discuss the role of the weak bonding of Hg in the $\text{Hg}_{1-x}\text{Cd}_x\text{Te}$ lattice upon interface morphology when metal is deposited on the surface. The Ag/ $\text{Hg}_{1-x}\text{Cd}_x\text{Te}$, Cu/ $\text{Hg}_{1-x}\text{Cd}_x\text{Te}$, Al/ $\text{Hg}_{1-x}\text{Cd}_x\text{Te}$, and Cu/CdTe interfaces are studied in ultra-high vacuum with X-ray and ultraviolet photoemission and with LEED. The three metals are found to yield distinctly different interface morphologies. For Ag/ $\text{Hg}_{1-x}\text{Cd}_x\text{Te}$, the Hg instability results in vacancy diffusion of Ag 10^2 - 10^3 Å into the semiconductor. For Cu overlayers, the instability greatly enhances Te and Cd intermixing into the Cu for $\text{Hg}_{1-x}\text{Cd}_x\text{Te}$ compared to CdTe. The more reactive Al overlayers deplete the weakly bound Hg from the $\text{Hg}_{1-x}\text{Cd}_x\text{Te}$ surface. We compare the metal/ $\text{Hg}_{1-x}\text{Cd}_x\text{Te}$ interfaces with the corresponding metal/CdTe and metal/GaAs interfaces. For the three overlayer metals on $\text{Hg}_{1-x}\text{Cd}_x\text{Te}$ the instability of the Hg bond results in interfaces with a much greater degree of intermixing than for the corresponding metal/binary semiconductor interfaces.

Introduction

$\text{Hg}_{1-x}\text{Cd}_x\text{Te}$ is a semiconductor alloy with a bandgap spanning the range 0 to 1.5 eV as the composition is varied from $x = 0$ to $x = 1$. As such it is an important candidate for IR photodetection. Intimately related to this bandgap tunability is a marked instability in the HgTe bond.¹ The weakness of this bond is reflected in the much lower heat of formation ΔH_f for HgTe than for CdTe: $\Delta H_f(\text{HgTe}) = -7.6$ kcal/mole, while $\Delta H_f(\text{CdTe}) = -24.1$ kcal/mole.² Further, there is theoretical³ as well as experimental¹ evidence that the HgTe bond, which is already weak in HgTe, is further destabilized in $\text{Hg}_{1-x}\text{Cd}_x\text{Te}$ by the presence of the Cd. This instability plays a critical role in electronic and mechanical properties of the material, both for the bulk and for surfaces and interfaces.¹

Both for applications to IR photodetection and to further the understanding of Schottky barrier formation in general, it is of interest to study the interface properties of the metal/ $\text{Hg}_{1-x}\text{Cd}_x\text{Te}$ junction. As might be expected, the weakness of the HgTe bond plays a crucial role in determining the nature (morphology and band bending) of the interface. In this paper we explore the behavior of the metal/ $\text{Hg}_{1-x}\text{Cd}_x\text{Te}$ interface morphology through photoemission

and LEED studies of interfaces of $\text{Hg}_{1-x}\text{Cd}_x\text{Te}$ with three metals of increasing reactivity: Ag, Cu and Al; the Cu/CdTe interface was also studied. For all three metals, the HgTe bond instability is found to result in highly nonabrupt interfaces, with marked depletion of Hg from the semiconductor near-surface for the more-reactive overlayers, and intermixing of the semiconductor and overlayer for the less-reactive cases.

Table 3-1 shows the heats of formation ΔH_f of Te of the noble metals and of Al. Also shown are the heats of alloying $\Delta H_{\text{sol}}(\text{C};\text{M})$ of the cations (C) Cd and Hg at infinite dilution in the overlayer metals (M), calculated using the semiempirical model of Miedema.^{4,5} Based on their small heats of formation with Te, the noble metals would be expected to form nonreactive interfaces with $\text{Hg}_{1-x}\text{Cd}_x\text{Te}$, while Al, with its large $\Delta H_f(\text{Al}_2\text{Te}_3)$, should in contrast be strongly reactive with $\text{Hg}_{1-x}\text{Cd}_x\text{Te}$. In accordance with these considerations, there is clear evidence of strong overlayer-Te formation for Al overlayers but not for Au,⁶ Ag, or Cu overlayers. However, although the noble metals have comparable heats of Te formation, Ag/ $\text{Hg}_{1-x}\text{Cd}_x\text{Te}$ and Cu/ $\text{Hg}_{1-x}\text{Cd}_x\text{Te}$ prove to have dissimilar morphologies, while Au/ $\text{Hg}_{1-x}\text{Cd}_x\text{Te}$, for which we refer to the results of Davis et al.,⁶ presents a porphology distinct from both the Ag and Cu interfaces. An understanding of these differences requires consideration of the heats of solution ΔH_{sol} , as well as ΔH_f .⁷ Finally, the large heat of Te formation for Al gives the interface of Al with $\text{Hg}_{1-x}\text{Cd}_x\text{Te}$ a morphology which differs from the interfaces with the noble metals.

Table 3-1. Heats of Te Formation ΔH_f , and Heats of Solution $\Delta H_{\text{sol}}(\text{C};\text{M})$ of Cation C in Metal M in the Solid Phase, for Various Metals on $\text{Hg}_{1-x}\text{Cd}_x\text{Te}$.

Metal (M)	Telluride (Te)	ΔH_f^* (kcal/mole)	$\Delta H_{\text{sol}}(\text{Cd};\text{M})^{**}$ (kcal/mole)	$\Delta H_{\text{sol}}(\text{Hg};\text{M})^{**}$ (kcal/mole)
Cd	CdTe	-24.1		
Hg	HgTe	-7.6		
Ag	Ag_2Te	-8.6	-3.4	-2.1
Cu	Cu_2Te	-10.0	-1.7	+0.3
Au	AuTe_2	-4.5	-12.2	-6.4
Al	Al_2Te_3	-76.2	+3.4	+4.1

*From Ref. 2.
 **Calculated from Miedema's semiempirical model (Refs. 4 and 5).

Experimental

Single-crystal bars of p-type $\text{Hg}_{1-x}\text{Cd}_x\text{Te}$ ($x = 0.23$ for Ag and Al overlayers, $x = 0.25$ for Cu) and n-CdTe (In-doped to $1 \times 10^{17}/\text{cm}^2$) with cross-sectional areas of $5\text{--}5 \text{ mm}^2$ were transferred into a previously-baked vacuum chamber and then cleaved in ultra-high vacuum (base pressure 6×10^{-11} torr) to reveal a [110] face. For the cleaved $\text{Hg}_{1-x}\text{Cd}_x\text{Te}$ surfaces the Fermi level E_F was located near the conduction band minimum (CBM) making the surfaces n-type, as is often observed.⁸ For CdTe, E_F for the clean cleaved surface was located 0.3 eV below the CBM. (The bulk bandgap is 0.20 eV for $x = 0.23$, 0.22 eV for $x = 0.25$, and 1.49 eV for CdTe.) Sequential depositions of metal were evaporated from a tungsten filament onto the room temperature surface, which was studied at each stage by X-ray and ultraviolet photoelectron spectroscopy (XPS and UPS) using respectively a Mg K α X-ray source ($h\nu = 1253.6$ eV) and a helium lamp (He I and He II, $h\nu = 21.2$ and 40.8 eV). The photoelectrons were analyzed with a double-pass cylindrical-mirror analyzer (CMA). All interfaces except for Al/ $\text{Hg}_{1-x}\text{Cd}_x\text{Te}$ were also characterized by LEED using electron energies less than 65 eV and beam currents less than 1 μA . We observed no electron-beam-induced surface disruption for $\text{Hg}_{1-x}\text{Cd}_x\text{Te}$ or CdTe, in contrast to the disruption reported for CdTe in Ref. 9. The amount of metal deposited is given in units of a monolayer, ML, which we define to be the surface density of atoms on the $\text{Hg}_{1-x}\text{Cd}_x\text{Te}$ [110] face: for $x = 0.23$, 1 ML = 6.76×10^{14} atoms/ cm^2 which corresponds to 1.15Å of metallic Ag, 0.80Å of Cu, and 1.12Å of Al. The variation of surface atomic density with x -value over the entire composition range is 1%, which is negligible for our purposes.

Results

In subsections A to C below, the three metal/ $\text{Hg}_{1-x}\text{Cd}_x\text{Te}$ interfaces are compared with the respective metal/CdTe and metal/GaAs interfaces with emphasis on the role that the Hg bonding plays for $\text{Hg}_{1-x}\text{Cd}_x\text{Te}$. Full discussions of the Ag/ $\text{Hg}_{1-x}\text{Cd}_x\text{Te}$ ^{10,11} and Al/ $\text{Hg}_{1-x}\text{Cd}_x\text{Te}$ ¹¹ interfaces have been published. The latter interface has been investigated previously by Daniels et al.¹² and Davis et al.¹³ We present here a brief preliminary discussion of Cu/ $\text{Hg}_{1-x}\text{Cd}_x\text{Te}$ and Cu/CdTe; a more complete analysis will be presented elsewhere.¹⁴

Before presenting the results, we give a brief overview. The differences in interface morphology mentioned in the introduction are reflected in the He I valence band spectra in Figure 3-1, which shows spectra for the clean $\text{Hg}_{1-x}\text{Cd}_x\text{Te}$ surface as well as for the surface covered by 5 ML of each overlayer metal. The Ag4d intensity for 5 ML Ag/ $\text{Hg}_{1-x}\text{Cd}_x\text{Te}$ is much less than the Cu3d intensity for an equal coverage of Cu/ $\text{Hg}_{1-x}\text{Cd}_x\text{Te}$. The Al/ $\text{Hg}_{1-x}\text{Cd}_x\text{Te}$ spectrum is striking for the almost complete attenuation of the Hg5d level at the relatively low 5 ML coverage.

Ag overlayers

Because at $h\nu = 21.2$ eV the Ag4d, Cd4d and Hg5d states have similar cross sections,¹⁵ the comparatively low intensity of the Ag4d in Figure 3-1 implies that either the Ag is not sticking to the surface or it diffuses well into the semiconductor. A detailed analysis¹⁰ of the XPS core levels shows that the Ag diffuses 10^2 - 10^3 Å into the bulk of the semiconductor. Only after on the order of 100 ML Ag has been deposited does the surface attain a metallic character, with the valence band spectrum showing an occupied density of states up to the Fermi level. While the Te and Cd concentrations in the near-surface remain essentially constant up to 100 ML Ag deposition, the Hg concentration decreases by 3% with each ML of Ag evaporated onto the surface.¹⁰ It is thus reasonable to infer that the Ag moves into the lattice by displacing Hg and then moving into the resulting vacancies, permitting the high solubility associated with vacancy diffusion. After Refs. 10 and 11 were published we repeated the study of Ag/ $\text{Hg}_{1-x}\text{Cd}_x\text{Te}$, this time including characterization of the surface order with LEED. In support of the Hg-replacement model of Ag diffusion, a LEED pattern showing the original 1×1 surface order is observed at coverages as high as 40 ML. At 100 ML the LEED pattern is gone, indicating that the surface is now covered with polycrystalline metallic Ag or that the concentration of Ag in the $\text{Hg}_{1-x}\text{Cd}_x\text{Te}$ surface at this coverage is high enough to disrupt the lattice order of the surface. No evidence is seen for significant chemical reaction between the overlayer and the semiconductor (although the data do not completely rule out the occurrence of such reaction).

The importance of the presence of easily removed Hg in formation of the Ag/ $\text{Hg}_{1-x}\text{Cd}_x\text{Te}$ interface is verified by a comparison with Ag/CdTe from Ref. 9. With no weakly bound cations which Ag can replace in the lattice, Ag

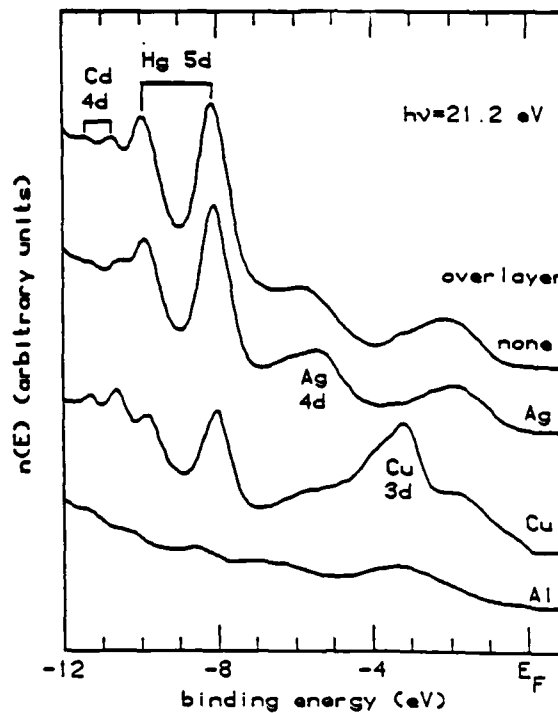


Figure 3-1. Valence Band Spectra at $h\nu = 21.2$ eV of the Clean $\text{Hg}_{1-x}\text{Cd}_x\text{Te}$ Surface as Well as for the Surface Covered by 5 ML of Each Overlayer Metal. The $\text{Cu}/\text{Hg}_{1-x}\text{Cd}_x\text{Te}$ spectrum is for the composition $x = 0.25$; the other three spectra are for $x = 0.23$. A spectrum of clean $x = 0.25$ $\text{Hg}_{1-x}\text{Cd}_x\text{Te}$ is not shown as it is very similar to the clean $x = 0.23$ spectrum.

should not diffuse into CdTe. In agreement with this reasoning, no movement of Ag into the semiconductor is observed for Ag/CdTe; this interface is essentially abrupt,⁹ in dramatic contrast to Ag/ $\text{Hg}_{1-x}\text{Cd}_x\text{Te}$ (a small Cd movement into the overlayer is observed in Ref. 9, but this may well be due to the anomalous instability of the surface observed during their LEED work). The behavior of Ag on CdTe closely parallels its behavior on the III-V's. Ag/ InP ¹⁶ and Ag/ GaAs ,¹⁷ for instance, have been shown to be nonintermixing, with the only important deviation from the "ideal" abrupt interface being Ag island formation instead of pure laminar growth.

Cu overlayers

Because of the similarities between Cu and Ag in metal-Te heats of formation, the two metals might naively be expected to form similar interfaces on $\text{Hg}_{1-x}\text{Cd}_x\text{Te}$. However, as was mentioned in the introduction, heats of alloying

will also play a role in determining interface reactivity (this point is discussed in greater detail in Section 4). Thus the valence band spectra for 5 ML of the two metals on $\text{Hg}_{1-x}\text{Cd}_x\text{Te}$ in Figure 3-1 differ in two ways: The Hg5d intensity decreases from the clean spectrum to the 5 ML coverage much more for Cu overlayers than for Ag; and while the Ag4d is barely visible due to diffusion of Ag into the bulk, the Cu3d intensity is comparable to that of the Cd4d and Hg5d levels. Since at $h\nu = 21.2$ eV all three subshells have similar photoionization cross sections,¹⁵ there can be no deep diffusion of Cu into the semiconductor as there is for Ag.

More details of the interface morphology can be obtained from the XPS core levels. Figure 3-2(a) shows as a function of Cu coverage the peak areas I of the semiconductor, normalized to the zero-coverage values I_0 . If the interface for Cu were abrupt and the metal film laminar, I/I_0 would fall exponentially with coverage, with a $1/e$ length of order 20 ML. Only for the Cd3d peak below 10 ML is such attenuation observed. Above 10 ML the attenuation of the Cd3d peak area slows so that at 100 ML coverage $I/I_0 \approx 40\%$. The deviation from exponential attenuation is even more marked for the Te3d peak area, which actually rises 5% by the 10 ML coverage, then levels off and falls slowly to $I/I_0 = 85\%$ at 100 ML coverage; there is virtually no further attenuation during the next 200 ML deposition. The attenuation of the core intensities is much too slow to be explainable by formation of Cu islands at the interface. The interface is thus highly nonabrupt, with significant intermixing of the surface up to coverages of several hundred ML. The Hg behaves very differently from the Cd or Te, with the Hg4f peak area decreasing to $I/I_0 = 80\%$ by 0.6 ML, and then attenuating exponentially until 10 ML with a $1/e$ length of 9 ML (11Å). The escape length in Cu (or a Cu-Cd-Te alloy) for electrons photoemitted with 1150 eV kinetic energy from the Hg4f subshell should be about 20Å.¹⁸ Thus the Hg4f attenuation, especially below 0.6 ML, is too fast to be an escape depth effect and must be due to depletion of Hg from the surface.

Some intermixing is observed for the Cu/CdTe interface as well, but to a much smaller degree than for Cu/ $\text{Hg}_{1-x}\text{Cd}_x\text{Te}$. Figure 3-2(b) shows the peak areas of the CdTe core levels as a function of Cu coverage, normalized as in Figure 3-2(a). Both Te and Cd core levels attenuate faster than for Cu/ $\text{Hg}_{1-x}\text{Cd}_x\text{Te}$. For Te3d, $I/I_0 = 20\%$ at 100 ML, with little attenuation

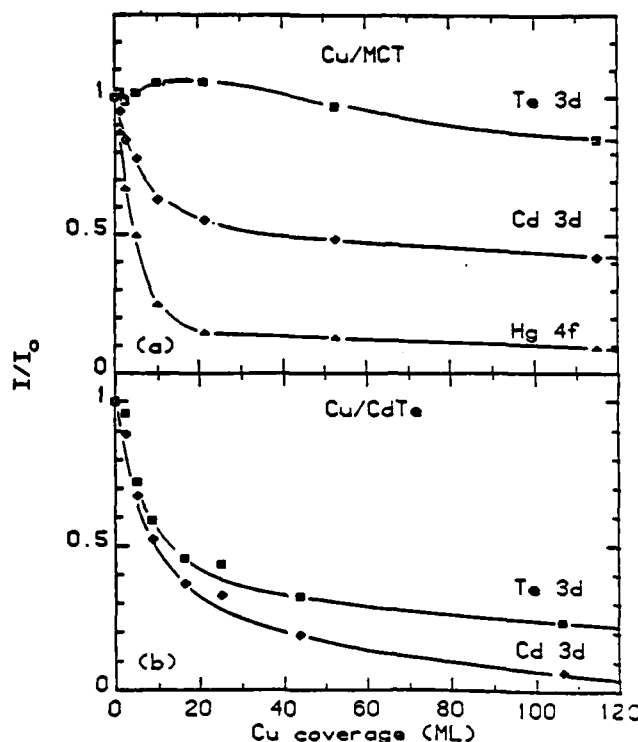


Figure 3-2(a). Attenuation of the XPS Peak Areas I of the $\text{Hg}_{1-x}\text{Cd}_x\text{Te}$ Core Levels With Increasing Cu Coverage. The peak areas are normalized to their zero-coverage values I_0 .

Figure 3-2(b). Attenuation of the Semiconductor Core Level Peak Areas as in (a), But for Cu/CdTe.

thereafter. The Cd3d attenuates exponentially with a 15 to 20 Å (19 to 25 ML) escape length at all coverages, with no signal observable beyond 100 ML. Thus, little or no Cd is intermixed from CdTe into the overlayer, while the concentration of Te intermixed into the overlayer for CdTe is about 1/4 of the intermixed Te concentration for $\text{Hg}_{1-x}\text{Cd}_x\text{Te}$. Formation of islands of Cu on the surface would also slow the attenuation of the Te3d level below that expected for a laminar interface, but then the Cd and Te intensities would be expected to attenuate at similar rates. Thus, while the landing of the Cu is not unlikely, the dependency of I/I_0 on the atom being examined unambiguously indicates intermixing of Te into the overlayer. The depletion of the weakly bonded Hg in $\text{Hg}_{1-x}\text{Cd}_x\text{Te}$ provides an excess of Te as well as presumably collapsing the lattice, thus causing substantially greater intermixing for $\text{Hg}_{1-x}\text{Cd}_x\text{Te}$ than for CdTe.

The similarities between metal/CdTe and metal/GaAs are even greater for Cu than for Ag. For Cu/GaAs,¹⁹ both Ga and As intermix with the overlayer, with the anion being the predominant intermixed species seen in the overlayer at high coverages. Indeed, the As3d peak area at $h\nu = 85$ eV attenuates sufficiently slowly that at 100 ML $I/I_0 = 30\%$, showing that the anion concentration in the Cu overlayer is comparable for GaAs and CdTe. The concentration of Ga in the Cu overlayer is much smaller than the concentration of As, with $I/I_0 = 2\%$ at 100 ML.

Al overlayers

The He I spectrum for $\text{Al}/\text{Hg}_{1-x}\text{Cd}_x\text{Te}$ in Figure 3-1 shows a very rapid Hg5d signal attenuation, with $I/I_0 = 5\%$ at 5 ML, implying a significant depletion of Hg from the surface. The attenuation of the semiconductor core level intensities with Al coverage is shown in Figure 3-3. The Cd3d attenuates at a rate consistent with attenuation through an abrupt Al overlayer, while the Te3d signal attenuates much more slowly, with $I/I_0 = 60\%$ at 40 ML. This slow attenuation of the Te3d intensity is consistent with the Te-rich surface-segregated layer reported by Davis et al.¹³ Verifying the expected reactivity of this interface, at coverages below 2 ML there is one Al2p peak corresponding to reacted Al (i.e. shifted to higher binding energy than for the metallic Al2p), while at higher coverages a metallic Al contribution arises at 0.9 ± 0.2 eV lower binding energy and becomes dominant as the interfacial reacted layer is covered up by unreacted Al. A detailed analysis of the interface is given in Ref. 11. It shows that as the first 2 to 3 ML of Al are deposited, Hg is depleted to 50% or less of its original concentration to a depth of 10 to 30Å into the semiconductor; there is little or no further Hg depletion at higher coverages. The Hg-depleted semiconductor surface is covered by a 3 to 5 ML thick AlTe reacted layer, which in turn is covered by metallic Al. A several ML thick Te-rich reacted layer is segregated to the surface of the metallic Al layer. A similar interface morphology is seen for the reactive In¹³ and Cr^{20,21} overlayers.

For $\text{Al}/\text{Hg}_{1-x}\text{Cd}_x\text{Te}$, a relatively sharp peak originating from the Te p-like states of the Te-rich layer floating on the metallic Al evolves in the UPS valence band at high coverages 3.2 eV below E_F .¹¹ Patterson and Williams²² show a very similar peak evolving at high coverages for Al/CdTe, which

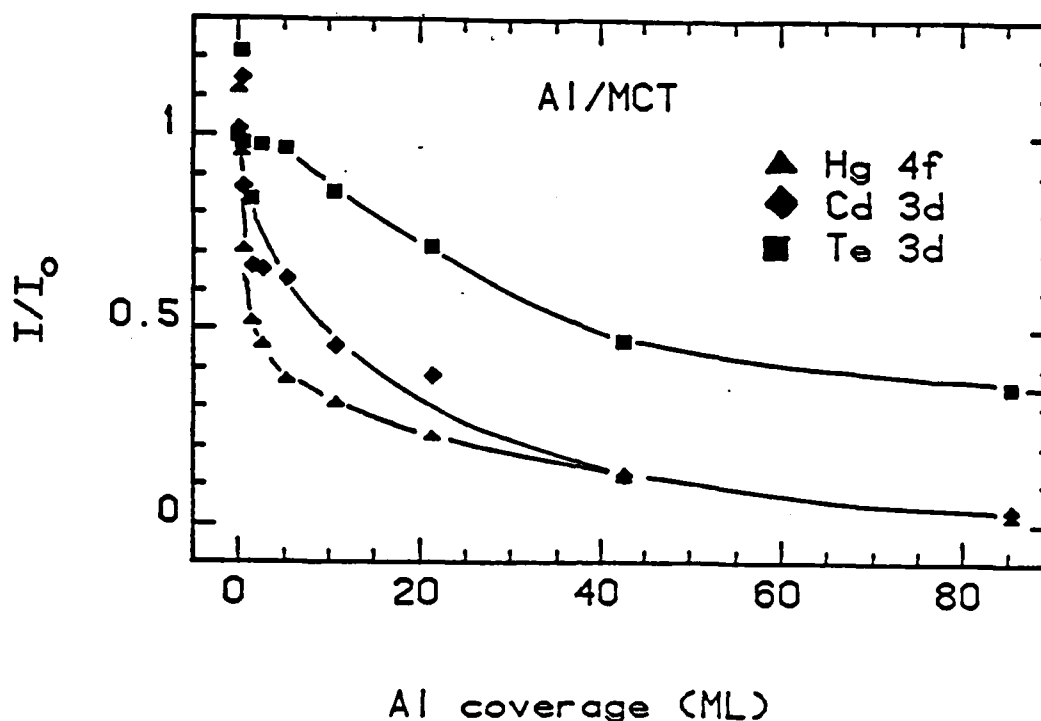


Figure 3-3. Attenuation of the XPS Peak Areas I of the $\text{Hg}_{1-x}\text{Cd}_x\text{Te}$ Core Levels With Increasing Al Coverage. The peak areas are normalized to their zero-coverage values I_0 .

suggests the presence of outdiffused Te in or on the Al for this interface as well. They also show evidence for the presence of metallic Cd dissociated from the CdTe, as manifested by the growth of a Cd4d peak at 0.6 eV lower binding energy than for Cd bound to Te. (Note that the formation of metallic Cd does not imply Cd intermixing with the overlayer. For Al/CdS,²³ for example, the dissociated metallic Cd is localized at the semiconductor surface.) No metallic Cd is seen for Al/ $\text{Hg}_{1-x}\text{Cd}_x\text{Te}$, suggesting that the presence of Hg is inhibiting formation of dissociated metallic Cd for the $\text{Hg}_{1-x}\text{Cd}_x\text{Te}$ interface. One contributing factor may be the enhancement of the CdTe bond strength in $\text{Hg}_{1-x}\text{Cd}_x\text{Te}$ compared to CdTe.¹ Probably more important is the nonstoichiometry of the first 10 to 30 Å of the semiconductor due to Hg depletion at low Al coverages. For $x = 0.23$ a depletion of half the Hg at the surface creates a large excess of Te, which is then available to help trap any Cd which might otherwise (as in Al/CdTe) have moved into the overlayer. This Te excess also provides Te for the AlTe interfacial reacted layer and for the Te-rich segregated surface layer.

For Al/GaAs,²⁴ a limited metal-cation exchange reaction occurs, with a small amount of released Ga present in the overlayer near the semiconductor surface. The reaction appears to be confined to within at most a few crystal layers, reflecting the large reactivity of the interface.²⁵ This decrease in interface width with increasing reactivity for GaAs appears to hold for $\text{Hg}_{1-x}\text{Cd}_x\text{Te}$ as well if the interface width is considered to be the width over which the composition changes from semiconductor to bulk metal. However, $\text{Hg}_{1-x}\text{Cd}_x\text{Te}$ (and probably CdTe) have a surface segregated anion layer which does not appear in GaAs. It has been observed²⁶ more generally that the ratio of outdiffused anion: outdiffused cation decreases with increasing overlayer reactivity for III-V's but not for II-VI's.

Discussion

For the three overlayer metals discussed in this paper, the trends in interface morphology for CdTe parallel those for GaAs. Ag forms a nonintermixed interface on both semiconductors, while for Cu there is a significant concentration of the anion in the overlayer up to several hundred ML coverage. This similarity between the two semiconductors for the noble metals also holds for Au. Au/GaAs²⁷ is at least as intermixing as Cu/GaAs: probed with $h\nu \approx 100$ eV (giving high surface sensitivity), $I/I_0 \approx 40$ to 50% for As3d and $\approx 10\%$ for Ga3d after 80 ML coverage. In comparison, for Au/CdTe²⁸ at 17 ML coverage, $I/I_0 \approx 60\%$ for the Te4d and $\approx 45\%$ for the Cd4d (probed with high surface sensitivity), making Au/CdTe somewhat more intermixed than Cu/CdTe. For both semiconductors the reactive overlayer Al forms more localized interfaces than for the noble metals, but the limiting of the interface width is much more pronounced for GaAs.

With the introduction of Hg into the lattice, the overlayers formed on $\text{Hg}_{1-x}\text{Cd}_x\text{Te}$ for the noble metals and Al differ significantly from the respective interfaces for CdTe and GaAs. In all cases the instability of Hg in the lattice serves to delocalize the interface to widths of a few tens of angstroms for Al (plus the surface segregated Te-rich layer), and hundreds of angstroms for the noble metals. The mechanism of the intermixing enhancement is different for the three overlayers studied here, as well as for Au.⁶ Furthermore, the Cd signal at high coverages is greater in Au/CdTe than in Cu/CdTe, while for $\text{Hg}_{1-x}\text{Cd}_x\text{Te}$ the situation is reversed, with a greater Cd

signal in $\text{Cu}/\text{Hg}_{1-x}\text{Cd}_x\text{Te}$ than in $\text{Au}/\text{Hg}_{1-x}\text{Cd}_x\text{Te}$. These differences can be understood qualitatively through consideration of the heats of alloying of the semiconductor cations in the overlayer metal. The heats of Te formation and cation-overlayer are shown in Table 3-1.

The relative abruptness of the Ag/CdTe interface is due to a lack of chemical reaction because of silver's low heat of Te formation $\Delta H_f(\text{Ag}_2\text{Te})$ and alloying $\Delta H_{\text{sol}}(\text{Cd};\text{Ag})$. For $\text{Hg}_{1-x}\text{Cd}_x\text{Te}$, the weakly bound Hg is driven out by the heat of condensation of the Ag on the $\text{Hg}_{1-x}\text{Cd}_x\text{Te}$ surface. This leads to formation of Hg vacancies through which the Ag can diffuse, driven by the concentration gradient in the chemical potential across the interface. Te formation and alloying can provide a barrier to this diffusion, but because $\Delta H_f(\text{Ag}_2\text{Te})$ and $\Delta H_{\text{sol}}(\text{Cd};\text{Ag})$ are small the barrier is low, permitting the observed motion of Ag 10^2 - 10^3\AA into the $\text{Hg}_{1-x}\text{Cd}_x\text{Te}$.

Au also has a small heat of Te formation, but its heat of alloying is much larger: $\Delta H_{\text{sol}}(\text{Cd};\text{Au}) \approx -14$ kcal/mole, which is four times the value of $\Delta H_{\text{sol}}(\text{Cd};\text{Ag})$. The large $\Delta H_{\text{sol}}(\text{Cd};\text{Au})$ is sufficient to disrupt the CdTe surface, pulling Cd into the overlayer. The presence of Te in the overlayer is probably also favored by alloying considerations, but this cannot be verified without information on $\Delta H_{\text{sol}}(\text{Te};\text{Au})$. In contrast, for Cu/CdTe little or no Cd is observed in the overlayer due to the small heat of alloying for Cu: $\Delta H_{\text{sol}}(\text{Cd};\text{Cu}) \approx 2$ kcal/mole. The slightly greater heat of Te formation for Cu than for Ag apparently is sufficient to pull Te into the overlayer for Cu/CdTe while leaving Ag/CdTe abrupt.

In the case of $\text{Hg}_{1-x}\text{Cd}_x\text{Te}$ interfaces with Cu and Au, the Hg instability alters the intermixing compared to CdTe. For $\text{Cu}/\text{Hg}_{1-x}\text{Cd}_x\text{Te}$, formation of Hg vacancies occurs to a greater degree than for the less reactive Ag/ $\text{Hg}_{1-x}\text{Cd}_x\text{Te}$. The resulting surface lattice collapse probably enables both Cd and Te to intermix with the Cu overlayer, and may also serve as a barrier to Cu indiffusion. The small heat of CuCd alloying now would presumably make it energetically favorable for the Cd to move to the surface of the Cu rather than mixing uniformly with the Cu. In this case the Cd core level intensity would be greater than for the same amount of Cd mixed uniformly into the overlayer. The observed strong Cd signal intensity for $\text{Cu}/\text{Hg}_{1-x}\text{Cd}_x\text{Te}$ is consistent with such Cd segregation to the surface (although this evidence is not conclusive). For $\text{Au}/\text{Hg}_{1-x}\text{Cd}_x\text{Te}$, on the other hand, the large heat of AuCd

alloying will tend to mix the Cd evenly into the overlayer, or even keep it localized near the $\text{Au/Hg}_{1-x}\text{Cd}_x\text{Te}$ interface. As can be seen from Table 3-1, the heat of AuHg alloying is nonnegligible, so that some Hg also might be seen in the overlayer, despite the large Hg vapor pressure. Davis et al.⁶ show that for 40 ML $\text{Au/Hg}_{1-x}\text{Cd}_x\text{Te}$, $I/I_0 \approx 20$ to 30% for Cd4d and $I/I_0 \approx 15\%$ for Hg5d (both probed with $h\nu = 70$ eV giving surface sensitivity on the order of 5 ML). We attribute the slow attenuation to mixing of the semiconductor cations into the Au.²⁹

Finally, for $\text{Al/Hg}_{1-x}\text{Cd}_x\text{Te}$ a strong AlTe reaction is observed. Consequently there is a Hg depletion of 50% or more in the first 10 to 30 Å of the semiconductor. This strong alteration of lattice stoichiometry, which does not have a direct parallel for the binary semiconductors CdTe and GaAs, must disrupt the lattice and provide an excess of Te. A 3 to 5 ML AlTe reacted layer on top of the Hg-depleted region is covered by metallic Al, with a segregated Te-rich layer floating on the surface. Although the Hg loss and resulting Te excess is much greater for Al overlayers than for Cu overlayers, the reactivity of Al with Te tends to "chemically trap"²⁵ the Te, making the presence of Te in or on the overlayer less than for Cu. The positive heat of alloying $\Delta H_{\text{sol}}(\text{Cd};\text{Al})$ of Cd in Al (Table 3-1), and the presence of the Te excess at the interface, keep Cd from entering the overlayer to any significant extent.

Conclusions

The instability of the Hg bond in $\text{Hg}_{1-x}\text{Cd}_x\text{Te}$ compared to the Cd bond plays a pivotal role in determining the morphology of metal/ $\text{Hg}_{1-x}\text{Cd}_x\text{Te}$ interfaces. Band bending, which was not emphasized in this paper, also is influenced by the Hg bonding. For $\text{Ag/Hg}_{1-x}\text{Cd}_x\text{Te}$, for instance, the indiffused Ag or possibly Hg vacancies themselves dope the semiconductor p-type at low coverages, bringing E_F closer to the valence band maximum.¹⁰ The weak Hg bonding causes metal/ $\text{Hg}_{1-x}\text{Cd}_x\text{Te}$ interfaces to show behavior qualitatively different from that of the binary II-VI and III-V semiconductors CdTe and GaAs.

REFERENCES

1. W. E. Spicer, J. A. Silberman, I. Lindau, A.-B. Chen, A. Sher, and J. A. Wilson, J. Vac. Sci. Technol. A 1 1735 (1983).
2. K. C. Mills, Thermodynamic Data for Inorganic Sulphides, Selenides and Tellurides (Butterworths, London, 1974).
3. A. Sher, A.-B. Chen, W. E. Spicer, and C. K. Shih, J. Vac. Sci. Technol. A 3, 105 (1985).
4. A. R. Miedema, P. F. de Chatel, and F. R. de Boer, Physica B 100, 1 (1980).
5. A. K. Niessen, F. R. de Boer, R. Boom, P. F. de Chatel, W. C. M. Mattens, and A. R. Miedema, CALPHAD 7, 51 (1983).
6. G. D. Davis, W. A. Beck, N. E. Byer, R. R. Daniels, and G. Margaritondo, J. Vac. Sci. Technol. A 2, 546 (1984).
7. The importance of the heat of alloying in interface formation has been discussed by, e.g., J. F. McGilp and I. T. McGovern, J. Vac. Sci. Technol. B 3, 1641 (1985).
8. J. A. Silberman, P. Morgen, I. Lindau, W. E. Spicer, and J. A. Wilson, J. Vac. Sci. Technol. 21, 154 (1982).
9. T. P. Humphreys, M. H. Patterson, and R. H. Williams, J. Vac. Sci. Technol. 17, 886 (1980).
10. D. J. Friedman, G. P. Carey, C. K. Shih, I. Lindau, W. E. Spicer, and J. A. Wilson, Appl. Phys. Lett. (in press).
11. D. J. Friedman, G. P. Carey, C. K. Shih, I. Lindau, W. E. Spicer and J. A. Wilson, J. Vac. Sci. Technol. (in press).
12. R. R. Daniels, G. Margaritondo, G. D. Davis, and N. E. Byer, Appl. Phys. Lett. 42, 50 (1983).
13. G. D. Davis, N. E. Byer, R. A. Riedel, and G. Margaritondo, J. Appl. Phys. 57, 1915 (1985).
14. D. J. Friedman, G. P. Carey, I. Lindau, W. E. Spicer and J. A. Wilson, unpublished.
15. J. J. Yeh and I. Lindau, At. Data Nucl. Data Tables 32, 1 (1985).
16. T. Kendelewicz, W. G. Petro, I. Lindau, and W. E. Spicer, Appl. Phys. Lett 44, 1066 (1984).
17. R. Ludeke, T.-C. Chiang, and T. Miller, J. Vac. Sci. Technol. B 1, 581 (1983).

18. I. Lindau and W. E. Spicer, in Synchrotron Radiation Research, edited by H. Winick and S. Doniach (plenum, New York, 1980).
19. J. J. Joyce and J. H. Weaver, Mater. Res. Soc. Symp., Boston, 1985 (in press).
20. D. J. Peterman and A. Franciosi, Appl. Phys. Lett. **45**, 1305 (1984).
21. P. Philip, A. Franciosi, and D. J. Peterman, J. Vac. Sci. Technol. A **3**, 1007 (1985); A. Franciosi, P. Philip, and D. J. Peterman, Phys. Rev. B **32**, 8100 (1985).
22. M. H. Patterson and R. H. Williams, J. Cryst. Growth **59**, 281 (1982).
23. L. J. Brillson, Surf. Sci. Repts. **2**, 123 (1982).
24. P. Skeath, I. Lindau, C. Y. Su, and W. E. Spicer, Phys. Rev. B **28**, 7051 (1983).
25. L. J. Brillson, C. F. Brucker, N. G. Stoffel, A. D. Katnani, and G. Margaritondo, Phys. Rev. Lett. **46**, 838 (1981).
26. L. J. Brillson, C. F. Brucker, A. D. Katnani, N. G. Stoffel, and G. Margaritondo, Surf. Sci. **132**, 212 (1983).
27. W. G. Petro, I. Babalola, T. Kendelewicz, I. Lindau, and W. E. Spicer, J. Vac. Sci. Technol. A **1**, 1181 (1983).
28. L. J. Brillson, C. F. Brucker, N. G. Stoffel, A. D. Katnani, R. Daniels, and G. Margaritondo, Physica **117/118B**, 848 (1983).
29. Davis et al. (Ref 6.) argue that because no Cd4d component is observed at the metallic Cd4d binding energy, which is 0.6 eV lower than in $Hg_{1-x}Cd_xTe$, there is no Cd in the overlayer. They therefore attribute the slow attenuation of the Cd intensity to islanding of Au on the semiconductor. However, using the formalism of Steiner and Hüfner (Ref. 30) relating heats of alloying to binding energy shifts, as applied by Nogami et al. (Ref. 31) to the metal/semiconductor interface, we calculate that the Cd4d for Cd in dilute solution in Au should be shifted on the order 1 eV to higher binding energy than the position for metallic Cd. Thus the absence of a Cd4d component at the metallic Cd position does not preclude the presence of Cd in the overlayer.
30. P. Steiner and S. Hüfner, Acta Metall. **29**, 1885 (1981).
31. J. Nogami, T. Kendelewicz, I. Lindau and W. E. Spicer (submitted to Phys. Rev. B).

3.2 CALCULATION OF CdTe BAND STRUCTURE

As an aid in completing the analysis of the angle-resolved data, calculation of the band structure of CdTe using the nonlocal pseudopotential of Chelikowsky and Cohen¹ was performed. The spectrum of computed energies and wave function spanned the valence bands and the high lying conduction bands up to 30 eV above the valence band maximum.

The results of this calculation shed insight into the role of the actual final states involved in the normal emission from CdTe (and by analogy, from $\text{Hg}_{1-x}\text{Cd}_x\text{Te}$) in shaping the features observed in the spectra. While a simple model of the final states that approximates them by free electron parabolas successfully accounts for much of the observed structure, certain peaks in the data reject instead the mixing of the parabolic bands that takes place in the crystal potential.² The calculation sheds light on this aspect in a semiquantitative way (trends are reproduced but quantitative comparison is not possible). The calculated valence and high-lying conduction bands along the Σ direction are illustrated in Figure 3-2. As the caption explains, states with a large [220] plane wave component (these contribute most strongly to the normal emission) are marked, and experimentally determined values of energy and k for selected transitions observed in the normal emission data from CdTe are also shown. While the data clearly falls in the region of high [220] density, the points occur at energies consistently higher than the calculation. The effect of mixing of the [220] and [002] parabolas is especially strong in the region around $k = 0.7$ ($2\pi/a$), and it is here that the structures marked No. 1 and No. 3 exhibit a nonmonotonic dependence of energy in the spectra of k in Figure 3-4.

The calculation was also used in a second way. The wave functions of each band were used to examine the optical transition matrix elements for interband transitions. These are the central elements determining the intensity of peaks in the spectra and contain the polarization dependence of the photoexcitation. In all cases that were examined, the calculated polarization dependence and the measured behavior agreed. This analysis requires knowledge of which bands participate in the interband transition; the agreement obtained is therefore confirmation of the accuracy of the assignment of the k -space origin of the features in the photoemission data.

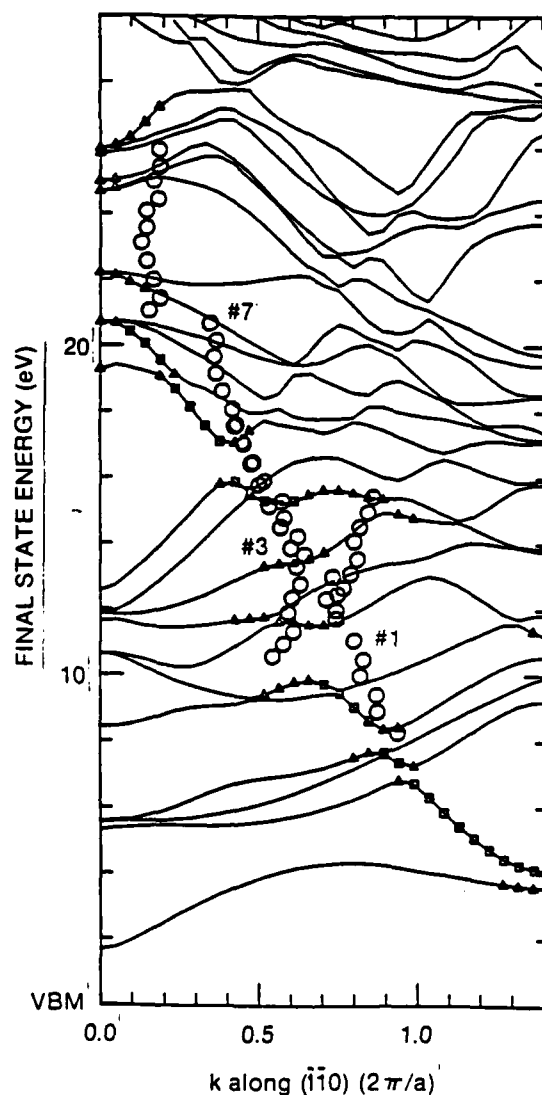


Figure 3-4. Calculated CdTe Conduction Bands of Σ_3 Symmetry and Identification of States With Greater Than 30% () or Between 10% and 30% (Δ) [220] Plane Wave Character. Also shown are portions of the experimental final states for peaks No. 1, No. 3, and No. 7 (O).

REFERENCES

1. J. R. Chelikowsky and M. L. Cohen, "Nonlocal Pseudopotential Calculations for the Electronic Structure of Eleven Diamond and Zinc-Blende Semiconductors," *Phys. Rev.*, B 14, 556 (1976).
2. J. A. Silberman, D. Laser, C. K. Shih, D.J. Friedman, I. Lindau, W. E. Spicer, and J. A. Wilson, "Angle-resolved Photoemission Spectroscopy of $\text{Hg}_{1-x}\text{Cd}_x\text{Te}$," *J. Vac. Sci. Technol.*, A 3, 233 (1985).

3.3 ANGLE-RESOLVED PHOTOEMISSION STUDY OF THE CdTe, HgTe and $\text{Hg}_{1-x}\text{Cd}_x\text{Te}$ BAND DISPERSIONS ALONG MAJOR SYMMETRY DIRECTIONS, AND THE ALLOYING EFFECT IN $\text{Hg}_{1-x}\text{Cd}_x\text{Te}$

Angle-resolved photoemission spectroscopy (ARPES) study on the band structure of $\text{Hg}_{1-x}\text{Cd}_x\text{Te}$ along [110] direction using normal emission method has been published by Silberman et al.¹ This work is an extension of the band mapping along other major symmetry directions ([111] and [100]) using off-normal emission method. By assuming direct transition model (DTM) and the free electron final state, the band mapping along [100] direction shows very good agreement with the band calculations by Chelikowsky et al.² for CdTe using nonlocal pseudopotential method, and Hass et al.³ for HgTe and $\text{Hg}_{1-x}\text{Cd}_x\text{Te}$ using empirical tight binding method. Part of our mapping results for the lower bands along [100] for CdTe and HgTe are shown in Figure 3-5. The assumption of free electron final state and DTM in the band mapping along [111] and mapping. Realistic final state calculation may be necessary for further analysis.

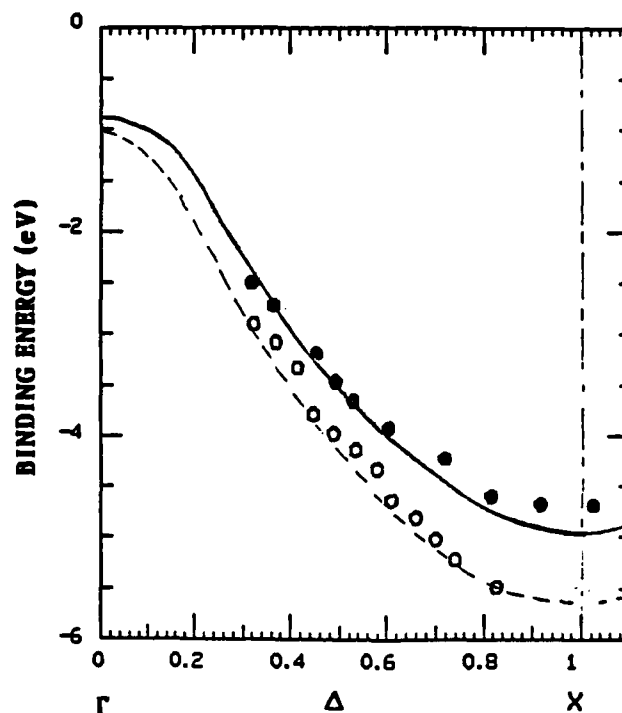


Figure 3-5. The Band Mappings of CdTe(●) and HgTe(o) Along [100] Direction Using Off-Normal Emission ARPES. The theoretical calculations for CdTe from Ref. 2 (solid line) and HgTe from Ref. 3 (dash line) are also shown for comparison. Only the lower bands are presented.

Besides the band mapping on the CdTe, HgTe and $\text{Hg}_{1-x}\text{Cd}_x\text{Te}$, ARPES is very useful in investigating the alloying effect on the substitutional alloy $\text{Hg}_{1-x}\text{Cd}_x\text{Te}$. In $\text{Hg}_{1-x}\text{Cd}_x\text{Te}$, the crystal structure remains single crystal (i.e. the lattice is periodic); however, the potential is aperiodic due to the random fluctuation of the chemical constituents. In treating the disorder problem in pseudobinary alloys, the Coherent Potential Approximation (CPA) which uses the virtual crystal potential as the unperturbed Hamiltonian and treats the chemical disorder as the perturbation, has been very successful in calculating the electronic structures of the substitutional alloys. In 1982 Spicer et al.⁴ published an experimental result showing the breakdown of virtual crystal approximation (VCA) in $\text{Hg}_{1-x}\text{Cd}_x\text{Te}$. There they used the angle-integrated photoemission spectroscopy to show that the density of states as a function of energy agree with the CPA rather than VCA calculation result. Besides the prediction in the density of states, the CPA also shows that the pure Bloch waves in VCA picture are now subjected to the alloy scattering resulting from the aperiodic potential term. This will result in the broadening and the peak shifting of the spectral density function deviating from the VCA Bloch state. Because the disorder in $\text{Hg}_{1-x}\text{Cd}_x\text{Te}$ manifests itself primarily in the difference of cation s-level energy associated with relativistic shifts, only the self-energy associated with the cation s-states Σ_s enters the spectral density functions $A(n, k, E)$:

$$A(n, k, E) = -\pi^{-1} f_s^c \sum_s'' \{ [E - E(n, k) - f_s^c \sum_s']^2 + (f_s^c \sum_s'')^2 \}^{-1}$$

where $E(n, k)$ is the energy of the VCA eigen state $|n, k\rangle$, $f_s^c(n, k)$ represents the fraction of time an electron in state $|n, k\rangle$ spends on cation s orbitals, \sum_s'' is the imaginary part of self energy, and \sum_s' is the real part of self energy. As one can see from the expression of the spectral function, \sum_s' and \sum_s'' reflect the energy shift and the damping of a particular VCA eigen state. Using ARPES, we can restrict ourself into the optical transition involving a particular initial state. Then by comparing the ARPES peaks of HgTe, CdTe, and $\text{Hg}_{1-x}\text{Cd}_x\text{Te}$ of the same k value, we are able to deduce the information of the peak shifts and broadenings. The alloy scattering is the strongest in the lowerband along [100] direction because it contains the largest cation s orbital contribution. In Figure 3-6 we show the experimental result of the alloy broadening and the energy shift of the lower band along

[100] direction (the details of the experimental deduction will be published elsewhere). We also show the theoretical calculation of the self energy Σ_s' and Σ_s'' by Hass and Ehrenreich³ in Figure 3-6. One should realize that the correct theoretical expression should also contain $f_s^c(n, k)$ which is not included in Figure 3-6. The theoretical calculation including $f_s^c(n, k)$ is underway. The experimental result shows strong variation of the peak shifts and the broadenings of the peaks versus binding energies is very significant -- the positions of the cross over of the peak shift (from negative to positive) and the maximum broadening agree very well with the theoretical prediction. The cross over of Σ_s' and the maximum of Σ_s'' happen at binding energy ~ 4.8 eV which corresponds the transition from the Hg s orbital contribution to the Cd s contribution (see the density of states projected on cation s orbitals, Figure 3-7).

REFERENCES

1. J. A. Silberman, D. Laser, C. K. Shih, D. J. Friedman, J. A. Wilson, I. Lindau, and W. E. Spicer, J. Vac. Sci. Tech. A 3, 233 (1985).
2. J. R. Chelikowsky and M. L. Cohen, Phys. Rev. B 14, 556 (1983).
3. K. C. Hass, H. Ehrenreich and B. Velicky, Phys. Rev. B 27, 1088 (1983).
4. W. E. Spicer, J. A. Silberman, J. Morgen, I. Lindau, J. A. Wilson, A.-B. Chen, and A. Sher, Phys. Rev Lett. 49, 948 (1982).

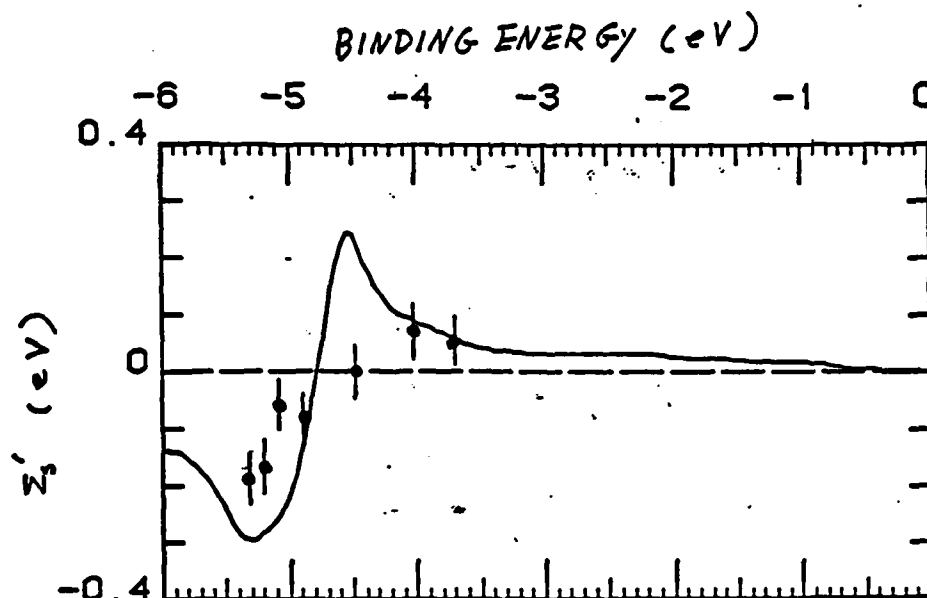


Figure 3-6(a). Comparison of the Theoretical Calculation of $\Sigma'_s(E)$ for $\text{Hg}_{0.7}\text{Cd}_{0.3}\text{Te}$ and the Experimental Result of the ARPES Peak Shift From the VCA Value of $\langle 100 \rangle$ Lower Band.

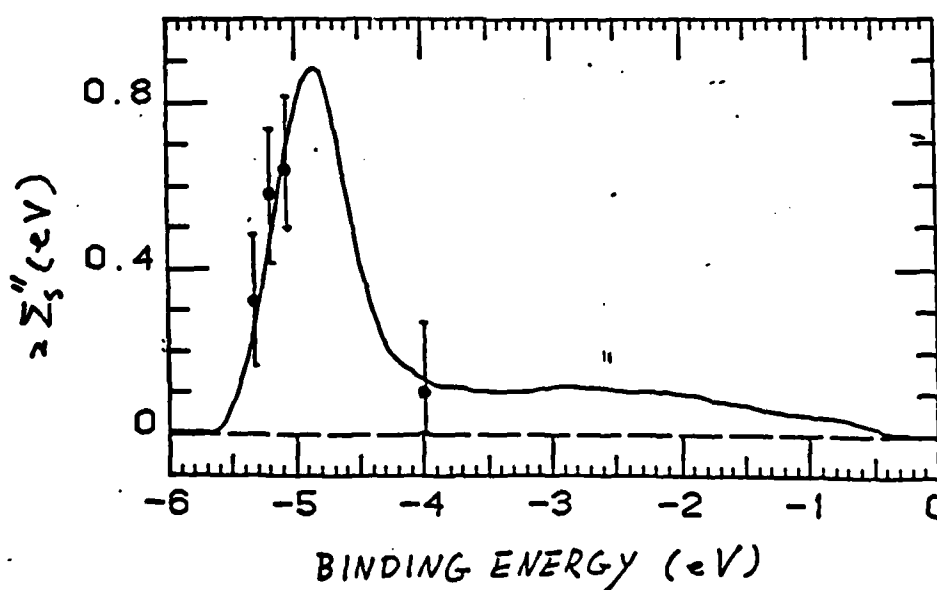


Figure 3-6(b). Comparison of $2\Sigma''_s(E)$ for $\text{Hg}_{0.7}\text{Cd}_{0.3}\text{Te}$ and the Experimental Result of ARPES Peak Broadening. The broadening data was obtained by comparing ARPES data of HgTe and $\text{Hg}_{0.7}\text{Cd}_{0.3}\text{Te}$ of the same photon energy $h\nu$, and analyzer angle θ_A .

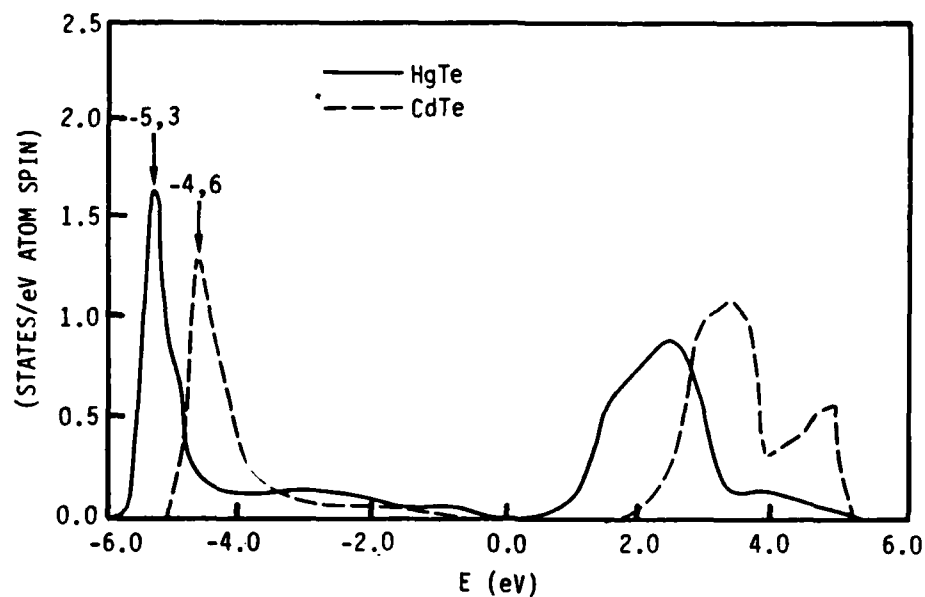


Figure 3-7. Density of States Projected on Cation s Orbitals for HgTe (Solid Curve) and CdTe (Dashed Curve) [cf. Eq. (17)].

Section 4 ALLOY BONDING

Results obtained on the alloy bonding task since July 1985 are contained in the following five papers. The first four are reprints of papers which were published in this period while the last one is a preprint accepted for publication in the Journal of Vacuum Science and Technology A.

Dislocation energies and hardness of semiconductors

A. Sher

SRI International, Menlo Park, California 94025

A.-B. Chen

Auburn University, Auburn, Alabama 36849

W. E. Spicer

Stanford University, Stanford, California 95305

(Received 13 July 1984; accepted for publication 5 October 1984)

The dislocation energies and hardness of semiconductors are calculated by an extension of Harrison's method. It is demonstrated in agreement with experiment that dislocation energies per unit length are proportional to $d^{-3} - d^{-9}$, where d is the bond length and hardness is proportional to $d^{-5} - d^{-11}$. The hardness is related to the interaction energies among dislocations. It is argued that dislocation densities of semiconductors will be reduced if they are alloyed with a second constituent that has a shorter bond length. Experimental evidence supporting this strategy is noted.

Dislocations in semiconductors are detrimental to device function; they serve as channels for impurity migration and trapping, which cause nonuniform doping and degrades p - n junctions.¹ They also decrease the material's resistance to plastic deformation. The aim of this letter is to provide insights into the underlying physical mechanisms controlling dislocations and semiconductor hardness, and then to suggest strategies for decreasing dislocation densities. It is well established that the hardness of tetrahedrally coordinated semiconductor materials—groups IV, III-V, and II-VI compounds—exhibits a sharp variation with their near-neighbor distance d , approximately proportional to d^{-9} for one group of seven compounds.² Thus, semiconductors with small lattice constants tend to be harder materials. These same materials have larger stiffness coefficients³ and have fewer dislocations in as-grown crystals.⁴⁻⁶

The shear coefficients (combinations of C_{44} and $C_{11} - C_{12}$ in the Schoenflies notation)⁷ depend on crystal orientation and (in Harrison's notation⁸) are proportional to $V_2^{1/2}/d^2(V_2^{1/2} + V_3^{1/2})^{1/2}$, where $V_2 \propto d^{-2}$ is the covalent and V_3 is the ionic energy. The metallic interaction modifies the functional dependence of the shear coefficient on V_2 and V_3 , but introduces no explicit dependence on the hopping integrals, denoted V , by Harrison.^{3,8} In a pure covalent material, the bond energy is proportional to V_2 (or d^{-2}), and the bond volume is $\propto d^3$; hence, in this case, the shear coefficient varies as d^{-2} . In the limit, $V_3 \gg V_2$, $C_{11} - C_{12} \propto d^{-11}$. For most polar semiconductors, d^{-9} is a good approximation.

Hardness is determined by applying a known force F to a probe of a prescribed shape driving it into the surface of the sample.⁷ The area A of the resulting indentation is measured, and the hardness is the force per unit indented area. Many dislocations must be formed to allow the probe to indent the semiconductor. If the indenter is a rectangular pyramid, then the hardness is $H = F/A = Fh/Ah = \epsilon_T/Ah$, where ϵ_T is the work required to cause the indenter to penetrate to a depth h . A side view of the indentation in a cut through its center is illustrated schematically in Fig. 1. The top of the indentation has side length W ; thus, $A = W^2$. The Burger's vector has magnitude b , proportional to the bond length d . The number of dislocations N_d required to accommodate an

indentation to depth h is $N_d = h/b = \frac{1}{2}W \cos \vartheta/b$, where ϑ is the angle between the normal to the tip of the indenter and a side. Figure 1 also shows a model of one possible configuration of the dislocations. The edges of the extra atom planes that are driven from the indented volume into the bulk of the semiconductor are shown as lines terminated by dots. The dotted ends of these lines are the positions of the dislocations, which are perpendicular to the plane of the figure. The planes driven to the sides each have a finite extent and a trapezoidal shape. The planes driven down under the indenter have a square shape.

Much of the work done on the indenter goes into the energy to form the indicated dislocation configuration, although some certainly goes into heat. There are two major contributions to this formation energy. The first is the energy needed to generate each dislocation as an isolated entity, and the second is the interaction energy among these dislocations. Because the interaction term dominates H , approximations made to simplify the first term are relatively unimportant. The extra planes driven to the sides of the indentation have a finite extent; accordingly (in this idealized picture), there are both edge dislocations at their base and screw dislocations associated with their termination. The square planes driven below the indentation have edge dislocations around the sides and screw dislocations at the corners to make the turns. Moreover, there are interactions

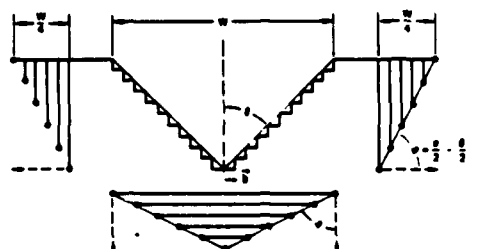


FIG. 1. Schematic representation of an idealized minimum-energy dislocation configuration produced by a square cross-section indenter in a hardness measurement. W is the side length and h is the depth of the indentation. In this ideal case, half the material from the indented region is displaced along the glide planes (indicated by the dashed arrows) to the sides and half is displaced below the indenter.

among the dislocations, which can produce a minimum-energy configuration. For the arrangement depicted in Fig. 1, it always costs energy to position a second dislocation on a parallel glide plane to one already present. However, the magnitude of this extra energy can be minimized and, for proper configurations of the dislocations, there are attractive forces along the glide planes that will tend to position the dislocations into the minimum-energy configuration. The minimum configuration arises when half of the atoms from the indented volume go respectively to the side and below the indenter. Then, in both regions, the maximum angle made between successive close-spaced dislocation lines and their glide planes is $\vartheta = \pi/2 - \vartheta/2$, as shown in the figure. This is the minimum realistic energy configuration. If the dislocations are separated more than shown in Fig. 1, then there is more volume of strained material and the interaction energy would be larger still.

An approximate expression for the energy required to indent the material is⁷

$$\epsilon_T = 2.4 \left[\sum_{i=1}^N E_i L_i + \frac{1}{2} \sum_{i,j=1}^N E_{ij} [\min(L_i, L_j)] \right] \quad (1)$$

In the first term, using an isotropic medium approximation and neglecting core terms, the energy per unit length to form an edge dislocation is⁷

$$E_i = \frac{Gb^2}{4\pi(1-\nu)} \ln \frac{R}{r_0} \quad (2)$$

the shear coefficient is G , the Burger's vector $b = d/3$ for an indentation along a $\langle 100 \rangle$ axis, the range of the elastic deformation of a dislocation R is taken equal to W (for want of a better approximation), $r_0 \sim d$ is the dislocation core radius, the Poisson ratio is $\nu \sim 0.2$ for most semiconductors, and L_i is the length of the i th dislocation. In the second term, E_{ij} is the interaction energy per unit length between dislocations i and j . Assuming they have parallel glide planes and their Burger's vectors have the same sign, E_{ij} is given by⁷

$$E_{ij} = \frac{Gb^2}{2\pi(1-\nu)} \left[\ln \left(\frac{R}{r_{ij}} \right) + \cos^2 \varphi_{ij} \right], \quad (3)$$

where r_{ij} is the separation, and φ_{ij} is the angle that a line perpendicular to and joining the dislocations makes with the glide plane, as shown in Fig. 1. Because the various dislocations in a region have different lengths, the net interaction energy is approximated by multiplying the energy per unit length by the length of the shorter one. The upper limits on the sums N are the number of dislocations in one region (side or bottom) associated with one edge. For the minimum-energy configuration, $N = N_h/2$. The four that multiplies the bracket accounts for the four sides, and the two for the two regions for each side.

We now encounter our first surprise. As we can see from Eq. (2) and (3), E_{ij} and E_i have comparable magnitudes. Because there are approximately N^2 terms in the interaction energy sum, only N terms in the formation energy sum, and N is a large number ($N \gg 1$), the interaction energy completely dominates the hardness. In fact, N is typically of the order 10^5 . Hence, terms owing to screw dislocations, core energies, heat dissipation as the dislocations propagate to their places, and other effects associated with the first term are unimpor-

tant. However, care must be taken with the interaction terms: Eq. (1) neglects a number of secondary interactions, some positive and others negative; these will be added later. The principal neglected terms are the interactions between the dislocations in the different regions on each side (positive), and the interactions between adjacent side and bottom regions (positive), and the interaction between the opposite sides in the bottom regions (negative). Comparison of the results with experiment will indicate how important these neglected terms are likely to be. The length L_i is $W(N-i)/N$ for i from 1 to N . This is the largest length of the side-inserted planes and its choice partially accounts for interactions between the otherwise neglected screw dislocations. The distance $r_{ij} = r_i - r_j$ is given by $2\sqrt{2}b|i-j|$ for i and j ranging from 1 to N for the minimum-energy configuration and a tetrahedrally bonded semiconductor. Finally, in the indicated configuration, $\varphi_{ij} = \varphi = \pi/2 - \vartheta/2$. Inserting these expressions into Eq. (1) and retaining only terms of order N^2 yields

$$H_{\min} = \frac{G \cot \vartheta}{6\pi(1-\nu)} \left[-\ln \left(\frac{\cot \vartheta}{\sqrt{2}} \right) + \frac{4}{3} + \sin^2 \frac{\vartheta}{2} \right]. \quad (4)$$

One can also get a number for the hardness of a dislocation in which all the material is pushed along the same glide plane, e.g., to the side, to the bottom, or normal to the face of the indenter (a possibility not depicted in Fig. 1). In this case, the factor of 2 in front of Eq. (1) is removed, $N = N_h$ and $\phi = \pi/2 - \vartheta$. Then a higher nonequilibrium hardness in the context of this model (denoted H_1), is obtained.

$$H_1 = \frac{G \cot \vartheta}{3\pi(1-\nu)} \left[-\ln \left(\frac{\cot \vartheta}{\sqrt{2}} \right) + \frac{4}{3} + \sin^2 \vartheta \right]. \quad (5)$$

The proper answer for most materials, and depending on crystal orientation, probably lies somewhere between H_{\min} and H_1 . For an indenter with $\vartheta = \pi/4$, we have $H_{\min} = 0.0969G/(1-\nu)$ and $H_1/H_{\min} = 2.39$. Harrison⁸ has shown that one contribution to the shear coefficient (actually $C_{11} - C_{12}$) is $G = 2.38 \hbar^2 m \alpha_c^3 / md^5$, where m is the free-electron mass, α_c is the covalence, $\alpha_c = V_2/(V_2^2 + V_3^2)^{1/2}$, and d is the bond length. We will approximate G by this expression. Using this G and $\nu = 0.2$, and changing the dimensions to those in terms of which experimental hardness numbers are customarily quoted gives $H_{\min} = 2.38 \times 10^4 (\alpha_c^3/d^5) \text{ kgm/mm}^2$, where d is in angstroms. Calculated values of H_{\min} and H_1 are plotted against experimental results in Fig. 2 for a number of semiconductors.

Figure 2 has the theoretical H_{\min} and H_1 values connected by arrows from H_{\min} to H_1 for each compound, plotted as a function of the corresponding experimental values.^{2,9} If the theory were perfect and the experimental values were accurate, the points would fall on the indicated unity slope line. Several conclusions can be drawn. First, the order of magnitude of the predicted and measured values are the same, a result obtained with no adjustable parameters in the theory. Secondly, the trends from one compound to another are properly given by the theory. Although the H_{\min} values are generally too small, they fit the soft materials better, and the H_1 values fit the harder materials better. Thirdly, from Eqs. (1) and (3), H is given in a rough but revealing

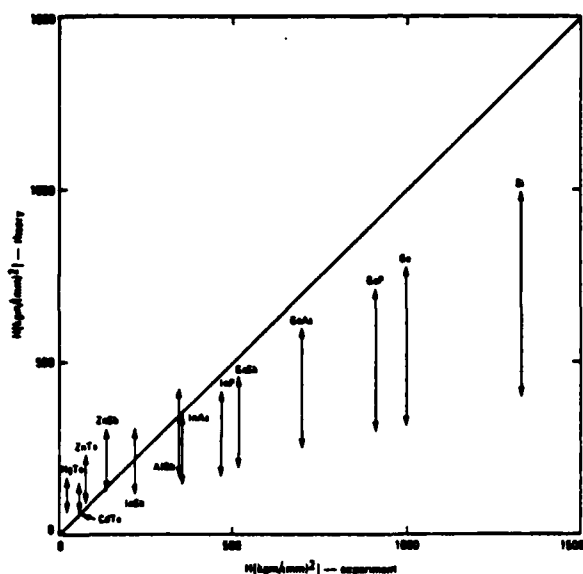


FIG. 2. Theoretical vs experimental hardness of several semiconductors in Refs. 2 and 9. The two theoretical values for each semiconductor are connected by an arrow from H_{min} to H_1 . Perfect agreement would correspond to points being on the unity-slope solid line.

approximation by $4N^2\bar{E}_y\bar{L}/Ah$, where the average dislocation length $\bar{L} = W/2$ and \bar{E}_y is the average dislocation pair interaction energy per unit length. Notice that N (or W) cancels from this expression; thus, H is independent of W (or F) and therefore, H is truly a measure of the properties of the material. This result would not be found if the dislocation energies ($\propto N$) were to dominate H rather than the pair interaction energy ($\propto N^2$). Finally, the Berger's vector cancels from the leading term and appears only in the argument of the logarithm in Eq. (3). Thus, the answers are also insensitive to its choice.

Dislocations are often found in materials as they are grown. Their density is determined by the thermal and mechanical stresses to which they are subjected in the growth process. A dislocation constitutes a metastable excitation relative to the perfect crystal ground state. At the elevated growth temperatures and temperature gradient behind the growth front, the number of dislocations present is controlled by the relative rate at which vacancies anneal or condense into dislocations.¹⁰ The dislocation formation rate will be slower in a material grown at the same temperature if E_f is higher. If an alloy is formed from a material of interest and a second constituent with a shorter bond length, one expects the average bond energy (and thus both the melt temperature and vacancy formation energy) to increase proportional to a low inverse power of the average bond length.⁸ Hence, the equilibrium vacancy density just below the melting point tends to be the same in lowest order for all materials, independent of the bond lengths of the constituents. However, the shear coefficient and dislocation energy per unit length will increase with much higher inverse powers of the bond length. Consequently, dislocation densities should be reduced in such alloys relative to those found in the longer bond length pure constituent. This expectation is confirmed

in the recent work reported on $Zn_{1-x}Cd_xTe$ bulk material.⁴ The best CdTe that has ever been grown has dislocation densities in excess of $5 \times 10^5 \text{ cm}^{-2}$. The addition of only 4% Zn reduced the dislocation count to less than $5 \times 10^4 \text{ cm}^{-2}$. The ZnTe bond length is 2.643 Å, while the CdTe bond length is 2.805 Å, a 6% difference. This 6% difference in bond length translates into a 2% difference in the dislocation energy per unit length for $1 - x = 0.04$. Dislocation energies per unit length are typically 10 eV per lattice spacing; accordingly, a 2% increase can be expected to slow their formation rate considerably.

The argument just presented naturally leads to a strategy for decreasing dislocations in other semiconductors. If an alloy is made of the material of interest with another compound with a shorter bond length, then the dislocation density should be reduced. For example, this suggests that the addition of a small amount of GaP ($d = 2.359 \text{ Å}$) may significantly reduce the dislocation density of bulk grown GaAs ($d = 2.448 \text{ Å}$). It has been demonstrated that the addition of approximately 1% GaN ($d = 1.946 \text{ Å}$)^{5,6} or of a 10^{18} cm^{-3} BAs ($d = 2.069 \text{ Å}$) concentration¹¹ to GaAs can yield a large volume of dislocation-free material. An InAs additive with its longer bond length ($d = 2.623 \text{ Å}$) serves the same function indirectly, by causing GaAs bonds in its neighborhood to be compressed. This indirect mechanism should be less effective than substituting short bond length additives.

We have demonstrated that the dislocation energies and hardness of tetrahedrally bonded semiconductors are rapid functions of the reciprocal of the bond length. This rapid d dependence of dislocation energies provides a rationale for the dramatic decrease of the dislocation density in bulk grown $Zn_{0.04}Cd_{0.96}Te$ material relative to that found in CdTe, and suggest means for accomplishing the same ends in other materials.

The authors are indebted to J. P. Hirth, W. A. Harrison, and T. N. Casselman for helpful comments. This work was supported in part by DARPA contract MDA 903-83-C-0108 and AFOSR contract 49620-81-K-0012.

¹E. M. Swiggard, Proceedings of GaAs IC Symposium, Phoenix, AZ 1983, p. 26.

²N. A. Groyunova, A. S. Borshchevskii, and D. N. Fretiaikov, in *Semiconductors and Semimetals*, edited by R. K. Willardson and A. C. Beer (Academic, NY, 1968), Vol. 4, Chap. 1.

³W. A. Harrison, *Electronic Structure and the Properties of Solids* (Freeman, San Francisco, 1980); R. C. Sokel, thesis, Stanford University, 1978; W. A. Harrison, *Microscience* (limited distribution SRI International publication, Menlo Park, 1983), Vol. 4, p. 34.

⁴S. L. Bell and S. Sen, presented at Infrared Imaging Systems (IRIS) Detector Specialty Group Meeting, Boulder CO, 1983; T. W. James and B. F. Zuck, *ibid.*

⁵J. Seki, H. Watanabe, and J. Matsui, *J. Appl. Phys.* 42, 822 (1983).

⁶G. Jacob, *J. Cryst. Growth* 59, 669 (1982).

⁷J. W. Christian, *Theory of Transformations in Metals and Alloys*, 2nd ed. (Pergamon, NY, 1975), Chap. 7. For a discussion of the interaction energies, see J. P. Hirth and J. Lothe, *Theory of Dislocations*, 2nd ed. (Wiley, NY, 1982), pp. 262-263.

⁸W. A. Harrison, *Phys. Rev. B* 27, 3592 (1983).

⁹S. Cole and A. F. W. Willoughby, *J. Cryst. Growth* 59, 370 (1982).

¹⁰G. Schoeck and W. A. Tiller, *Philos. Mag.* 5, 43 (1960).

¹¹S. Miyazawa, 1983 European Patent Application 833021652, filing date 4/18/83, and references therein.

Effects influencing the structural integrity of semiconductors and their alloys^{a)}

Arden Sher

SRI International, Menlo Park, California 94025

An-Ban Chen

Auburn University, Auburn, Alabama 36889

W. E. Spicer^{b)} and C-K Shih

Stanford University, Stanford, California 94305

(Received 1 June 1984; accepted 21 August 1984)

The bond length and energy changes of the constituents of alloys relative to their pure crystal values are calculated from an extension of Harrison's method. It is demonstrated that the already weak HgTe bonds are destabilized by adjacent CdTe, HgS, or HgSe, but are stabilized by ZnTe. It is also argued that dislocation energies and the hardness of semiconductors vary as a high inverse power of the bond length of the constituents. Hence, the shorter ZnTe bond as an additive should improve the structural properties of HgTe and CdTe. Experiments that support these predictions are noted. The electronic transport properties of 0.1 eV band gap HgZnTe are about the same as those of HgCdTe, and the structural properties of the Zn compound are superior; thus, we conclude that HgZnTe is likely to be the better material for IR devices.

I. INTRODUCTION

The objective of this work is to understand the microscopic mechanisms that govern the stability of $\text{Hg}_{1-x}\text{Cd}_x\text{Te}$ alloys, and then to suggest changes in the material that improve its strength without adversely affecting its electronic behavior. In pursuit of this goal we have extended Harrison's bonding theory,¹ which is applicable to all tetrahedral structured semiconductors, to calculate bond length and energy changes in an alloy—including charge shift and reconstruction effects—relative to their pure crystal values, vacancy formation energies, dislocation energies, and hardness.

In this paper, we review the experimental situation in several of these areas and compare some of the results with theory for all the group IV, III-V compound, and II-VI compound semiconductors and their alloys. For example, the theory properly predicts the observed inverse ninth power bond length (d^{-9}) dependence of the hardness² of semiconductors and, with no adjustable parameters, their correct magnitude. We demonstrate that the weak HgTe bond is destabilized by alloying it with CdTe, HgS, or HgSe; however, the bond is stabilized by ZnTe. Moreover, because the bond length of ZnTe (2.406 Å) is 14% shorter than that of HgTe (2.797 Å) or CdTe (2.804 Å), the dislocation energy per unit length and hardness of the alloys $\text{Hg}_{1-x}\text{Zn}_x\text{Te}$ and $\text{Cd}_{1-x}\text{Zn}_x\text{Te}$ are predicted in agreement with some experiments to be significantly higher than those of the compounds with $x = 0$. Measurements indicate that the electron and hole mobilities of $\text{Hg}_{1-x}\text{Zn}_x\text{Te}$ with $x \sim 0.16$, corresponding to a 0.1 eV band gap, are comparable to those of $\text{Hg}_{1-x}\text{Cd}_x\text{Te}$ for $x = 0.2$.³ This is to be expected, because the electron effective mass in a narrow-gap material is small; hence, the electron wave functions at Γ_{1c} are distributed over many atoms, with the result that alloy scattering rates are small at the band edge. The hole mobilities are large for a somewhat different reason: The valence band edge is mostly composed of Te p states; however, there is also some cation p state contribution. Because the p state energies of Hg and Zn

are nearly the same, the alloy scattering strength at the valence band edge is small. We conclude that, because of its structural advantage, HgZnTe may be superior to HgCdTe for infrared devices

II. ALLOY MODIFICATION OF THE BOND ENERGY AND LENGTH

A. Pure compounds

The first task is to recast Harrison's bond energy and bond length formalism into a structure suitable for generalization to alloys. Focus attention on the n th bond of a pure zinc blende structured compound semiconductor; for the time being, suppress any notation identifying it. Then, in a II-VI compound, the bond energy is¹:

$$E_b = \frac{\epsilon_p^+ - \epsilon_p^-}{2} + |V_{1+} + V_{1-}| - 2(V_2^2 + V_3^2)^{1/2} + 2 \sum_{l=0}^3 (\epsilon_{m-}^l + \epsilon_{m+}^l) + \frac{\gamma}{d^4}, \quad (1)$$

where the first term is the energy per bond needed to transfer two electrons from a p state on the group VI atom (the anion) to a p state on the group II atom (the cation), so that both start with four electrons (ultimately in the final bonding arrangement there is a net electron transfer from the cation to the anion), the second term is the promotion energy per bond to form sp^3 hybrids on both atoms, the third term is the bond formation energy owing to the covalent and ionic terms, the fourth term is Harrison's metallization energy, and the fifth term is the repulsive overlap energy that prevents the bonds from collapsing. The various symbols are defined below:

$\epsilon_{p\pm 1}$ is the $\left\{ \begin{smallmatrix} \text{cation} \\ \text{anion} \end{smallmatrix} \right\}$ p state correlated term values,⁴
 $V_{1\pm 1} \equiv (\epsilon_{p\pm 1} - \epsilon_{s\pm 1})/4$ are hopping integrals between two adjacent bonds coupled through a $\left\{ \begin{smallmatrix} \text{cation} \\ \text{anion} \end{smallmatrix} \right\}$,
 $\epsilon_{s\pm 1}$ are the $\left\{ \begin{smallmatrix} \text{cation} \\ \text{anion} \end{smallmatrix} \right\}$ s state correlated term values,
 $V_2 \equiv -24.5/d^2$ (eV) is the covalent energy,
 d is the bond length,

$$V_3 = (\epsilon_+ - \epsilon_-)/2,$$

$\epsilon_{1\pm} = (\epsilon_{s1\pm} + 3\epsilon_{p1\pm})/4$ are the sp^3 hybrid energies.

$$\epsilon_{m1\pm} = \sum_{j=1}^3 (U_{b1\pm}^o | U_{a1\pm} | V_{1\pm}^2 | / (\epsilon_b^o - \epsilon_a^o))$$

is the contribution to the reduction of the bonding state energy ϵ_b^o calculated by second-order perturbation theory of the bond in question (denoted by superscript o), owing to its interaction with the three neighboring ($i = 1-3$) antibonding states sharing the same {cation anion}

$$U_{b+} = \sqrt{(1 - \alpha_p)/2} = U_{a-},$$

$$U_{b-} = \sqrt{(1 + \alpha_p)/2} = U_{a+},$$

are the probability amplitudes of finding the cation and anion sp^3 -hybrid contributions to the bonding and antibonding states, e.g., U_{b+} is the probability amplitude of finding the cation³ hybrid in the bonding state, etc.,

$\alpha_p = V_3/\sqrt{V_2^2 + V_3^2}$ is the polarity,

$\alpha_c = |V_2|/\sqrt{V_2^2 + V_3^2}$ is the covalency,

$$\epsilon_{1\pm} = \frac{\epsilon_+ + \epsilon_-}{2} \pm \sqrt{V_2^2 + V_3^2},$$

are the bonding and antibonding one electron energy states owing only to covalent and ionic interactions,

$$\epsilon_{m1\pm} = \frac{(U_{b1\pm}^o | U_{a1\pm} | V_{1\pm}^2 |)}{\epsilon_b^o - \epsilon_a^o}, \quad i = 1, 2, 3$$

are the contributions to the bond in question arising from its antibonding state interactions with a neighboring bonding state i , and γ is an adjustable coefficient chosen so the measured bond lengths are reproduced.

Harrison has written Eq. (1) without explicit reference to the surrounding bonds. Equation (1) in its present form is rather easily used for alloy calculations by replacing host atom terms by one appropriate to the alloy.

The parameter γ for each compound is fixed by the condition that there is no net force on atoms at their equilibrium lattice positions. This condition is satisfied if the gradient of the total energy with respect to all the bond lengths vanishes:

$$\nabla_{d_n} E_T = 0, \quad \text{where } E_T = \sum_n E_b^n.$$

The condition is equivalent to the requirement that the net bond tension $T_{on} + T_{mn}$ for the n th bond equals the repulsive force

$$T_{on} + T_{mn} - \frac{4\gamma_n}{d_n^3} = 0, \quad (2)$$

where

$$T_{on} = \frac{\partial}{\partial d_n} (-2\sqrt{V_2^2 + V_3^2}) = 4\alpha_c \sqrt{V_2^2 + V_3^2}/d, \quad (3)$$

$$\begin{aligned} T_{mn} &= 2 \frac{\partial}{\partial d_n} \sum_{i=0}^3 (\epsilon_{m+n}^i + \epsilon_{m-n}^i), \\ &= \sum_{i=0}^3 (T_{m+n}^i + T_{m-n}^i). \end{aligned} \quad (4)$$

TABLE I. Correlated term values and bond energies for three II-VI compounds. The experimental bond lengths, polarity, and metallic contribution to the bond energy are also plotted

Atom	Correlated term values (eV)		
	s	p	sp^3
Zn	-10.224	-4.920	-6.246
Cd	-9.611	-4.784	-5.991
Hg	-10.946	-4.872	-6.391
Te	-19.620	-9.824	-12.273

Compound	d (Å) ^a	Bond energies		E_b (eV)
		α_p	E_{metallic} (eV)	
ZnTe	2.643	0.652	-0.625	-0.985
CdTe	2.805	0.710	-0.466	-0.944
HgTe	2.797	0.685	-0.614	-0.480

^aReference 12.

The last identity in Eq. (4) defines the indicated bond tensions. Collecting all the results from the earlier paragraphs, one finds (dropping the bond designation n):

$$T_{m-}^o = -\frac{4}{d} \left[(1 + \alpha_p)\alpha_p + \frac{\alpha_c^2 \sqrt{V_2^2 + V_3^2}}{\epsilon_b^o - \epsilon_a^o} \right] \epsilon_{m-}^o, \quad (5a)$$

$$\begin{aligned} T_{m-}^1 &= T_{m-}^2 = T_{m-}^3 \\ &= \frac{4}{d} \left[(1 - \alpha_p)\alpha_p - \frac{\alpha_c^2 \sqrt{V_2^2 + V_3^2}}{\epsilon_b^o - \epsilon_a^o} \right] \epsilon_{m-}^1, \end{aligned} \quad (5b)$$

$$T_{m-}^o = \frac{4}{d} \left[(1 - \alpha_p)\alpha_p - \frac{\alpha_c^2 \sqrt{V_2^2 + V_3^2}}{\epsilon_b^o - \epsilon_a^o} \right] \epsilon_{m-}^o, \quad (5c)$$

$$\begin{aligned} T_{m-}^1 &= T_{m-}^2 = T_{m-}^3 \\ &= -\frac{4}{d} \left[(1 + \alpha_p)\alpha_p + \frac{\alpha_c^2 \sqrt{V_2^2 + V_3^2}}{\epsilon_b^o - \epsilon_a^o} \right] \epsilon_{m-}^1. \end{aligned} \quad (5d)$$

Finally combining Eqs. (1)-(5), the bond energy is

$$\begin{aligned} E_b &= -1(1 + \alpha_p^2)(V_2^2 + V_3^2)^{1/2} \\ &\quad - \frac{9}{8}(1 - \alpha_p^2)^2 \frac{(V_{1+}^2 + V_{1-}^2)}{(V_2^2 + V_3^2)^{1/2}} \\ &\quad + |V_{1+} + V_{1-}| + \frac{\epsilon_p^+ - \epsilon_p^-}{2}. \end{aligned} \quad (6)$$

Equation (6) was first derived by Harrison using a much simpler argument.¹ The bond energies quoted in Table I and on Fig. 5 are calculated from this expression, using as input the correlated term values from Table I and the experimental bond lengths.

B. Alloy calculations

There are several layers of sophistication that can be used to compute the bond energy and length changes between pure compounds and their alloys. However, all the calculations are motivated by the EXAFS experimental result found first for $\text{Ga}_{1-x}\text{In}_x\text{As}$ and later in other compounds.⁵ It was found that, while the average bond length in the alloy follows Vegard's rule and varies linearly between those of the pure constituents, the individual bond lengths of GaAs and

NO-A166 795

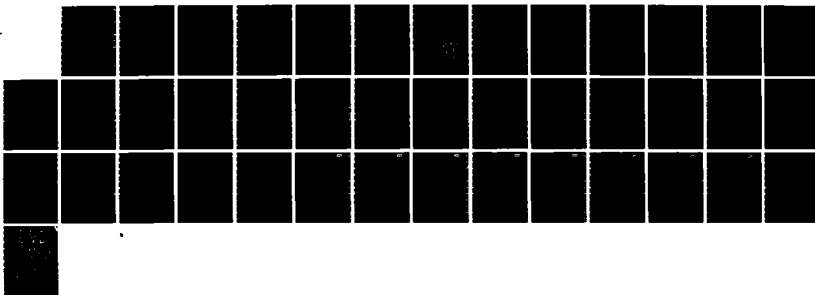
HQCDTE SURFACE AND DEFECT STUDY PROGRAM(U) SANTA
BARBARA RESEARCH CENTER GOLETA CALIF J A WILSON ET AL.
MAR 86 SBRC-60411 MDA903-83-C-0108

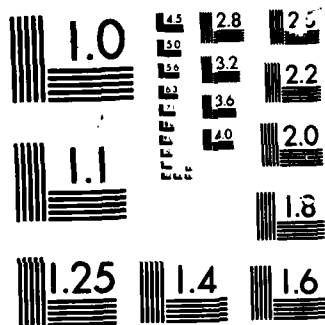
2/2

UNCLASSIFIED

F/G 20/12

NL





MICROCOPY

CHART

InAs are nearly the same as those of the pure materials—changing by only about 4%. The shorter GaAs bond increases its length when it is an impurity in an InAs host by about 4%, and the longer InAs bond shrinks by about 4% in the opposite extreme where it is the impurity in GaAs. The lattice fits together by having the metal sublattice nearly retain its fcc structure with a lattice constant following Vegard's rule, and each As atom adjusts its local position and accommodates to which metal atoms occupy its four neighboring sites. Thus there are five local arrangements; in the first an As atom is surrounded by four Ga atoms [a Ga(4)In(0) configuration], in the second there are three Ga atoms and one In [a Ga(3)In(1) configuration], and the last three configurations are Ga(2)In(2), Ga(1)In(3), and Ga(0)In(4). In a general cation $A_{1-x}B_xC$ alloy or anion $CA_{1-x}B_x$ alloy, the generalizations are obvious, and one can examine $A(4-\eta)B(\eta); \eta = 1, 2, 3, 4$ configurations.

1. Method 1

The lowest level of approximation that takes account of these findings calculates [from Eqs. (1) and (2)] a given bond's energy and length shift when its surrounding bonds have different constituents. The calculation is done assuming that the surrounding bonds retain their pure crystal bond lengths. This model is somewhat unrealistic, in that it ignores the strains that must be present to allow the lattice to fit together. However, it is nonetheless useful because it treats the largest terms, viz. those arising from charge transfer between the substituted species in the alloy, and results in analytic expressions, while the successively more complicated treatments must be done numerically. It is also useful later because, taken together with the more complete calculations, it allows one to judge the relative contribution from different physical effects. From Eq. (1) in a cation-substituted alloy one can deduce an expression for the energy shift of an AC bond when η surrounding bonds are replaced by BC, ΔE_b^η as

$$\begin{aligned} \Delta E_b^\eta = & \frac{2[U_b^0 - U_b^1(BC)V_{1-}]^2}{\epsilon_b^0 - \epsilon_b^1(BC)} \\ & - \frac{2[U_b^0 - U_b^1(AC)V_{1-}]^2}{\epsilon_b^0 - \epsilon_b^1(AC)} \\ & + \frac{d\partial}{4\partial d} 2 \left\{ \frac{[U_b^0 - U_b^1(BC)V_{1-}]^2}{\epsilon_b^0 - \epsilon_b^1(BC)} \right. \\ & - \frac{[U_b^0 - U_b^1(AC)V_{1-}]^2}{\epsilon_b^0 - \epsilon_b^1(AC)} \\ & + \frac{[U_b^1(BC)U_b^0 - V_{1-}]^2}{\epsilon_b^1(BC) - \epsilon_b^0} \\ & \left. - \frac{[U_b^1(AC)U_b^0 - V_{1-}]^2}{\epsilon_b^1(AC) - \epsilon_b^0} \right\}, \quad (7) \end{aligned}$$

where the partial derivative is taken with respect to the central bond length (a term designated with a superscript 0) and in this simple approximation

$$\Delta E_b^\eta = \eta E_b^1, \quad \eta = 0, 1, 2, 3. \quad (8)$$

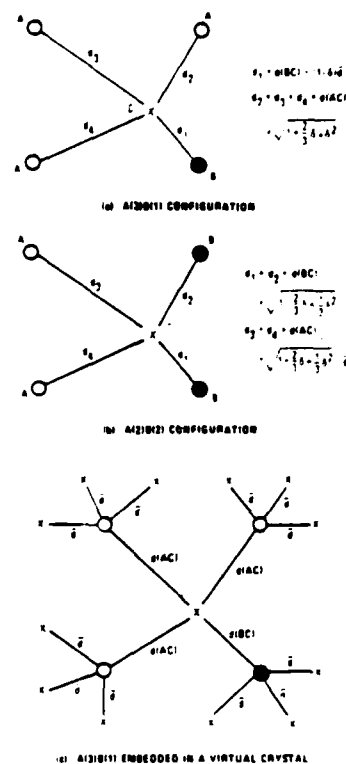


FIG. 1. Schematic view of various bond configurations. (a) A(3)B(1) configuration, (b) A(2)B(2) configuration, and (c) A(3)B(1) configuration embedded in a virtual crystal.

The bond length shifts are found from Eq. (2). The modification of these expressions for an anion-substituted alloy follows from symmetry.

2. Method 2

A more realistic calculation includes strain and permits the lattice to fit together. The simplest non-self-consistent, near-neighbor version of this calculation proceeds as follows. In a cation-substituted alloy $A_{1-x}B_xC$ (e.g., $Hg_{1-x}Cd_xTe$ or $Zn_{1-x}Hg_xTe$), the cations are assumed to occupy their regular fcc sublattice sites, while the anions accommodate to their local configuration. The average lattice constant is taken to follow Vegard's rule:

$$\bar{d} = (1-x)d_0(AC) + xd_0(BC), \quad (9)$$

where d_0 and $d_0(BC)$ are the pure crystal lattice constants. Then in an A(3)B(1) configuration [see Fig. 1(a)], the anion will be displaced along the BC bond. For definiteness, suppose $d(AC) > d(BC)$; then the anion will be shifted away from the tetrahedral site toward the B atom. Because $d_0(AC) > d_0(BC)$, the $d(BC)$ bond will be elongated and the $d(AC)$ bonds will also be locally elongated in a strained configuration. We can for this case [see Fig. 1(a)] write

$$d(BC) = (1-\delta)\bar{d} \quad (10)$$

and for the three AC bonds

$$d(AC) = \sqrt{1 + \frac{2\delta}{3} + \delta^2} \bar{d}. \quad (11)$$

In an A(2)B(2) configuration [see Fig. 1(b)], we have for both BC bonds

$$d(BC) = \sqrt{1 - \frac{2}{3}\delta + \frac{1}{3}\delta^2 \bar{d}}, \quad (12)$$

and for both AC bonds

$$d(AC) = \sqrt{1 + \frac{2}{3}\delta + \frac{1}{3}\delta^2 \bar{d}}. \quad (13)$$

The values of δ are determined by the condition $\partial E_T / \partial \delta = 0$, or

$$\sum_{n=0}^3 \left(T_{on} + T_{mn} - \frac{4\gamma_n}{d_n^2} \right) \frac{\partial d_n}{\partial \delta} = 0. \quad (14)$$

Equation (14) is solved by

- (1) Assigning the γ_n s their pure crystal values.
- (2) Supposing that the four tetrahedrally configured anions are embedded in the virtual crystal [see Fig. 1(c)].
- (3) For each x , δ is varied and the bond tensions are calculated and inserted into Eq. (14) until a value of δ is found that satisfies this equation.

The computer outputs are δ and the AC and BC bond energies. This method can be extended to take explicit account of the bond length variations of larger clusters, and \bar{d} can be calculated explicitly (instead of using Vegard's rule) so the results can be made to be self-consistent. Also, effects arising from bond angle distortions can be included. The major effects that are currently included in the calculation arise from the bond length dependence of V_2 , and charge shifts driven

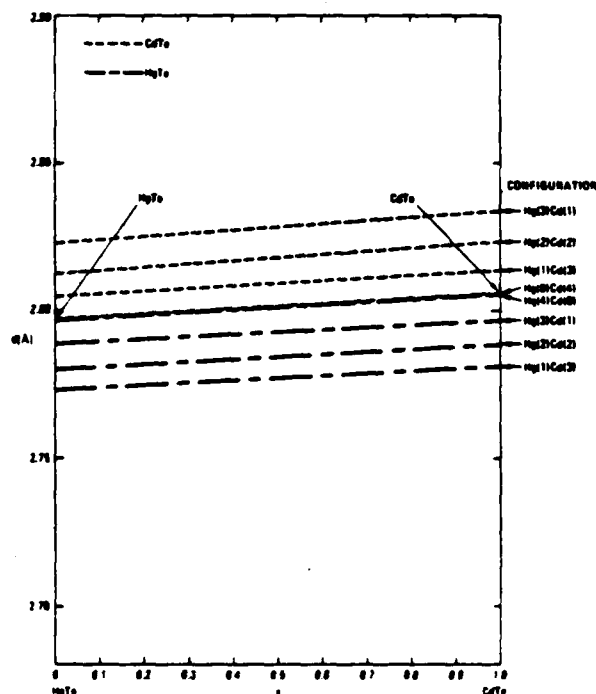


FIG. 2. Bond lengths as a function of concentration x for the $Hg_{1-x}Cd_xCdTe$ alloy in different configurations. The short dashed lines are for the CdTe bonds and the long-short dashed lines represent the behavior of the HgTe bonds.

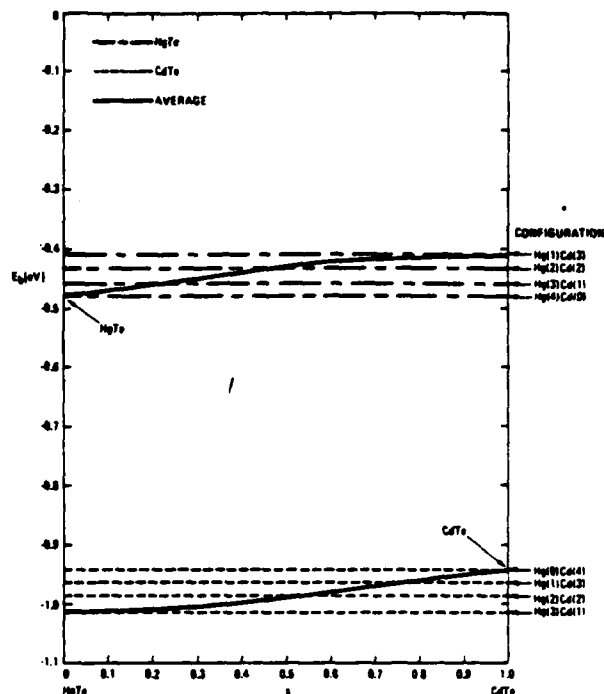


FIG. 3. Bond energy as a function of concentration x for the $Hg_{1-x}Cd_xCdTe$ alloy in different configurations. The short dashed lines are for the CdTe bonds and the long-short dashed lines represent the behavior of the HgTe bonds. The solid lines are the concentration weighted averages of the respective bond energies.

by hybrid energy differences and coupled through the metalization terms. However, V_2 is also sensitive to bond angle distortions, and these effects are not included in the present results. We expect their inclusion will modify the quantitative results by 10%–30%, but not the trends.

C. Results

The correlated atomic term values⁴ for the elements in the more common II–VI compounds are listed in Table I, along with the bond energies of their nine compounds. The valence s state energies for Zn are large, become smaller as for Cd, and then (in an unusual occurrence) the trend reverses and the Hg s levels are deeper again. This is caused by the relativistic terms that become important in Hg. The p state levels have a similar trend; however, the differences among the atoms are much smaller. The levels of the anions are deeper than those of the cations. Thus, there is a net electron transfer from the cations to the anions, which is responsible for the ionic contribution to the bonding. The polarity, also listed in Table I, reflects the relative contribution of ionic and covalent character to the bonds. Notice that α_p is small for ZnTe larger for CdTe, and smaller again for HgTe. By contrast, the metallic contribution E_m is large for ZnTe and HgTe and small for CdTe. In fact, HgTe would not be bound if it were not for the metallic contribution to the bond, not a terribly surprising result, because HgTe is a semimetal. The bond lengths of CdTe and HgTe are very nearly the same, but this is an accident resulting from the balance of contribu-

tions to their bonds: CdTe is dominated by the covalent and ionic contributions to its bond, while HgTe has bonds that are mostly covalent and metallic. We should therefore not be too surprised if their alloy displays some unusual bond length variations.

Figures 2 and 3 illustrate the $\text{Hg}_{1-x}\text{Cd}_x\text{Te}$ alloy concentration variations of the length and energy for the five configurations. These results were calculated using the second method discussed in Sec. II B. In Fig. 2 we see the unexpected result that the shorter HgTe bond becomes still shorter in the alloy, while the CdTe bond length increases. Moreover, the changes are large compared to the original length difference. Thus, one can expect to find local microstrains, even in this nearly lattice-matched material. The bond energy variations shown in Fig. 3 also display an important result. The already weak HgTe bond is destabilized by the presence of Cd. The flat concentration variation of the bond lengths and energies is peculiar to HgCdTe ; much more structured behaviors are exhibited by other compounds.

Several considerations to keep in mind when dealing with alloys are depicted schematically in Fig. 4 for a $\text{Hg}(3)\text{Cd}(1)$ configuration. Due to the charge shift alone, the HgTe bond shrinks by 0.030 Å, the minimum in the configuration diagram moves to a smaller bond length and the depth of the well is decreased. Then the bond is stretched by 0.011 Å to its final length. Thus, the bond is not centered at a local mini-

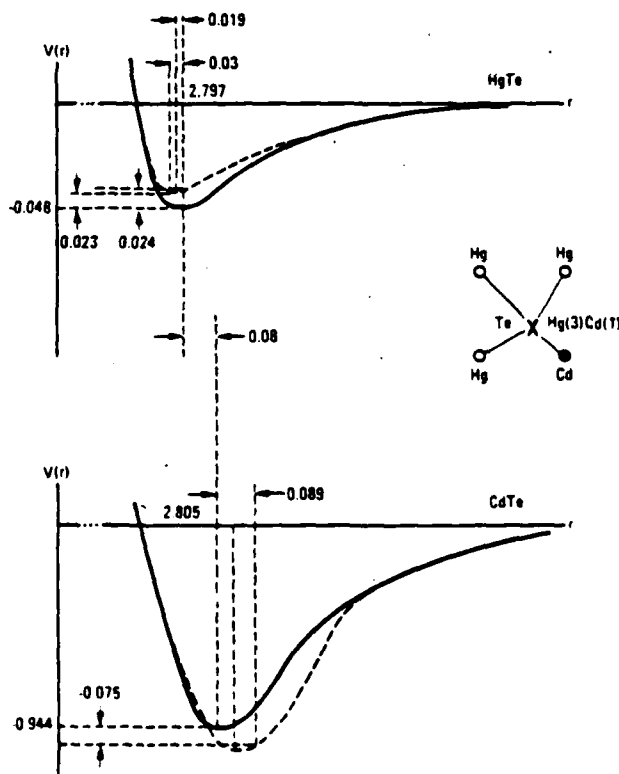


FIG. 4. Schematic picture of a potential configuration diagram for the HgTe and CdTe bonds in an Hg_3Cd_1 configuration. For the HgTe bond the energy and position of the bond center are calculated by method 1 of Sec. II B and the final stretched position and energy by method 2. The results quoted for the CdTe bond are those determined by method 2.

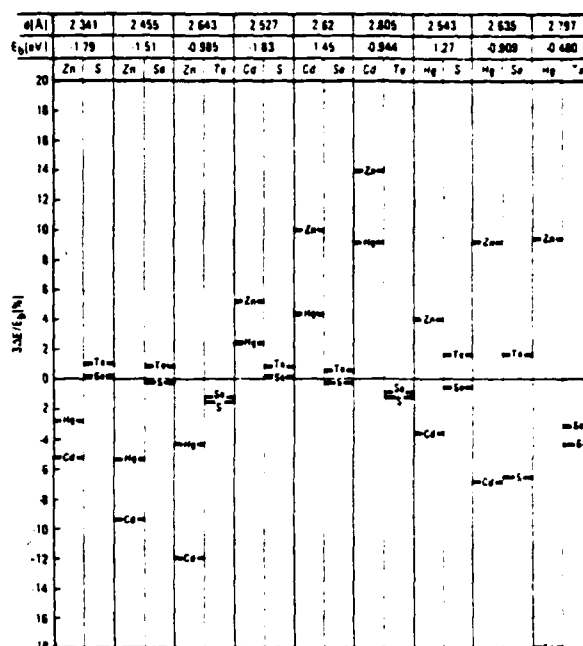


FIG. 5. AC bond energy shifts for the II-VI compounds in $A(1)B(3)$ configurations expressed as a percentage of the pure crystal bond energy. The B atom is designated in the line that shows the shift. The pure crystal AC bond energies and lengths are given at the top of the figure. These numbers were calculated by method 1 in Sec. II B.

um. For example, this implies that the force constant of local phonon modes will be related to the second derivative of this configuration diagram evaluated at the strained position away from the well minimum. This effect is even more pronounced for materials with a larger lattice mismatch. Notice that the CdTe bond is also stretched relative to its local minimum in this configuration.

The result for bond energy variations for all the II-VI compound alloys is gathered in Fig. 5. Here the energy shifts of an AC bond in a $A(1)B(3)$ configuration $\Delta E_b/E_b = 3\Delta E_b/E_b$ are presented as a percentage of the pure material bond energy for cation substitute alloys along with equivalent results for anion substantial alloys, e.g., $\text{HgS}_{1-x}\text{Te}_x$. The energy shifts are calculated following the first method presented in Sec. II B. We have not had the opportunity to run all the compounds following the more sophisticated calculational procedure. The bond at the top of a column is the one whose energy shift is calculated, and the other constituent is identified in the line that indicates the energy shift. A negative $3\Delta E_b/E_b$ is destabilizing and a positive one stabilizing. Focus on HgTe. It is destabilized by CdTe, HgS, and HgSe, but is stabilized by ZnTe. The CdTe destabilizes the HgTe bond by 18% according to the simple calculation and by 15% according to the better one. The difference between Zn and Cd occurs because in the Cd case there is a net electron transfer from the Cd to the Hg, while in the case of Zn there is practically no such transfer. These extra transferred electrons must occupy antibonding states, because the bonding states on the HgTe are full, so the net effect (including other energy state shifts) is to destabilize the HgTe bond. This predicted destabilization of the HgTe bond in HgCdTe alloys

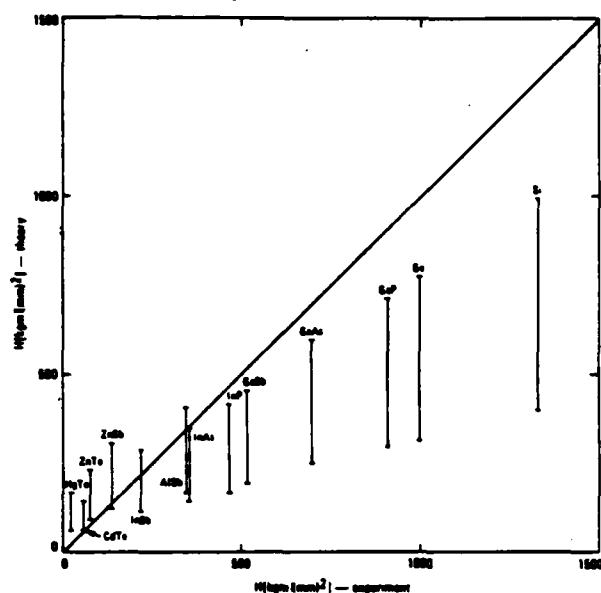


FIG. 6. Theoretical vs experimental hardness. The two values at the top and bottom of the vertical lines designated for each compound were calculated for two different possible dislocation arrangements. The lower one corresponds to the minimum energy configuration and the upper one to a likely higher energy configuration. The experimental numbers were taken from Ref. 2.

agrees with the d state energy shift reported by Spicer *et al.* at last year's workshop,⁶ and by the oxygen uptake experiments presented by the same group at this conference.⁷

III. DISLOCATION ENERGIES AND HARDNESS

The dislocation energies and hardness of semiconductor are calculated by an extension of Harrison's method.¹ It is demonstrated, in agreement with experiment, that dislocation energies per unit length, depending on the covalency, are proportional to d^{-9} , where d is the bond length and hardness is proportional to d^{-5} to d^{-11} . The low powers are for pure covalent materials. The hardness is related to the interaction energies among dislocations. The detailed theory will be published elsewhere.⁸

Figure 6 shows the theoretical hardness of several semiconductors plotted against experimental values.² The theory is calculated for two different dislocation configurations caused by the extra material pushed by the indenter into the crystal. The lower end of each vertical line is a realistic hardness for the minimum energy configuration, and the upper ends of the lines are the values found for a higher-energy configuration. In most cases, one would expect real configurations to have hardnesses lying somewhere between these two values, once the effect of heat generated by the indentation process is subtracted from the experimental numbers. This theory has no adjustable parameters, yet it predicts the right trends and magnitudes.

IV. NATIVE IMPERFECTIONS GROWN INTO ALLOYS

There are two kinds of imperfections we shall discuss: vacancies and dislocations. At present, the conclusions are tentative, because the detailed theory is still incomplete. Va-

cancy formations energies and the melting temperature are both proportional to the bond energies of the constituents. Thus, one would expect the vacancy density just below the melting point to be about the same for all materials with a similar coordination number; in our semiconductor case, the coordination number is four. Dislocation energies are mostly owing to long-range bond angle distortions⁹ and accordingly are sensitive to the shear coefficients, which vary roughly as d^{-7} for many compounds.¹ Based on this general argument, one would expect to find fewer dislocations in materials with short bond lengths.

Dislocations appear in bulk grown materials through a sequence of steps.¹⁰ We shall only discuss the simplest case, where there are no mechanical stresses on the growing material. In the temperature gradient behind the growth front, there is usually a supersaturated vacancy content. These excess vacancies may diffuse to surfaces where they do no harm, or they may condense into vacancy clusters that can then organize into dislocation loops. If a loop is not parallel to the growth front, it can climb toward the front by absorbing more vacancies. If it climbs faster than the growth progresses, then the loop will reach the front. It can then spread and grow along with the crystal. Observed from the growth surface, such a loop will appear to be two edge dislocations. If this dislocation formation process can be inhibited in any of its steps, the resulting material will have fewer dislocations.

Zn in $\text{Zn}_{1-x}\text{Cd}_x\text{Te}$ or $\text{Zn}_{1-x}\text{Hg}_x\text{Te}$ will serve this function in two ways. The first is that Zn stabilizes the weaker bond in these alloys; accordingly, vacancy formation energies in the alloy should be larger than those in the pure constituent CdTe or HgTe. The melting temperature will also be raised somewhat; which effect "wins" is a matter still to be decided. The second effect is clear cut: The shorter bond lengths of the ZnTe will introduce stiff struts into the system that will increase the dislocation energies and thus should inhibit dislocation loop formation and subsequent climb. The large dislocation density reduction found by Bell and Sen in $\text{Zn}_{1-x}\text{Cd}_x\text{Te}$ with only 4% Zn supports this speculation.¹¹

V. CONCLUSIONS

We have argued that, in an alloy, the bond energies and bond lengths are modified from their pure crystal values. Bond energies can be strengthened or weakened in an alloy depending on the relative sp^3 state energies and the consequent net electron shift between the constituents. For most compounds, the average bond length modifications for each type of bond are generally small compared to those suggested by Vegard's rule, in agreement with experiment. However, HgCdTe is an exceptional case, because the bond lengths for HgTe and CdTe are nearly the same (by accident). The bond length and energy shifts also depend sensitively on the local configuration and the bonds are locally strained. These effects must be taken into consideration in a proper theory of alloy vacancy formation energies, phonon frequencies, dislocation energies, etc.

The conclusions most relevant to the initial question posed in the introduction are that for the narrow gap allows:

Cd destabilizes the already weak HgTe bond and has little effect on the dislocation energy.

Zn both stabilizes the HgTe bond and increases the dislocation energy.

Zn also decreases the dislocation density of CdTe to improve substrates.

HgZnTe electron and hole mobilities are about the same as those of comparable band gap HgCdTe.

HgZnTe is likely to be a superior material to HgCdTe for detectors operating in the 8–12 μm regime.

⁴¹This work was supported in part by AFOSR Contract No. F496280-81-K-0012 and by DARPA Contract No. MDA-903-83-0-0108.

⁴²Stanford Ascherman Professor of Engineering.

⁴³W. A. Harrison, *Electronic Structure and the Properties of Solids* (Freeman, San Francisco, 1980); R. C. Sokel, thesis, Stanford University, 1978.

W. A. Harrison, *Microscience* (SRI International, Menlo Park, California, 1983), Vol. IV, p. 34 limited-distribution.

⁴⁴N. A. Goyunova, A. S. Borshchevskii, and D. N. Fretaiakov, *Semiconductors and Semimetals*, edited by R. L. Willardson and A. C. Beer (Academic, New York, 1958), Vol. IV, Chap. I.

⁴⁵O. Mukhina, A. M. Gulyaev, A. S. Shnurnikov, and I. V. Yamshchikova, *Tr. Mosk. Energ. Inst.* 443, 16 (1980).

⁴⁶A. B. Chen, A. Sher, and W. E. Spicer, *J. Vac. Sci. Technol. A* 1, 1674 (1983).

⁴⁷J. C. Mikkelsen, Jr. and J. B. Boyce, *Phys. Rev. Lett.* 19, 1412 (1982), and private communications.

⁴⁸W. E. Spicer, J. A. Silberman, I. Landau, A. B. Chen, A. Sher, and J. A. Wilson, *J. Vac. Sci. Technol. A* 1, 1735 (1983).

⁴⁹J. A. Silberman, D. Laser, I. Landau, and W. E. Spicer (these proceedings).

⁵⁰A. Sher, A. B. Chen, and W. E. Spicer, *Appl. Phys. Lett.* 46, 54 (1985).

⁵¹J. P. Hirth and J. Lothe, *Theory of Dislocations*, 2nd ed. (Wiley, New York, 1982).

⁵²G. Schoeck and W. A. Tiller, *Philos. Mag.* 5, 43 (1960).

⁵³S. L. Bell and M. Sen (these proceedings).

⁵⁴R. Zallen, *Handbook of Semiconductors*, edited by T. S. Moss and W. Paul (North-Holland, Amsterdam, 1982), Vol. I, Chap. 1.

Bond-length relaxation in pseudobinary alloys

C. K. Shih, W. E. Spicer, and W. A. Harrison
 Stanford University, Stanford, California 94305

Arden Sher
 SRI International, Menlo Park, California 94025
 (Received 17 September 1984)

The bond-length relaxation in pseudobinary alloys can be predicted by a simple radial force model. In tetrahedral structure alloys the bond-length deviation of the solute in the dilute solution is a quarter of the bond-length difference between the two components. This result agrees with the experimental work done on the $\text{Ga}_{1-x}\text{In}_x\text{As}$ system performed by Mikkelsen and Boyce.

In calculating pseudobinary alloy properties, the nearest-neighbor distance is a very important parameter. For many years people have used the virtual-crystal approximation (VCA) which assumes that all atoms occupy the average lattice positions. In 1982 Mikkelsen and Boyce used extended x-ray-absorption fine structure (EXAFS) to study the atomic scale structure of the $\text{Ga}_{1-x}\text{In}_x\text{As}$ system.¹ They found that the Ga-As and In-As bond lengths did not follow the VCA; instead, they only slightly deviated from their natural bond lengths even in the dilute solutions, and the magnitude of the bond-length deviation at the dilute limit was about a quarter of the difference of the natural bond lengths of the two components (GaAs and InAs). These results can be explained by a simple radial force constant model in which the weaker angular forces are neglected.

Consider a compound GaAs in which one of the Ga atoms is replaced by an In atom. This configuration represents the dilute limit of In-As in a GaAs host (see Fig. 1). In this configuration, four In-As bonds are identical and the tetrahedral symmetry is preserved at the In atom. We regard any difference between Ga and In as a first-order difference. Let us call d_{GaAs} the natural bond length of the host and K the stretching force constant for the host. Adding In will change K by an amount we regard as first order, but that alone will not give the distortion. However, because the natural bond length of InAs, d_{InAs} , is larger than d_{GaAs} by a first-order amount the As atoms around the In impurity move outward by a first-order distance; we hold the second neighbors fixed and to first order can take K to be the value for the host. Let us call u the outward relaxation displacement of the As. Then Δd_{InAs} , the amount that the final In-As bond length deviates from d_{InAs} , is $d_{\text{GaAs}} - d_{\text{InAs}} + u$. The bond lengths of the neighboring Ga-As are decreased by $-u \cos \theta$ equal to $-u/3$ to first order. The energy associated with the distortion is

$$E = 4[(k/2)(d_{\text{GaAs}} - d_{\text{InAs}} + u)^2 + 3(k/2)(u/3)^2].$$

By minimizing the energy with respect to u , we obtain

$$u = \frac{1}{4}(d_{\text{InAs}} - d_{\text{GaAs}}).$$

or the deviation of the In-As bond length

$$\Delta d_{\text{InAs}} = \frac{1}{4}(d_{\text{GaAs}} - d_{\text{InAs}}).$$

Similarly, the bond-length deviation of dilute Ga-As in an InAs host is

$$\Delta d_{\text{GaAs}} = \frac{1}{4}(d_{\text{InAs}} - d_{\text{GaAs}}).$$

This predicts exactly Mikkelsen and Boyce's result.¹ Note that this displacement leaves all metallic atoms in their original sites; only the As atoms move. To a good approximation this is true in the concentrated alloy, where the metal atoms form a face-centered-cubic lattice of the weighted average lattice parameter and the As atoms move to fit local bond lengths.

One can apply this principle to the rocksalt-structure systems, e.g., $\text{K}_{1-x}\text{Rb}_x\text{Br}$, and predict that the bond-length deviation of the solute in the dilute solution is half of the

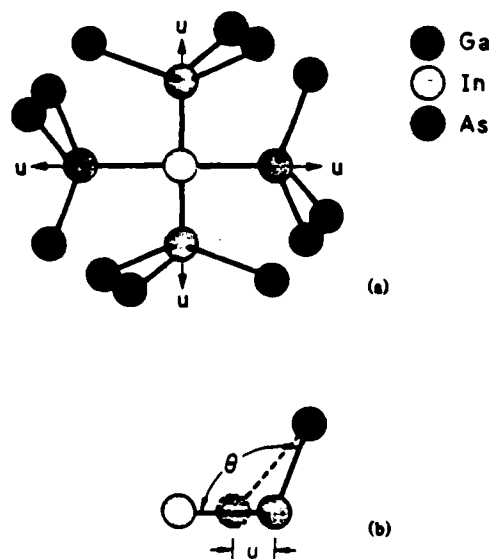


FIG. 1. (a) An indium atom substitutes for gallium in GaAs; the tetrahedral symmetry is preserved at the In atom. (b) The displacement of As atoms, u , results in the Ga-As bonds being decreased by $u \cos \theta$. The In-As bond lengths are varied by $d_{\text{GaAs}} + u - d_{\text{InAs}}$.

difference between the two components:

$$\Delta d_{KBr} = \frac{1}{2}(d_{RbBr} - d_{KBr}) ,$$

$$\Delta d_{RbBr} = \frac{1}{2}(d_{KBr} - d_{RbBr}) .$$

However, because of the lattice geometry, the approximation that all the cations stay in their original sites might not be as good. In rocksalt structure, the restoring force on the displaced first neighbor results from the atom right behind

the first neighbor; one would expect that the relaxation extends more than one interatomic distance and the value of the bond-length deviation would be somewhat smaller than what is predicted by this model. This agrees with the experimental result.^{2,4}

We thank Dr. Alex Zunger for valuable discussions. This work was supported by the Defense Advanced Research Projects Agency under Contract No. 800989-B8

¹J. C. Mikkelsen, Jr. and J. B. Boyce, Phys. Rev. B 28, 7130 (1983).

²J. B. Boyce and J. C. Mikkelsen, Jr., Bull. Am. Phys. Soc. 29, 271 (1984)

Binding Energy and Spectral Width of Si 2p Core Excitons in $\text{Si}_x\text{Ge}_{1-x}$ Alloys

S. Krishnamurthy and A. Sher

Physical Electronics Laboratory, SRI International, Menlo Park, California 94025

and

A.-B. Chen^(a)

Department of Physics, Auburn University, Auburn, Alabama 36849

(Received 24 January 1985)

A calculation is presented to explain the anomalous experimental behavior of the Si 2p core-exciton binding energy and linewidth in $\text{Si}_x\text{Ge}_{1-x}$ alloys. The observed minimum in the linewidth near $x \approx 0.15$ can be explained as the result of a competition between intrinsic broadening due to screening and extrinsic alloy broadening. For pure Si, the binding energy is estimated to be 0.15 ± 0.05 eV and the width is shown to be smaller than that observed at $x \approx 0.15$.

PACS numbers: 71.55.Fr, 71.35.+z, 78.70.Dm

Until 1984, the Si 2p core exciton was believed to have an anomalously large binding energy.¹⁻¹⁰ Later, Newman and Dow¹¹ proposed a radically different picture in which the Si 2p core exciton is in fact a resonance with a negative binding energy. They further predicted that the exciton binding energy remains negative throughout most of the $\text{Si}_x\text{Ge}_{1-x}$ alloy composition range, except near $x \approx 0.20$ where it becomes positive. In a recent experiment,¹² Bunker *et al.* found an anomalous sharpening of the exciton spectra near $x = 0.15$; the data were interpreted to support the Newman-Dow point of view. Yet the most recent experiment¹³ still suggests a positive value for the binding energy E_b^0 in silicon.

In this Letter, we present a calculation that offers a plausible resolution to the above problem. In our theory, the calculated Si 2p core-exciton binding energy $E_b(x)$ and the linewidth $\Delta(x)$ in $\text{Si}_x\text{Ge}_{1-x}$ alloys are sensitively dependent on the parameter E_b^0 . A comparison of the calculated $\Delta(x)$ with the experiment¹² suggests a positive value 0.15 ± 0.05 for E_b^0 . The anomalous experimental spectrum¹² near $x \approx 0.15$ is explained as a result of a competition between an intrinsic broadening Δ_i due to screening and an extrinsic alloy broadening Δ_A . In the present theory, there is no need to suppose that the exciton suddenly changes its character from an extended effective-mass-like state to a deep localized state.

We need to calculate E_b and $\Delta = \Delta_i + \Delta_A$ as a function of alloy concentration x . The calculations are based on a quantitative coherent-potential-approximation (CPA) band structure. Details of the CPA calculations will be presented elsewhere. Below, we briefly discuss a Green's-function method for calculating E_b and Δ_A .

The one-particle effective Green's function in CPA takes the form

$$G(E) = [E - \bar{H} - \Sigma(E)]^{-1}, \quad (1)$$

where \bar{H} is the virtual-crystal approximation Hamil-

tonian and $\Sigma(E)$ is the self-energy. The site-diagonal Green's function is denoted as

$$F_\alpha(E) = \langle \phi_\alpha | G(E) | \phi_\alpha \rangle, \quad (2)$$

where ϕ_α is a localized orbital of specified symmetry. Here we only need to consider $\alpha = s$ for A_1 symmetry. The corresponding function in pure Si is denoted as $F_s^0(E)$. Following the theoretical treatment of deep substitutional-impurity levels,⁸ the core-exciton level for pure Si is determined by

$$F_s^0(E) = (V - E_s^{\text{Si}})^{-1}, \quad (3)$$

where E_s^{Si} is the site potential seen by an s electron in bulk silicon, and V is a central-potential parameter. For a chosen value of V , Eq. (3) can be solved for E , and vice versa. Then $E_b^0 = E_c^0 - E$, where E_c^0 is the conduction-band edge in pure silicon. Because of the uncertainties in the value of experimental E_b^0 and theoretical V , we treat E_b^0 (or V) as a parameter. The binding energy E_b in a $\text{Si}_x\text{Ge}_{1-x}$ alloy can be calculated by solving

$$F_s(E) = [V - \bar{E}_s - \Sigma_s(E)]^{-1}, \quad (4)$$

where

$$\bar{E}_s = xE_s^{\text{Si}} + (1-x)E_s^{\text{Ge}}. \quad (5)$$

Then E_b is given by

$$E_b = E_c - E. \quad (6)$$

The calculated values of the conduction-band edge and the exciton level measured relative to the top of the valence band are plotted in Fig. 1. The band gap increases with x with a slope discontinuity at ≈ 0.15 . The dashed lines a , b , and c represent exciton levels obtained with $E_b^0 = 0.1, 0.15$, and 0.30 eV, respectively. The binding energy E_b is also an increasing function of x , with a slope discontinuity near $x \approx 0.15$. The CPA introduces a slight bowing in E_c and E_b .

Strinati¹⁰ has calculated the variation of Δ_i with E_b

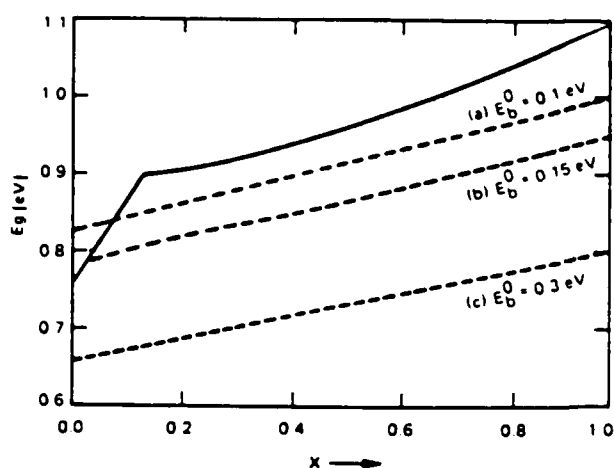


FIG. 1. Variation of the band gap (solid line) and the Si 2p core-exciton level with x in $\text{Si}_x\text{Ge}_{1-x}$ alloys. The energy is measured from the top of the valence band. The dashed curves a, b, and c represent exciton levels calculated with $E_b^0 = 0.1, 0.15$, and 0.3 eV, respectively.

by replacing the short-range Coulomb potential with a spherical square well of variable depth and a screened Coulomb tail. Strinati's results can be used to estimate Δ_I corresponding to the calculated E_b . Δ_I decreases rapidly with E_b , then saturates for larger E_b .

The contribution to the natural linewidth from the alloy broadening is calculated by a consideration of the electron part of the exciton wave function, ψ_s . The ψ_s is expanded in a linear combination of the s part of the conduction-band wave functions ϕ_n^s :

$$\psi_s(\mathbf{k}) = \sum_{n,s} C_{ns} \phi_n^s(\mathbf{k}). \quad (7)$$

We found that alloy scattering is only moderate and s scattering is dominant; thus, the alloy broadening $\Delta_A(E)$ is well approximated by

$$\Delta_A(E) \approx x(1-x)\delta_s^2 \text{Im}F_s(E), \quad (8)$$

where δ_s is the difference between E_s^{Si} and E_s^{Ge} . Hence, the alloy-broadening contribution to Δ is related to the alloy broadening of the band states, $\Delta_n(\mathbf{k}, E)$:

$$\begin{aligned} \Delta_A &= \frac{1}{N} \sum_{\mathbf{k}} \langle \psi_s(\mathbf{k}) | \Delta_A(E) | \psi_s(\mathbf{k}) \rangle \\ &\approx \frac{1}{V} \sum_{\mathbf{k}} \sum_n C_{ns}^2 \Delta_n(\mathbf{k}, E) \\ &= \int \rho_s(E) \Delta_A(E) dE \\ &= x(1-x)\delta_s^2 \pi \int \rho_s^2(E) dE. \end{aligned} \quad (9)$$

The integral in Eq. (9) is evaluated numerically

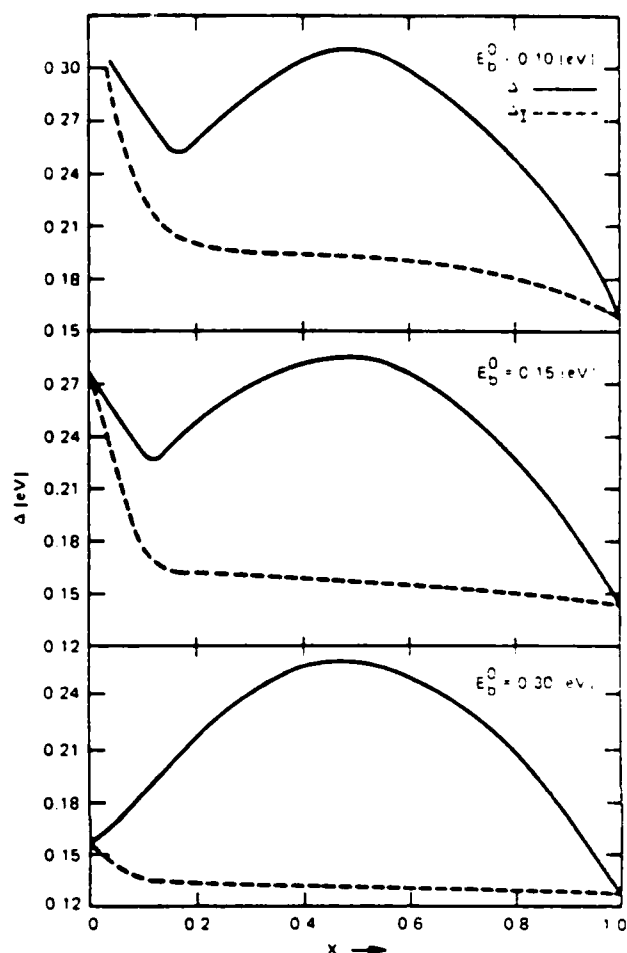


FIG. 2. Variation of Δ (solid lines) and Δ_I (dashed lines) with x for three E_b^0 values.

The calculated Δ , which is the sum of Δ_I and Δ_A , is plotted against x in Fig. 2 for three values of E_b^0 . In all three panels, the dashed curve represents Δ_I and the solid line represents Δ . It is seen from Fig. 1 that the exciton level follows the X edge of the conduction band. Hence the binding energy E_b , relative to the conduction band edge, remains almost constant (for a given E_b^0) until the minimum switches from the X edge to the L edge. Because of the change in the slope of E_g , E_b decreases rapidly when L becomes the minimum. Correspondingly, Δ_I varies slowly until the X to L crossover and then increases rapidly. This feature is clearly seen in Fig. 2.

For $E_b^0 = 0.15$, the Δ_I and Δ_A are comparable near $x = 0.50$, and Δ_I dominates for all small x and large x . These two competing mechanisms give a relative minimum near $x \approx 0.15$, a broader maximum near $x \approx 0.50$, and a smaller minimum for pure silicon. As E_b^0 is decreased, the relative minimum is shifted to larger x , e.g., the minimum shifts to $x = 0.20$ for $E_b^0 = 0.10$ eV. For $E_b^0 = 0.15$ eV, the position of the

relative minimum is in agreement with the experiment.¹² (By measuring the relative width at $x \approx 0.15$ to that at $x = 1$, one can make a better estimate of E_b^0 .) To correlate the theory with experiment, the calculated $1/\Delta^2$ is compared with the measured¹² $(\Delta\mu)^{-1}(d\mu/dE)_{\max}$ in Fig. 3, where $\Delta\mu$ is the edge step and $(d\mu/dE)_{\max}$ are the maximum values of the derivative of absorption spectra with respect to photon energy. Because the experimental values are given in arbitrary units, the values are normalized to agree at $x = 0.5$. The observed anomalous behavior near $x = 0.15$ and the qualitative x dependence in that region is clearly replicated by the theory. However, the calculation predicts a larger maximum at $x = 1$. It would be interesting to have experiments that cover the entire range of x to further test this prediction.

For larger values of E_b^0 , the calculated E_b is also large and hence Δ_i decreases slowly with x . Because the broadening is determined mainly by Δ_A , the linewidth is expected to be small for $x = 0$ and $x = 1$ only; this occurs for $E_b^0 = 0.30$ eV. For negative values of E_b^0 , E_b remains negative for all values of x . Accordingly, the linewidth is broad for all x , and there would be no such anomaly as in Fig. 3.

The calculations presented in this Letter are slightly different from alchemy approximations.⁸ We treat the central-cell potential V as a parameter and narrow its range from other considerations. We examine values of $V - E_j^{\text{Si}}$ of -8.49 , -7.09 , and -6.56 eV, corresponding to E_b^0 values of 0.30 , 0.15 , and 0.10 eV, respectively. If the strict alchemy approximation were taken, the value of $V - E_j^{\text{Si}}$ would be $E_j^{\text{P}} - E_j^{\text{Si}} = -4.59$ eV in the tight-binding approximation, and a negative

E_b^0 (~ -0.10 eV) would be obtained. When long-range interactions are included, however, the above resonance state becomes a shallow donor level, which is the experimental situation for a P impurity in Si. Our results suggest that V for core excitons in Si is deeper than those implied by alchemy approximations. However, if we use the alchemy approximation as a means of scaling, the value of V for Ge $3p$ core excitons should be deeper than that for Si $2p$ core excitons. Hence, the curve corresponding to $E_b^0 = 0.30$ in Fig. 2 should be a reasonable estimate for Ge $3p$ core-exciton binding energy in alloys. Therefore, we do not expect to see an anomalous behavior of Δ in alloys for this case.

In summary, the present calculations of the Si $2p$ core-exciton binding energy and linewidth suggest that the exciton level is about 0.15 ± 0.05 eV below the conduction-band edge for pure Si. It follows the X edge for $x > 0.15$ in the $\text{Si}_x\text{Ge}_{1-x}$ alloys, and E_b may eventually reach zero in the dilute limit $x \rightarrow 0$. Our value for E_b^0 represents the lower end of the previous measurements,¹⁻⁶ but is in good agreement with a recent experimental¹³ value of 0.120 ± 0.03 eV. By considering the intrinsic linewidth and the alloy broadening, we can explain the observed relative minimum in the linewidth near $x \approx 0.15$, without requiring a sudden change of the exciton character. On the basis of this calculation, we expect the corresponding width in pure Si to be even smaller than that observed near $x = 0.15$. We further argue that the binding energy of Ge $3p$ core excitons should be larger than that of Si $2p$ core excitons and there should be no anomaly in the Ge $3p$ linewidth in alloys.

This work was supported in part by the U.S. Department of Defense Advanced Research Projects Agency, under Contract No. MDA 903-83-C-0108 and the Air Force Office of Science Research through Grant No. AFOSR-84-0282. One of us (A.-B.C.) would like to thank Professor W. E. Spicer for his hospitality at Stanford University.

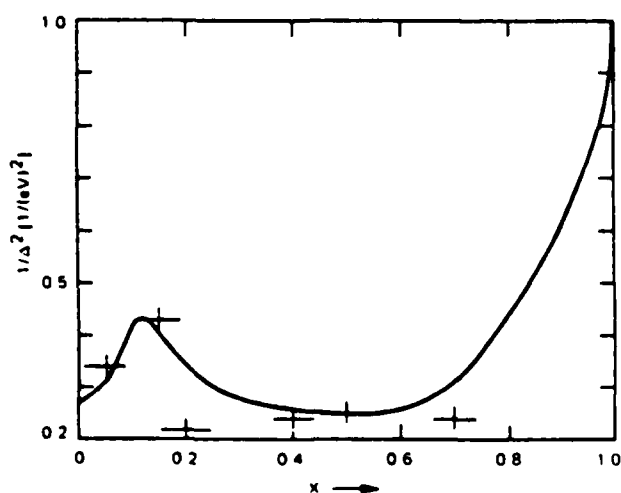


FIG. 3 The calculated $1/\Delta^2$ values (solid line) compared with the experimental results (marks) from Ref. 12. The value of calculated $\Delta(\text{Si})$ is 0.127 eV. The experiment is normalized to the theory at $x = 0.5$.

(a) Visiting professor at Stanford University

¹W. Eberhardt, G. Kalkoffen, C. Kunz, D. E. Aspnes, and M. Cardona, *Phys. Status Solidi* (b) **88**, 135 (1978)

²M. Altarelli and D. L. Dexter, *Phys. Rev. Lett.* **29**, 1100 (1972).

³F. C. Brown, R. S. Bachrach, and M. Skibowski, *Phys. Rev. B* **15**, 4781 (1977).

⁴R. S. Bauer, R. S. Bachrach, J. C. McMenamin, and D. E. Aspnes, *Nuovo Cimento* **39B**, 409 (1977).

⁵G. Margaritondo and J. E. Rowe, *Phys. Lett.* **59A**, 464 (1977).

⁶G. Margaritondo, A. Franciosi, N. G. Stoffel, and H. S.

Edelman, Solid State Commun. **36**, 298 (1980)

⁷C. Kunz, J. Phys. (Paris), Colloq. **39**, C4-119 (1978)

⁸H. P. Hjalmarson, H. Büttner, and J. D. Dow, Phys. Rev. B **24**, 6010 (1981).

⁹M. Altarelli, Phys. Rev. Lett. **46**, 205 (1981).

¹⁰G. Strinati, Phys. Rev. Lett. **49**, 1519 (1982).

¹¹K. E. Newman and J. D. Dow, Solid State Commun. **50**, 587 (1984)

¹²B. A. Bunker, S. L. Hulbert, J. P. Stoll, and F. C. Brown, Phys. Rev. Lett. **53**, 2157 (1984)

¹³S. E. Schnatterly and R. D. Carson, Bull. Am. Phys. Soc. **30**, 416 (1985)

CORRELATIONS IN PSEUDOBINARY ALLOYS

Arden Sher
SRI International, Menlo Park, CA 94025

An-Ban Chen
Department of Physics, Auburn University, AL. 36849

Mark van Schilfgaarde
SRI International, Menlo Park, CA 94025

Abstract

Correlations between atoms of Cd and Zn in $\text{Cd}_{1-x}\text{Zn}_x\text{Te}$ and Hg and Zn in $\text{Hg}_{1-x}\text{Zn}_x\text{Te}$ are calculated within an extended quasichemical approximation. A tetrahedron of alloy atoms is used for the microcluster unit. The statistical mechanics of the correlations is outlined for the present problem, an approximate method of solution is indicated. Microcluster energies are obtained from an approximation of a Keating model due to Martin, plus a correction due to Harrison to account for the coupling between the tetrahedral bonds.

It is found that the correlations are significant at typical growth temperatures (300-600K). $\text{Hg}_{1-x}\text{Zn}_x\text{Te}$ is predicted to undergo spinoidal decomposition between 300K and 600K.

Introduction

We present here a preliminary investigation of the statistical mechanics of multiatom correlations (microclusters) in pseudobinary alloys $A_{1-x}B_xC$ of tetrahedral semiconductors. Thermodynamic equilibrium is a balance between entropic forces, which favors random site occupation of the pseudobinary elements, and more energetically favorable ordered configurations. Below a critical temperature, the equilibrium state is a generally an ordered state, spinoidal decomposition for positive values of the mixing enthalpy, or compound formation for negative values. For growth temperature above the critical temperature the alloy may still exhibit correlations, which vanish in the infinite temperature limit.

With suitable approximations this alloy problem is isomorphic to the well-known Ising model, a notoriously difficult problem to solve. Since a rigorous treatment of correlations between units is intractable, we make here a *quasichemical* approximation and treat the alloy as composed of microclusters of several atoms embedded in an effective medium, which is tantamount to neglecting correlations among microclusters. The problem reduces to the original one in the limit of large microcluster size; in general the errors introduced by neglecting coupling between microclusters should not be of great importance well above the phase transition temperature. This model is clearly inappropriate at or below a critical temperature, but should give a reasonable indication of the short range correlations provided the correlation lengths do not exceed the microcluster size.

Microcluster Hamiltonian

Tetrahedron as a Microcluster Unit

If the microcluster has only pair interactions, the free energy must be

- 2 -

symmetric in x and $1-x$. For that reason we will work with a larger unit and choose the tetrahedral unit shown in Fig. 1 for the microcluster. It is the natural unit for calculating corrections to pair interactions, and is also compact. In tetrahedral solids the strains associated with an impurity tend to be short ranged; thus the tetrahedron will emphasize the most important differences between the various configurations. The microcluster is taken to be embedded in an effective (virtual crystal) medium.

A microcluster of two alloy atoms corresponds to the Bethe-Pierls approximation [1] in the Ising model analogue. The quasichemical approximation used here is comparable to it, though somewhat better (as larger microcluster sizes are taken) to that approximation.

Force Constant Model

Harrison [2] has shown that the cohesive energy in a tetrahedral crystal derives mainly from nearly independent bonds that only weakly couple to their environment, and that the variation in the bond energy depends mainly on the bond length, with rather weak dependences on the constituent atoms or the environment of the bond. *Metallization*, the relatively small coupling of the bond to neighboring bonds Harrison calculates in perturbation theory. This implies that the electronic structure contributing to the bonding is quite short-ranged. Long range interactions arising from the electronic structure (apart from the Madelung terms) can be estimated [3]; they decay exponentially with internuclear distance and are too small to be of significance here.

We use these findings as a justification for constructing a force constant model in which the bonds are treated nearly independently and the cohesive energy in the alloy differs from the virtual crystal approximation (VCA) partly through strains of bonds stretched or bond angles bent from their "natural" positions.

Indeed, such a model can be derived from a tight-binding theory [4] in that theory in the only additional corrections are the changes in metallization in the microclusters relative to those in the VCA. These corrections, called previously by us [5] the "chemical" energy, are also included here. It is this coupling that gives rise to departures from the pair interactions and asymmetries in the dependence of the free energy on composition. In the heavier elements the chemical energy can be quite significant, and can approach the order of the strain energies. Following our earlier work we will use a Keating model [6], neglecting the Madelung contributions to the force contents. This model is essentially similar to that of Sokel [4], except that we fit the force constants to experimental data.

Strain Energies in an Effective Medium

A microcluster differs in size and shape from the effective medium surrounding it, and so displaces all of the surrounding atoms so as to minimize the total strain energy. (The chemical energy does not depend strongly on the strains and can be ignored when calculating the strain energy.) In the approximations made here the entire effective medium is characterized in terms of the bonds connecting the microcluster to its twelve surrounding second neighbors. Each second neighbor couples to the adjacent microcluster atom with effective force constants K_r and K_t for strains parallel and perpendicular to the second-neighbor bond, respectively. Further reduction in the strain energy through displacement of more distant neighbors enters here as a modification of K_r and K_t . So far this is merely a recasting of the Keating model, since the interaction with the second neighbors can obviously be represented in terms of effective force constants; the approximations lie in our choice for K_r and K_t . It is implicitly assumed that the 24 force constants K are independent of each other. Because displacements of more distant neighbors fall off rapidly away from an impurity, the coupling between the different force constants is

indeed quite small, and errors introduced by this assumption should not be serious in comparison to errors inherent in the effective medium approximation.

To guide us to a suitable model for K_r and K_t , we use for the present purposes the Shih approximation [7] for the strain energy outside the microcluster itself. Using a force constant model, Shih *et al* calculated the bond length of a single impurity in a host crystal, holding the second neighbors fixed and neglecting the smaller angular forces. One might intuitively expect that the distortion about an impurity is quite well localized in tetrahedral solids, since the impurity-second neighbor bond angles are quite large. One would expect this to be far less the case if atoms were arranged collinearly as they are in the alkali halides, for example. In tetrahedral solids a displacement along the impurity-nearest neighbor axis has only a small component along the neighbor-second neighbor axis, and the distortion tends to damp out rapidly as the angular forces are weak. The simple model of Shih *et al* predicts that the nearest neighbor displaces so as to accommodate 3/4 of the strain in the impurity bond. This is in excellent agreement with experimental data [8], and provides *post facto* justification for the argument that distortions are reasonably well localized. Subsequent analysis by ourselves [5] has shown that the weak angular forces and the relaxation of more distant neighbors make corrections to this that nearly cancel. The Shih approximation also predicts reasonable mixing enthalpies. Thus, for the present analysis we use the Shih approximation to calculate the effective force constants K_r and K_t .

The Shih approximation predicts

$$K_r = \frac{3}{4}\alpha$$

where α is a Keating force constant to be defined below, and

$$K_t = 0$$

because it neglects angular forces. One might worry that the latter approximation is

unrealistic, but a detailed analysis [9] shows that it only makes a small contribution ($\sim 3\%$) to the total strain energy.

Microcluster Energies in an Effective Medium

Following our earlier work [5], strain energies are calculated from the Keating model

$$E_{\text{strain}} = \frac{3}{8d^2} \left[\alpha \sum_i \delta^2 \mathbf{r}_i \cdot \mathbf{r}_i + \beta \sum_{ij, i>j} \delta^2 \mathbf{r}_i \cdot \mathbf{r}_j \right]. \quad (1)$$

δ^2 above signifies the square of the difference in the dot product relative to the unstrained value. The α terms are two-body (radial) forces and the β terms are three-body (angular) forces, and are typically $5-10\times$ smaller than the α terms.

The total strain energy is thus formulated as the sum of strains internal to the microcluster, which we calculate from the Keating model, the three-body β strain energies connecting the microcluster to the adjacent effective medium atoms, and the strain energy from the effective medium,

$$\frac{1}{2} K_r \sum_{ij} (\hat{\mathbf{d}}_{ij} \cdot \delta \mathbf{r}_j)^2 \quad (2)$$

where the index i signifies each of the three external bonds adjacent to microcluster atom j .

The strain energy must be minimized with respect to the various possible distortions of the microcluster. To this is added the chemical terms [5] for the total energy. The two can be reasonably treated separately since the chemical terms do not depend strongly on bond lengths, and thus do not modify the distortions significantly.

From symmetry considerations the A_4 and B_4 microclusters have only the breathing mode shown in Fig. 2a, in which every A atom displaces radially by an

equal amount. The resulting strain energies for the A_4 and B_4 microclusters can be written

$$\begin{aligned} E_{A_4} &= E_{4,\text{strain}} = C_4 \delta_A^2 & \text{and} \\ E_{B_4} &= E_{0,\text{strain}} = C_4 \delta_B^2, & \text{where} \end{aligned} \quad (3)$$

$$\begin{aligned} \delta_A &= (\bar{d} - d_A)/\bar{d} & \text{and} \\ \delta_B &= (\bar{d} - d_B)/\bar{d} \end{aligned} \quad (4)$$

are the fractional differences in bond lengths of the pure crystals A and B relative to that of the virtual crystal. The A_2B_2 microcluster has five independent distortions u_j , where the u_j represent some linear combination of the displacements of the microcluster atoms. With judicious selection of the linear combinations, the stress matrix $\nabla_{u_i} \nabla_{u_j} E_{\text{strain}}$ can be made block diagonal with two of the distortions corresponding to the same breathing mode as in A_4 , and the remaining three corresponding to an internal strain shown in Fig. 2b. The microcluster strain energy takes the form

$$E_{A_2B_2} = E_{2,\text{strain}} = C_4 \left(\frac{\delta_A + \delta_B}{2} \right)^2 + C_2 \left(\frac{\delta_A - \delta_B}{2} \right)^2. \quad (5)$$

The A_3B and AB_3 microclusters have four independent distortions, but again a breathing mode can be block diagonalized with the strain energy taking the form

$$E_{AB_3} = E_{1,\text{strain}} = C_4 \left(\frac{\delta_A + 3\delta_B}{4} \right)^2 + \frac{3}{4} C_2 \left(\frac{\delta_A - \delta_B}{2} \right)^2 \quad (6)$$

with a similar expression for E_3 . C_4 and C_2 depend on the choice of model taken for the K_r and K_t . We use the Shih approximation described earlier for their calculation.

The total energy for microcluster j is then

$$E_j = E_{j,\text{strain}} + E_{j,\text{chem}} \quad (7)$$

The chemical energy is calculated as in our previous work [5]. Since only the differences in microcluster energies are relevant, it is convenient to define linear

combination of the E_j :

$$\Delta_j = E_j - \frac{1}{4}[j E_4 + (4-j) E_0]. \quad (8)$$

By definition Δ_0 and Δ_4 are 0.

Statistics of Correlations

The entropy is obtained from the number of ways to configure the alloy for a given energy. Since the microclusters are assumed to be independent, the energy of a configuration is specified by the number of each kind of microcluster. For the present work it is assumed that the surrounding medium has cubic symmetry, so that the microcluster energy depends only on the number of A (or B) atoms it contains. We distinguish each kind of microcluster with an index j , which can be taken in this symmetric case as the number of A atoms in the microcluster, so that j ranges from 0 to $n=4$. We define g_j is the number of distinguishable ways of rotating microcluster j on the same site, i.e. $g_j = 1, 4, 6, 4$ and 1 for $j = 0, 1, 2, 3$ and 4. If an external shear is imposed these energies are not degenerate, in which case it would be necessary to treat each orientation separately.

The entropy, the logarithm of the number of ways to configure a system with M_j microclusters of type j , is difficult to calculate precisely. We use here the approximate formula [10]

$$S = k \ln \frac{N!}{N_A! N_B!} \left[\frac{M!}{\prod_j M_j!} \prod_j (x_j^0)^{M_j} \right] \quad (9)$$

where N_A and N_B are the number of A and B atoms, respectively, with the number of unit cells $N = N_A + N_B$ and the number of clusters $M = \sum_j M_j$, which for this problem, $M = N$. The products over j range from 0 to $n=4$. Finally

$$x_j^0 = g_j x^j (1-x)^{n-j} \quad (10)$$

is the probability of finding microcluster j in a random alloy. The expression in brackets in Eqn. 9 is the probability of finding M_0, M_1, \dots, M_4 microclusters in the random alloy out of all the possible configurations of microclusters. The probabilities x_j^0 of finding microcluster j are assumed to be independent.

The microcluster energies Δ_j , Eqns. 8, and the entropy Eqn. 9 completely specify the equilibrium statistical mechanics of the alloy. With Stirling's approximation, the mixing free energy is

$$\delta F = M \left[(1-x)(E_4 - E_4^0) + x(E_0 - E_0^0) \right] + NkT[x \ln x + (1-x) \ln(1-x)] + M \sum_j x_j \Delta_j + kT \sum_j x_j \ln(x_j/x_j^0) \quad (11)$$

The meaning of E_4^0 and E_0^0 are the cluster energies in a pure A and B materials respectively: $(1-x)E_4^0 + xE_0^0$ is the VCA alloy energy. The equilibrium energy is the minimum with respect to the microcluster concentrations x_j , leading to five simultaneous equations subject to the constraints

$$\begin{aligned} (1-x)n &= \sum_j j x_j \text{ and} \\ 1 &= \sum_j x_j \end{aligned} \quad (12)$$

Using the method of steepest descents, these equations may be collapsed [9] into a single equation for an effective activity coefficient η . Once η is obtained, the microcluster concentrations are calculated from

$$x_j = \frac{1}{Z} \eta^j g_j e^{-\Delta_j/kT} \quad (13)$$

where Z is the partition function

$$Z = \sum_j \eta^j g_j e^{-\Delta_j/kT} \quad (14)$$

The mixing free energy becomes

$$\delta F = N \left[(1-x)(E_4 - E_4^0) + x(E_0 - E_0^0) \right] + NkT[(1-n)(x \ln x + (1-x) \ln(1-x)) + nx \ln \eta - \ln Z] \quad (15)$$

Results

Figs. 3 show the microcluster energies as a function of composition for the alloys $\text{Cd}_{1-x}\text{Zn}_x\text{Te}$ and $\text{Hg}_{1-x}\text{Zn}_x\text{Te}$. The asymmetries in those curves result from the chemical terms, and the asymmetry at the extremes of alloy composition give a rough measure of their importance relative to the strain energy. Near the extremes of the composition range, the microcluster energies increase roughly in proportion to the number of minority species present. Near the 50% composition, however, the Cd_2Zn_2 composition has very little excess energy, reflecting the fact that it nearly fits into the effective medium, while the Cd_4 and Zn_4 microclusters must contract and expand respectively, to fit into the room available. For the same reason, *mutatis mutandis*, ZnCd_3 and Zn_3Cd show the smallest energies near the 25% and 75% compositions, respectively.

Figs 4 and 5 show the difference in expectation values of microcluster populations relative to their random-alloy values at $T=300\text{K}$ and 1500K , respectively. These figures show strong deviations from randomness at low temperature, and significant ones at high temperature. Microclusters having least strain energy show greatest gains in population, following closely the rule mentioned above for the microcluster energies.

The free energies of mixing are shown in Figs 6. At high temperature, the mixing energy is nearly symmetric and rather strongly negative, reflecting the dominance of entropy terms. At 300K some finer structure in the $\text{Cd}_{1-x}\text{Zn}_x\text{Te}$ is in clear evidence, reflecting a tendency toward spinoidal decomposition. The same tendencies are present, and more pronounced in $\text{Hg}_{1-x}\text{Zn}_x\text{Te}$. The free energy is less at the extremes of alloy composition in Figs. 6 than throughout most all of the composition range, thus predicting that a phase transition towards spinoidal decomposition occurs in $\text{Hg}_{1-x}\text{Zn}_x\text{Te}$ between 300K and 600K .

Synopsis

The calculation of correlations in pseudobinary alloys is outlined within a quasichemical approximation, using tetrahedra of alloy atoms for the microcluster unit. Using a Keating model with corrections for coupling between the bonds, the energies of the various tetrahedral microclusters are calculated for $\text{Cd}_{1-x}\text{Zn}_x\text{Te}$ and $\text{Hg}_{1-x}\text{Zn}_x\text{Te}$. The correlations are found to be significant in both systems, particularly in $\text{Hg}_{1-x}\text{Zn}_x\text{Te}$. A phase transition to spinoidal decomposition is predicted for that system between 300K and 600K.

Acknowledgments

We wish to help Professor W. E. Spicer for helpful suggestions.

This work was supported in part by U.S. Airforce Office of Scientific Research Contract No. AFOSR-84-0284 and U.S. Defense Advanced Research Projects Agency DARPA Contract No. MDA-903-83-C-0108.

Figure Captions

Fig. 1. (a) Tetrahedral unit of four alloy atoms (●) surrounding the central atom (○). The unit is embedded in an effective medium, coupled to twelve second neighbors (○) with effective force constants K_r and K_t as described in the text. The four alloy atoms can be one of A_4 , AB_3 , A_2B_2 , A_3B or B_4 . (b) the external unit connecting to the cluster atom (●) in the present model. Using the Shih approximation the bottom three atoms are assumed not to move.

Fig. 2. Distortions of a tetrahedron. (a) breathing mode distortion of A_4 and also in the other microclusters as described in the text. (b) distortion in A_2B_2 corresponding to bond length differences $\delta_A - \delta_B$. There are three independent distortions: a radial distortion along the bond axes, a distortion transverse to the bond axes, and the displacement of the central C atom. (c) distortion in A_3B or AB_3 corresponding to bond length differences $\delta_A - \delta_B$. There are three independent distortions here as well: a uniform translation of all atoms in the microcluster (not shown), the displacement of the central atom, and the displacement of the three A (or B) atoms transverse to the bond axis.

Fig. 3. Microcluster energies as a function of composition in (a) $Cd_{1-x}Zn_xTe$ and (b) $Hg_{1-x}Zn_xTe$.

Fig. 4. Microcluster populations relative to the random alloy value in $Cd_{1-x}Zn_xTe$ at (a) 300K and (b) 1500K.

Fig. 5. Microcluster populations relative to the random alloy value in $Hg_{1-x}Zn_xTe$ at (a) 300K and (b) 1500K.

Fig. 6. Mixing free energies as a function of composition in (a) $Cd_{1-x}Zn_xTe$ and (b) $Hg_{1-x}Zn_xTe$.

References

1. E. A. Guggenheim, *Mixtures*, (Oxford University Press, London, 1952), pp 136ff.
2. W. A. Harrison, *Phys. Rev.* **B27**, 3592 (1983) and references therein.
3. R. Sokel and W. A. Harrison *Phys. Rev. Lett.* **36**, 61 (1976).
4. R. Sokel, *Bull. Am. Physical Society* **B21**, 1315 (1976). See also his PhD thesis, Stanford University (1978).
5. A. B. Chen and A. Sher *Phys. Rev.* **B32**, 3695 (1985).
6. R. M. Martin, *Phys. Rev.* **B10**, 4005 (1970).
7. C. K. Shih, W. E. Spicer, W. A. Harrison and A. Sher, *Phys. Rev.* **B31**, 1139 (1985).
8. J. C. Mikkelsen and J. B. Boyce, *Phys. Rev.* **B28**, 7130 (1983).
9. A. B. Chen, A. Sher and M. van Schilfsgaarde, to be published.
10. We are indebted to William Chen for suggesting this expression to us.

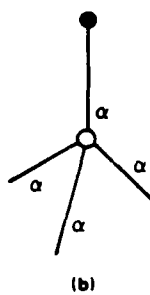
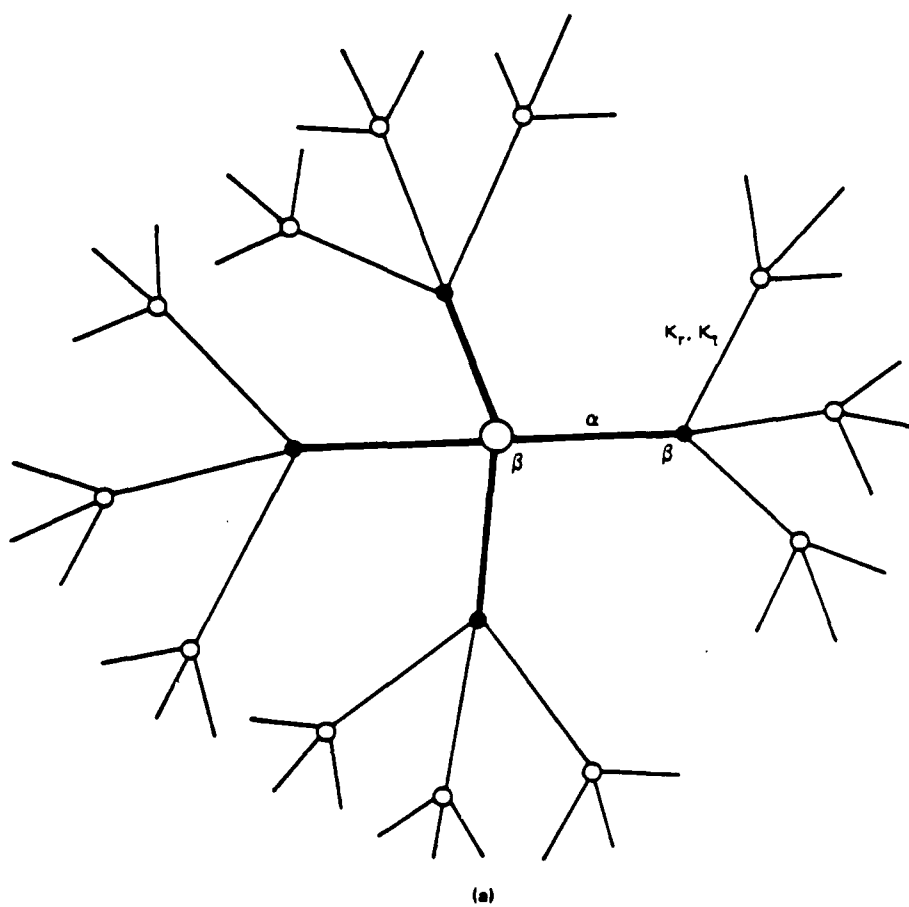
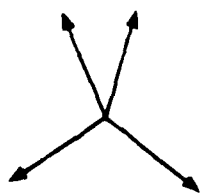
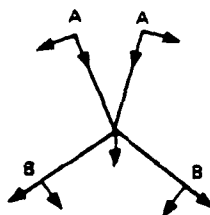


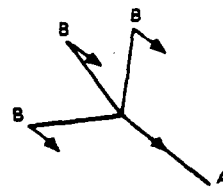
FIGURE 1



(a)



(b)



(c)

FIGURE 2

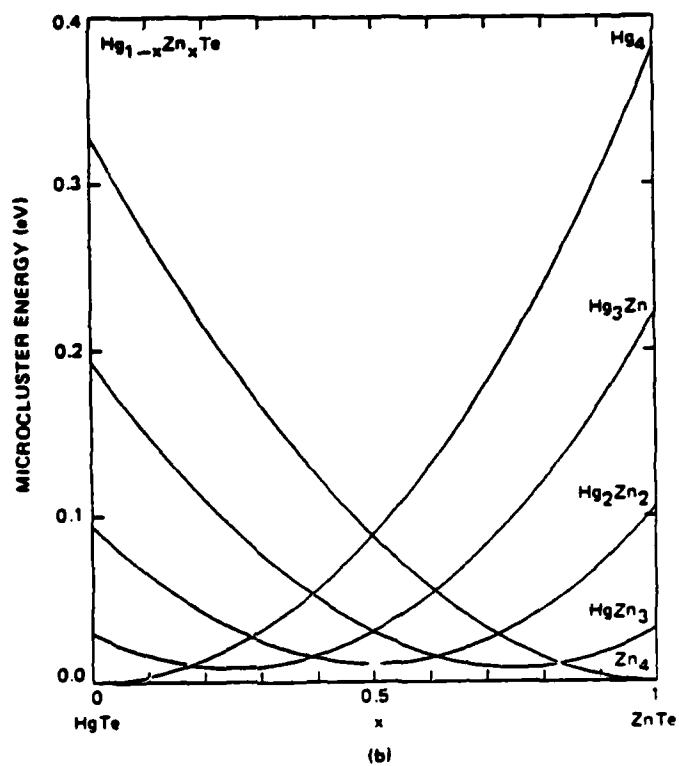
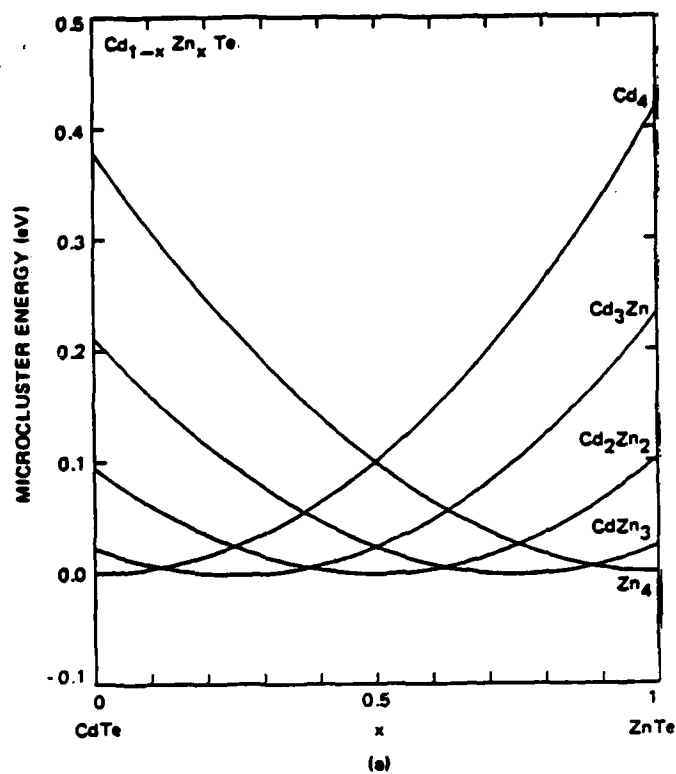
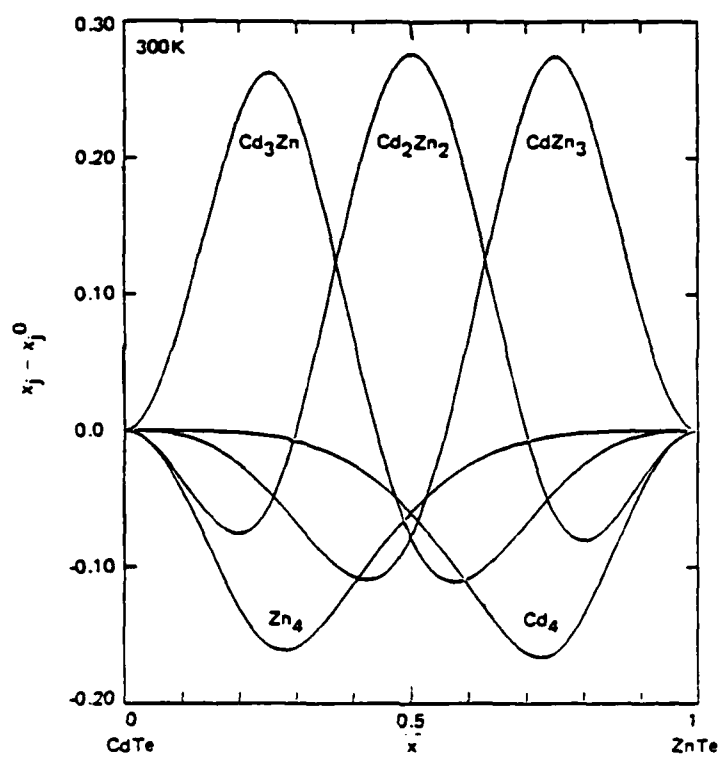
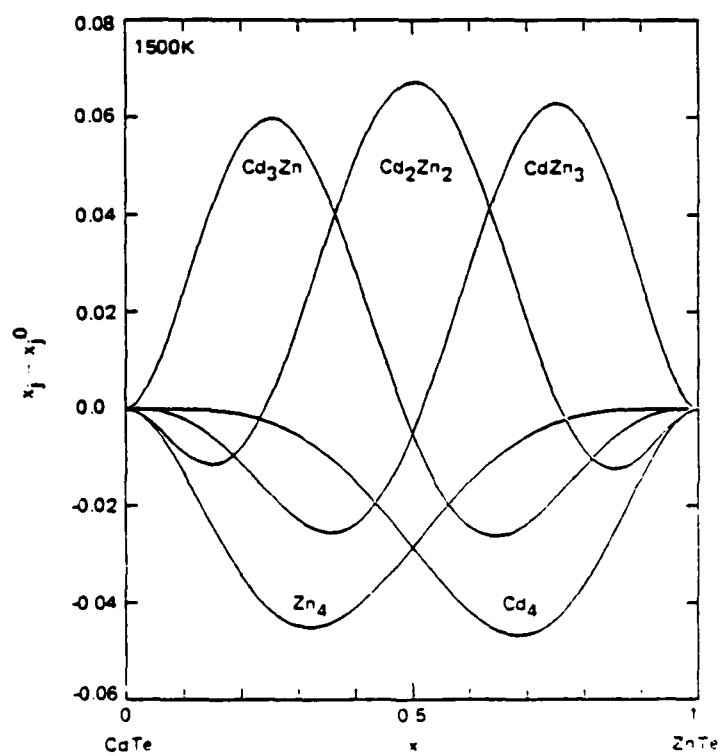


FIGURE 3



(a)



(b)

FIGURE 4

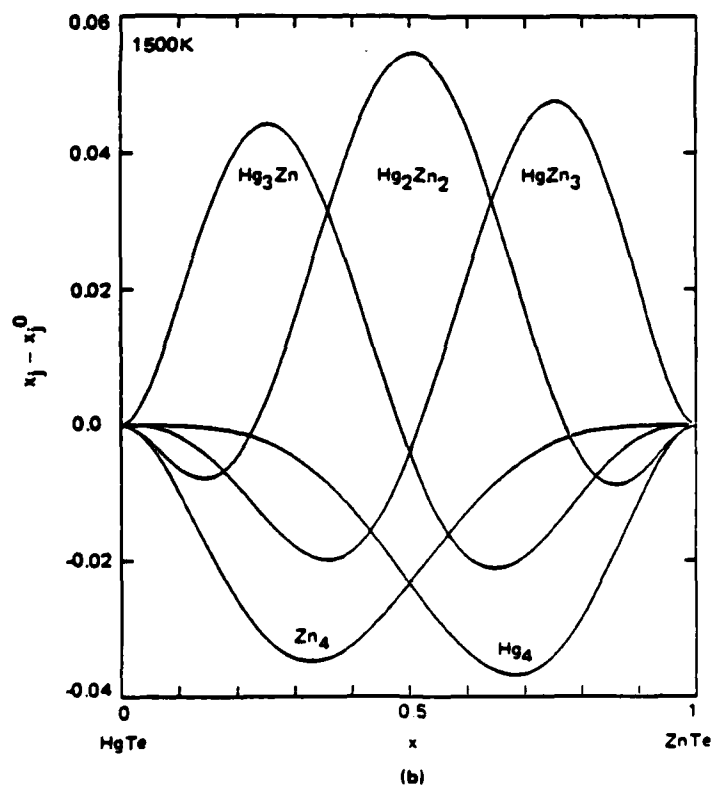
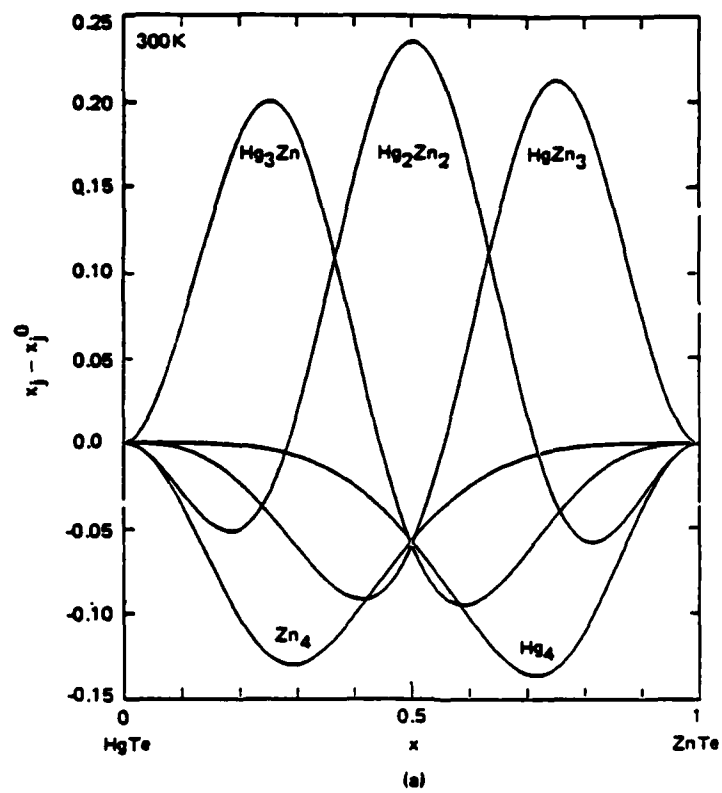


FIGURE 5

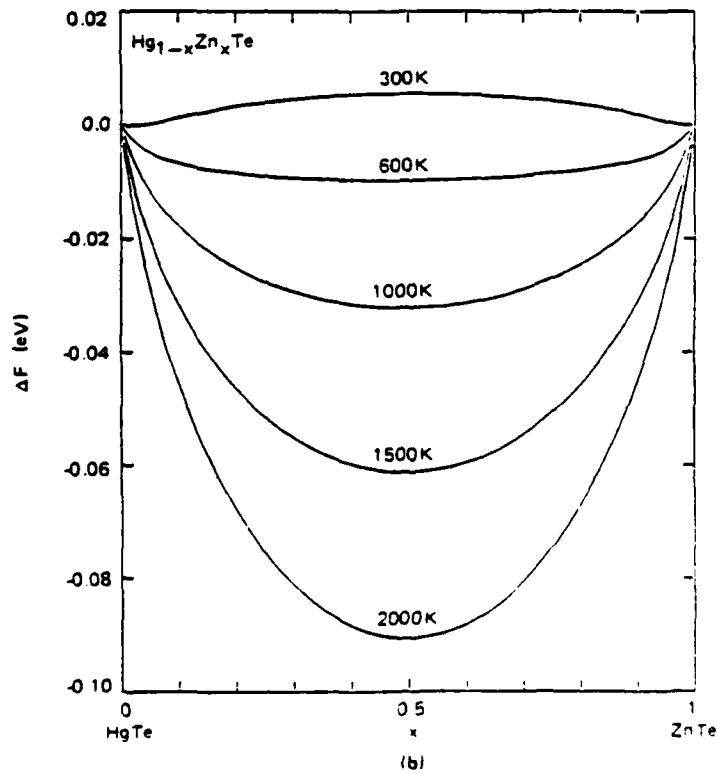
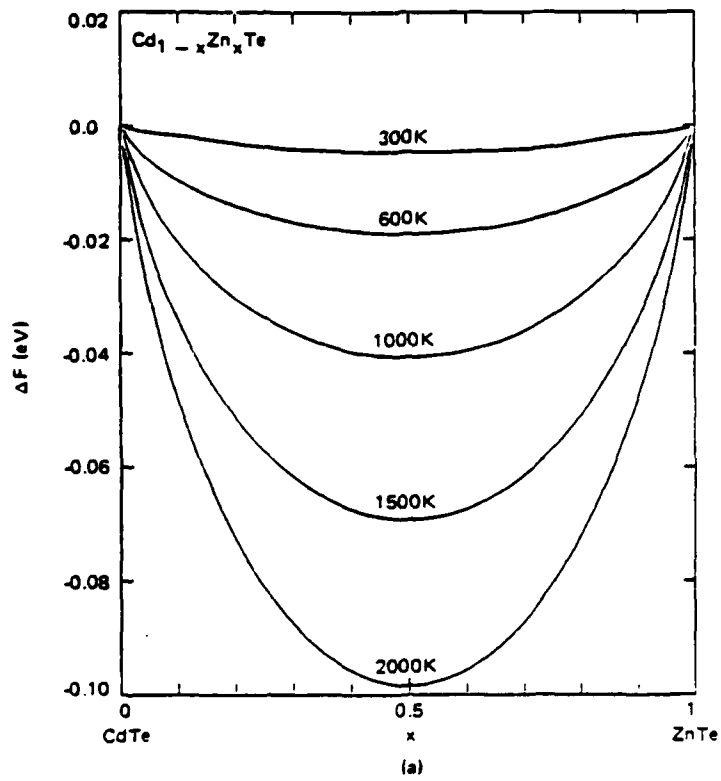


FIGURE 6

HUGHES

SANTA BARBARA RESEARCH CENTER
a subsidiary

(THIS PAGE INTENTIONALLY LEFT BLANK)



SANTA BARBARA RESEARCH CENTER
KSC 200 1-100

Section 5
LIST OF PAPERS, PRESENTATIONS AND THESES
SUPPORTED IN PART OR IN WHOLE
BY THIS CONTRACT

PUBLICATIONS SUPPORTED IN WHOLE OR IN PART BY THIS PROGRAM

1. J.A. Wilson, J.A. Silberman, P. Morgan, I. Lindau and W.E. Spicer, Paper A 4, Meeting of the IRIS Specialty Group on Infrared Detectors, 2-4 June 1981, Syracuse, New York.
2. J.A. Wilson, C.E. Jones, V.A. Cotton, M.D. Jack, A.G. Toth and J.K. Henriksen, Paper C-12, Meeting of the IRIS Specialty Group on Infrared Detectors, 27-29 July 1982, San Diego, California.
3. D.R. Rhiger, J.A. Wilson, J.M. Myrosznyk, R.E. Starr, S.L. Price, K.A. Kormos, M. Ray, J.W. Peters and H.H. Rogers, Paper D-8, Meeting of the IRID Specialty Group on Infrared Detectors, 27-29 July 1982, San Diego, California.
4. J.A. Wilson, V.A. Cotton, J.A. Silberman, D. Larer, W.E. Spicer and P. Morgen, "HgCdTe-SiO₂ Interface Structure," J. Vac. Sci. Technol., A 1 (3), 1719 (1983).
5. J.A. Wilson and V.A. Cotton, "Electrical Properties of the SiO₂:HgCdTe Interface," J. Vac. Sci. Technol., A 3 (1), 199 (1985).
6. J.A. Wilson and V.A. Cotton, "Effects of H₂O on the SiO₂-HgCdTe Interface," J. Appl. Phys., 57 (6), 2030 (1985).
7. J.A. Wilson and V.A. Cotton, "Storage Time at the SiO₂-HgCdTe Interface," Submitted to Journal of Applied Physics.
8. A. Ksendzov, F.H. Pollak, J.A. Wilson and V.A. Cotton, "Electroreflectance Study of HgCdTe in the Metal-Insulator-Semiconductor Configuration at 77K," Submitted to Applied Physics Letters.
9. J.A. Wilson and V.A. Cotton, "Damage Enhanced Doping at the HgCdTe Surface," In Preparation.
10. V.A. Cotton and J.A. Wilson, "Effects of Ion Implantation on Deep Electron Traps in Hg_{0.7}Cd_{0.3}Te," to be published in The Proceedings of the 1985 U.S. Workshop on the Physics and Chemistry of HgCdTe, J. Vac. Sci. and Technol.
11. V.A. Cotton and J.A. Wilson, "Carrier Trapping Centers in Randomly Implanted HgCdTe," proceedings of the IRIS Specialty Group on Infrared Materials, 18-19 June 1985, Colorado Springs, Colorado.
12. V.A. Cotton, J.A. Wilson and C.E. Jones, "Deep Electron Traps Near the Passivated Interface of HgCdTe," J. Appl. Phys., 58, 2208 (1985).
13. P. Morgen, J.A. Silberman, I. Lindau, W.E. Spicer, and J.A. Wilson, "Oxidation of Hg_{1-x}Cd_xTe Studied with Surface Sensitive Techniques," J. of Electronic Mat. Vol. II, No. 4, 597-610 (1982).

14. W.E. Spicer, J.A. Silberman, P. Morgen, I. Lindau, J.A. Wilson, An-Ban Chen, and A. Sher, "Dominance of Atomic States in a Solid: Selective Breakdown of the Virtual Crystal Approximation in a Semiconductor Alloy, $\text{Hg}_{1-x}\text{Cd}_x\text{Te}$," Phys. Rev. Lett., 49, No. 13, 948-951 (1982).
15. W.E. Spicer, J.A. Silberman, P. Morgen, I. Lindau, J.A. Wilson, A-B. Chen and A. Sher, "Unusual Behavior of $\text{Hg}_{1-x}\text{Cd}_x\text{Te}$ and Its Explanation," Physica 117B and 118B, 60-62 (1983).
16. W.E. Spicer, J.A. Silberman, I. Lindau, A-B. Chen, A. Sher, and J.A. Wilson, "Bandgap Variation and Lattice, Surface, and Interface 'instabilities' in $\text{Hg}_{1-x}\text{Cd}_x\text{Te}$," J. Vac. Sci. Technol., A 1 (3), Jul/Sept, 1674-1677 (1983).
17. A-B. Chen, A. Sher, and W.E. Spicer, "Relation Between the Electronic States and Structural Properties of $\text{Hg}_{1-x}\text{Cd}_x\text{Te}$," J. Vac. Sci. Technol., A 1 (3), Jul/Sept, 1674-1677 (1983).
18. J.A. Silberman, D. Laser, I. Lindau, W.E. Spicer and J.A. Wilson, "Initial Stages of Oxide Formation of HgCdTe Exposed to Activated Oxygen," J. Vac. Sci. Technol., A 3 (3), Jul/Sept, 1706-1711 (1983).
19. J.A. Silberman, D. Laser, I. Lindau, and W.E. Spicer, "Activated Oxygen Uptake on HgTe , CdTe , and $\text{Hg}_{0.69}\text{Cd}_{0.31}\text{Te}$," J. Vac. Sci. Technol., B 2, 589-590 (1985).
20. D. Laser, J.A. Silberman, W.E. Spicer, and J.A. Wilson, "Photoelectrochemical Effect of Anodic Oxide of $\text{Hg}_{1-x}\text{Cd}_x\text{Te}$," J. Appl. Phys., 56, 1897-1899 (1984).
21. C.K. Shih, W.E. Spicer, W.A. Harrison, A. Sher, "Bond-Length Relaxation in Pseudobinary Alloys," Phys. Rev., B 32, 1139 (1985).
22. G.P. Carey, S. Cole, T. Yamashita, J.A. Silberman, W.E. Spicer, and J.A. Wilson, "TEM Investigation of the Differences in Ion Milling Induced Damage of $\text{Hg}_{1-x}\text{Cd}_x\text{Te}$ and CdTe Heterojunctions," J. Vac. Sci. Technol., A 3 (1), 255-258 (1985).
23. J.A. Silberman, D. Laser, I. Lindau, W.E. Spicer, and J.A. Wilson, "Comparative Study of Activated Oxygen Uptake on HgTe , $\text{Hg}_{0.69}\text{Cd}_{0.31}\text{Te}$, and CdTe ," J. Vac. Sci. Technol., A 3 (1), 222-225 (1985).
24. J.A. Silberman, D. Laser, C.K. Shih, D.J. Friedman, I. Lindau, W.E. Spicer, and J.A. Wilson, "Angle-Resolved Photoemission Spectroscopy of $\text{Hg}_{1-x}\text{Cd}_x\text{Te}$," J. Vac. Sci. Technol., A 3, 233-237 (1985).
25. S. Cole, G.P. Carey, J.A. Silberman, W.E. Spicer, and J.A. Wilson, "Surface and Bulk Structural Defects in $\text{Hg}_{1-x}\text{Cd}_x\text{Te}$," J. Vac. Sci. Technol., A 3 (1), 1985.
26. D.J. Friedman, G.P. Carey, C.K. Shih, I. Lindau, W.E. Spicer, and J.A. Wilson, "Diffusion of Ag and Hg at the Ag/(Hg,Cd)Te Interface," Applied Physics Letters, to be published.

27. D.J. Friedman, G.P. Carey, C.K. Shih, I. Lindau, W.E. Spicer, and J.A. Wilson, "The Ag/(Hg,Cd)Te and Al/(Hg,Cd)Te Interfaces," Proceedings of the 1985 MCT Workshop, to be published.
28. C.K. Shih, D.J. Friedman, K.A. Bertness, I. Lindau, W.E. Spicer, and J.A. Wilson, "Electron Beam Induced Hg Desorption and the Electronic Structure of the Hg Depleted Surface of $\text{Hg}_{1-x}\text{Cd}_x\text{Te}$," Proceedings of the 1985 MCT Workshop, to be published.
29. D.J. Friedman, G.P. Carey, I. Lindau, W.E. Spicer, and J.A. Wilson, "Role of Hg Bonding in Metal/ $\text{Hg}_{1-x}\text{Cd}_x\text{Te}$ Interface Formation," Proceedings of the 1986 PCSI Conference, to be published.
30. W.A. Harrison, J. Vac. Sci. Technol., A 1, 1672 (1983).
31. A-B. Chen, A. Sher and W.E. Spicer, "Relation Between the Electronic States and Structural Properties of $\text{Hg}_{1-x}\text{Cd}_x\text{Te}$," J. Vac. Sci. Technol., Vol. 1, No. 3, 1674-1677 (1983).
32. T.N. Casselman, A. Sher, J.A. Silberman, W.E. Spicer, A-B. Chen, "On the Determination of the energy Band Offsets in $\text{Hg}_{1-x}\text{Cd}_x\text{Te}$ Heterojunction," J. Vac. Sci. Technol., Vol. 1, No. 3, 1692 (1983).
33. A-B. Chen, and A. Sher, "Bonding Theory of Semiconductor Alloys," in Microelectronics-Applications, Materials, and Technology, Vol. 3, (1984), SRI International Microelectronics Multiclient Program SRI International, Menlo Park, California.
34. A. Sher, A-B. Chen, and W.E. Spicer, "Phenomena Influencing the Dislocation Density of Semiconductor Compounds and Alloys," Proc. 13th International Conference on Defects in Semiconductors, AIME, Coronado, California, (12-17 August 1984).
35. A. Sher, A-B. Chen, and W.E. Spicer, "Dislocation Energies and Hardness of Semiconductors," Appl. Phys. Lett., Vol. 46, No. 1, 54 (January 1985).
36. A. Sher, A-B. Chen, W.E. Spicer and C.K. Shih, "Effects Influencing the Structural Integrity of Semiconductors and Their Alloys," J. Vac. Sci. Technol., Vol. A3, No. 1, 105 (January-February 1985).
37. C.K. Shih, W.E. Spicer, W.A. Harrison, and A. Sher, "Bond-Length Relaxation in Pseudobinary Alloys," Phys. Rev., Vol. 31, No. 2, 1139 (January 1985).
38. A-B. Chen and A. Sher, "Sensitivity of Defect Energy Levels to Host Band Structures and Impurity Potentials in CdTe," Phys. Rev. B., Vol. 31, No. 10, 6490-6497 (May 1985).
39. S. Krishnamurthy, A. Sher and A-B. Chen, "Generalized Brooks' Formula and the Electron Mobility in $\text{Si}_x\text{Ge}_{1-x}$ Alloys," Appl. Phys. Lett., Vol. 47, No. 2, 160-162 (July 1985).

40. S. Krishnamurthy, A. Sher and A-B. Chen, "Binding Energy and Spectral Width of Si 2p Core Excitons in $\text{Si}_x\text{Ge}_{1-x}$ Alloys," Phys. Rev. Lett., Vol. 55, No. 3, 320-323 (July 1985).
41. S. Krishnamurthy, A. Sher and A-B. Chen, "Band Structures of $\text{Si}_x\text{Ge}_{1-x}$ Alloys," Phys. Rev. B., (in press).
42. G.H. Tsau, A. Sher, M. Madou, J.A. Wilson, V.A. Cotton and C.E. Jones, "Low Frequency Admittance Measurements on the HgCdTe/PHOTOX™ SiO_2 Interface," J. Appl. Phys., (in press).
43. A. Sher, A-B. Chen, and M. van Schilfgaarde, "Correlations in Pseudobinary Alloys," J. Vac. Sci. Technol., A, (in press).

PRESENTATIONS SUPPORTED IN WHOLE OR IN PART BY THIS PROGRAM

1. J.A. Wilson, "Photoemission Investigation of an Atomically Clean $\text{Hg}_{1-x}\text{Cd}_x\text{Te}$ Surface in Vacuum and Under O_2 Exposure," Meeting of the IRIS Specialty Group on Infrared Detectors, June 2-4, 1981, Syracuse, New York.
2. J.A. Wilson, "Investigation of the Interface Region in n-Type HgCdTe ," Meeting of the IRIS Specialty Group on Infrared Detectors, July 27-29, 1982, San Diego, California.
3. D.R. Rhiger, "Photochemical Vapor Deposited Silicon Dioxide for HgCdTe Device Applications," Meeting of the IRIS Specialty Group on Infrared Detectors, July 27-29, 1982, San Diego, California.
4. J.A. Wilson, " HgCdTe-SiO_2 Interface Structure," 1983 U.S. Workshop on the Physics and Chemistry of Mercury Cadmium Telluride, February 8-10, 1983, Dallas, Texas.
5. J.A. Wilson, "Electrical Properties of the $\text{SiO}_2:\text{HgCdTe}$ Interface," 1984 U.S. Workshop on the Physics and Chemistry of Mercury Cadmium Telluride, May 14-17, 1984, San Diego, California.
6. V.A. Cotton, "Deep Electron Traps Near the Passivated Interface of HgCdTe ," 1984 U.S. Workshop on the Physics and Chemistry of Mercury Cadmium Telluride, May 14-17, 1984, San Diego, California.
7. V.A. Cotton, "Carrier Trapping Centers in Randomly Implanted HgCdTe ," Meeting of the IRIS Specialty Group on Infrared Detector Materials, June 18-19, 1985, Colorado Springs, Colorado.
8. V.A. Cotton, "Effect of Ion Implantation on Deep Electron Traps in $\text{Hg}_{0.7}\text{Cd}_{0.3}\text{Te}$," 1985 U.S. Workshop on the Physics and Chemistry of Mercury Cadmium Telluride, October 8-10, 1985, San Diego, California.
9. W.E. Spicer, "Surface and Interfaces of HgCdTe . What Can We Learn From 3-5's? What is Unique With HgCdTe ?" The First U.S. Workshop on the Physics and Chemistry of Mercury Cadmium Telluride, 1981, Minneapolis, Minnesota.
10. J.A. Silberman, "UPS Study of the Electronic Structure of $\text{Hg}_{1-x}\text{Cd}_x\text{Te}$: Breakdown of the Virtual Crystal Approximation," The First U.S. Workshop on the Physics and Chemistry of MCT, 1981.
11. J.A. Silberman, "Room-Temperature Stability of Cleaved $\text{Hg}_{1-x}\text{Cd}_x\text{Te}$," The First U.S. Workshop on the Physics and Chemistry of MCT, 1981.
12. W.E. Spicer, "Dominance of Atomic States in a Solid: Selective Breakdown of the Virtual Crystal Approximation in a Semiconductor Alloy, $\text{Hg}_{1-x}\text{Cd}_x\text{Te}$," 16th International Conference on the Physics of Semiconductors, 1982, Montpellier, France.

13. W.E. Spicer, "Interrelation Between $\text{Hg}_{1-x}\text{Cd}_x\text{Te}$ Interfaces Defects, Oxidation, Band Structure, and the Strength of the Hg-Te Bond," SPIE Conference, 1983, Arlington, Virginia.
14. J.A. Silberman, "Initial Stages of Oxide Formation on HgCdTe Exposed to Activated Oxygen," U.S. Workshop on the Physics and Chemistry of MCT, 1983, Dallas, Texas.
15. J.A. Silberman, "Oxygen Uptake on $\text{Hg}_{1-x}\text{Cd}_x\text{Te}$ and Related Compounds," Tenth Annual Conference on the Physics and Chemistry of Semiconductor Interface, 1983, Santa Fe, New Mexico.
16. J.A. Silberman, "Angle-Resolved Photoemission Spectroscopy of $\text{Hg}_{1-x}\text{Cd}_x\text{Te}$," U.S. Workshop on the Physics and Chemistry of MCT, 1984, San Diego, California.
17. J.A. Silberman, "Comparative Study of Activated Oxygen Uptake on HgTe , $\text{Hg}_{0.69}\text{Cd}_{0.31}\text{Te}$, and CdTe , U.S. Workshop on the Physics and Chemistry of MCT, 1984.
18. G.P. Carey, "Surface and Bulk Structural Defects in $\text{Hg}_{1-x}\text{Cd}_x\text{Te}$," U.S. Workshop on the Physics and Chemistry of MCT, 1984.
19. G.P. Carey, "TEM Investigation of the Differences in Ion Milling Induced Damage of $\text{Hg}_{1-x}\text{Cd}_x\text{Te}$ and CdTe Heterojunction," U.S. Workshop on the Physics and Chemistry of MCT, 1984.
20. J.A. Silberman, "Activated Oxygen uptake on HgTe , CdTe , and $\text{Hg}_{0.69}\text{Cd}_{0.31}\text{Te}$ (Poster)," 11th Annual Conference on the Physics and Chemistry of Semiconductor Interfaces, 1984, Pinehurst, North Carolina.
21. D.J. Friedman, "The $\text{Ag}/(\text{Hg},\text{Cd})\text{Te}$ and $\text{Al}/(\text{Hg},\text{Cd})\text{Te}$ Interfaces," U.S. Workshop on the Physics and Chemistry of MCT, 1985, San Diego, California.
22. D.J. Friedman, "Role of Hg Bonding in Metal/ $\text{Hg}_{1-x}\text{Cd}_x\text{Te}$ Interface Formation," Conference on the Physics and Chemistry of Semiconductor Interfaces, 1986, Pasadena, California.
23. A. Sher, "Phenomena Influencing the Dislocation Density of Semiconductor Compounds and Alloys," 13th Int. Conference of Defects in Semiconductors, August 12-17, 1984, Coronado, California.
24. G.H. Tsau, "Low Frequency Admittance Measurements on the $\text{HgCdTe}/\text{PHOTOX}^{\text{TM}}/\text{SiO}_2$ Interface," 1985 U.S. Workshop on the Physics and Chemistry of $\text{Hg}_{1-x}\text{Cd}_x\text{Te}$, San Diego, California.

THESES SUPPORTED IN WHOLE OR IN PART BY THIS PROGRAM

This contract has enabled support of the following students in part or all of their Ph.D. thesis research at Stanford University.

J.A. Silberman Electronic Structure and Oxidation of $\text{Hg}_{1-x}\text{Cd}_x\text{Te}$
G.P. Carey Surface and Bulk Defect Structural Studies of $\text{Hg}_{1-x}\text{Cd}_x\text{Te}$
D.J. Friedman Metal/(Hg,Cd)Te Interface Formation and Properties
C.K. Shih Electronic Structure and Bonding Properties of $\text{Hg}_{1-x}\text{Cd}_x\text{Te}$
C.M. Stahle Investigation of Anodic Oxides Grown on $\text{Hg}_{1-x}\text{Cd}_x\text{Te}$
A.K. Wahi Electronic Properties of $\text{Hg}_{1-x}\text{Cd}_x\text{Te}$ Surfaces

and one masters thesis at the University of California at Santa Barbara

V.A. Cotton Device Processing Effects on Deep Electron Traps in $\text{Hg}_{1-x}\text{Cd}_x\text{Te}$

END
FILMED

5-86

DTIC